XAFS study of the pressure induced B1→B2 phase transition

by

Shelly D. Kelly

A dissertation submitted in partial fulfillment of the requirements for the degree of

Doctor of Philosophy

University of Washington

1999

Approved by_____
(Chairperson of Supervisory Committee)

Program Authorized
to Offer Degree_____

Date_____

In presenting this dissertation in partial fulfillment of the requirements for the Doctoral degree at the University of Washington, I agree that the Library shall make its copies freely available for inspection. I further agree that extensive copying of this dissertation is allowable only for scholarly purposes, consistent with "fair use" as prescribed in the U. S. Copyright Law. Requests for copying or reproduction of this dissertation may be referred to University Microfilms, 1490 Eisenhower Place, P. O. Box 975, Ann Arbor, MI 49106, to whom the author has granted "the right to reproduce and sell (a) copies of the manuscript in microform and/or (b) printed copies of the manuscript made from microform."

Signature_____

Date_____

University of Washington

Abstract

XAFS study of the pressure induced B1→B2 phase transition

by Shelly D. Kelly

Chairperson of Supervisory Committee
Professor Robert Ingalls
Department of Physics

Pressure dependent x–ray absorption fine structure (XAFS) measurements on RbCl, AgCl and AgBr are presented in this thesis. Measurements on RbCl are presented at pressures spanning its structural B1→B2 phase transition including three measurements at the transition region between these phases. Using these XAFS data, I provide direct evidence of the martensitic-like phase transition mechanism. The local structure of RbCl at the transition is shown to be a mixture of the B1 and B2 phases. The amount of disorder in the structure at the transition is shown to be no greater than that found in the single phase region also an excess pressure required to initiate the phase transition was observed. AgCl and AgBr are said to undergo a B1→KOH→TlI→B2 phase transition. Measurements on AgCl and AgBr are present at pressures spanning the structural B1→KOH→TlI and B1→KOH transition, respectively. Using these XAFS data, I have determined the atomic positions for the KOH and TlI high pressure phases which was previously unknown. These local structures are found to be consistant with a topological transition mechanism where each phase is related to a KOH-type structure. The pressure dependence of the KOH and TlI-type phases indicates that these phases are stable within a large pressure region, and that the transition mechanism from the B1→B2 phase is not due to a gradual distortion of these two intermediate high pressure phases. Further evidence for a martensitic-like transition between the B1→KOH phases was found for AgBr, where for one measurement at the transition region the local structure was determined to be a mixture of the B1 and KOH-type phases. Although experiemental difficulties in

obtaining truely hydrostatic samples at these high pressure leads this evidence to be inconclusive in terms of its cause.

TABLE OF CONTENTS

List of Figures **iv**

List of Tables **viii**

Chapter 1: Introduction **1**

Chapter 2: X-ray Absorption Fine Structure: Method of Analysis **5**

2.1 X-ray Absorption Fine Structure (XAFS) 5

2.1.1 Basic Principles Involved in XAFS 6

2.1.2 Understanding the XAFS Equation 9

2.1.3 Extras in the XAFS Equation 12

2.2 Data Analysis 19

2.2.1 Isolation of the XAFS Signal 19

2.2.2 Fourier Transforms 25

2.2.3 Theoretical Models: FEFF 27

2.2.4 Fitting Theoretical Model to Data: FEFFIT 30

Chapter 3: XAFS Experiments **36**

3.1 Experimental Setup 36

3.1.1 Monochromator 37

3.1.2 Pinhole 40

3.1.3 Ion Chambers 41

3.1.4 High Pressure Experiment 43

3.2 Sample Preparation 47

3.2.1 Choice of Pressure Calibrant 48

3.2.2 Samples 49

3.3 XAFS Measurements 50

3.3.1 Signal to Noise 51

3.3.2 Errors in XAFS Measurements 53

Chapter 4: Niobium Pressure Calibrant **55**
4.1 Crystal Structure of Nb 57
4.1.1 Fourier Transform as a Finger-Print 57
4.1.2 Pressure Dependence of $|\tilde{\chi}(R)|$ 59
4.2 Alignment and Background Removal 59
4.3 XAFS Parameters and Meaningful Parameters 60
4.4 Determination of S_0^2 64
4.5 Determination of ΔE_0 66
4.6 Determination of Compression and Pressure 67

Chapter 5: The B1 to B2 Phase Transition of RbCl **72**
5.1 Crystal Structure of RbCl 72
5.1.1 Fourier Transform as a Finger Print 74
5.2 Alignment and Background Removal 74
5.3 Overview of Fit Procedure 76
5.4 Analysis of the Pure B1- and B2-Phases of RbCl 78
5.4.1 XAFS Parameters and Meaningful Parameters 78
5.4.2 Determination of S_0^2 80
5.4.3 Determination of ΔE_0 80
5.4.4 Determination of Pressure Dependent Parameters 81
5.5 Analysis of the Transition Region of RbCl 87
5.5.1 Modeled as a Mixture of B1- and B2-Phases 87
5.5.2 Modeled as a Distorted B1-phase 89
5.6 Conclusions 95

Chapter 6: Local Structure of AgCl Under Pressure **97**
6.1 Topological Relationship 98
6.2 A First Look at the Data 102
6.3 B1-Phase of AgCl 104
6.3.1 Alignment and Background Removal 105
6.3.2 XAFS Parameters and Meaningful Parameters 106
6.3.3 Determination of S_0^2 106
6.3.4 Pressure Dependences for the B1-Phase of AgCl 106

6.4 HPPI of AgCl 109
6.4.1 HPPI Model 111
6.4.2 Crystal Structure and Radial Distribution 112
6.4.3 HPPI Results and Pressure Dependence 115
6.5 HPPII of AgCl 117
6.5.1 HPPII Model 120
6.5.2 HPPII Results and Pressure Dependence 120
6.6 Discussion 123
6.7 Conclusions 131

Chapter 7: Local Structure of AgBr Under Pressure 133
7.1 A First Look at the Data 133
7.2 B1-Phase of AgBr 134
7.2.1 Alignment and Background Removal 134
7.2.2 XAFS Parameters and Meaningful Parameters 135
7.2.3 Determination of S_0^2 136
7.2.4 Pressure Dependences for the B1-Phase of AgBr 136
7.3 HPPI of AgBr 140
7.3.1 HPPI Model 140
7.3.2 HPPI Results and Pressure Dependence 140
7.4 Conclusions 145

Chapter 8: Conclusions 148

Bibliography 150

Appendix A: Fitting Models in feffit 156
A.1 Nb Calibrant 158
A.2 RbCl 158
A.2.1 B1-Phase and B2-Phase 158
A.2.2 Mixture of B1- and B2-Phases 160
A.3 AgCl and AgBr 160
A.3.1 KOH-Type Phase 161
A.3.2 TlI-Type Phase 161

LIST OF FIGURES

1.1 Cartoon of martensitic-like transition 2
1.2 Topological phase transition 3

2.1 The absorption coefficient for copper. 6
2.2 The interference of the photoelectron wave with its self. 8
2.3 An example of μ_0(E)·x for copper. 21
2.4 Comparison of pre-edge background. 23
2.5 Example of Copper K-edge μ(E)·x data before and after normalization. 24
2.6 An example of a Hanning window. 26
2.7 Copper data and theoretical model 28

3.1 A schematic of a high pressure XAFS transmission experiment 36
3.2 A schematic for Bragg reflection 37
3.3 The reduction of harmonics by detuning 39
3.4 A schematic of the pinhole and tool 41
3.5 XAFS data of copper in a diamond anvil cell 43
3.6 A schematic of the XAFS high pressure cell 44
3.7 The x-ray absorption coefficient for the B_4C anvils 46
3.8 A diagram of the low temperature apparatus 48
3.9 A schematic for the intensities attenuated in an XAFS experiment . . 52

4.1 The pressure dependence of the fraction change in the first nearest neighbor distance for Nb 56
4.2 Pressure dependence of $|\tilde{\chi}(R)|$ for Nb 58
4.3 Data and background function for Nb 60
4.4 Averaged $\chi(k)\cdot k^3$ data for Nb 61
4.5 An example of different k-weightings of $|\tilde{\chi}(R)|$ 65
4.6 K-weightings dependence of amplitude terms 66
4.7 $|\tilde{\chi}(R)|$ and Im$\tilde{\chi}(R)$ data and theoretical fit for Nb 68

4.8 Sample pressure as a function of helium gas pressure 70
4.9 Grüneisen relationship for Nb. 71

5.1 Phase diagram for RbCl 72
5.2 A cartoon of the B1 and B2 phases of RbCl 73
5.3 Pressure dependence of $|\tilde{\chi}(R)|$ for RbCl 75
5.4 Data and background function for RbCl 76
5.5 Comparison of $\chi(k)\cdot k^2$ data for RbCl 77
5.6 The pressure dependence of the fraction change in the first nearest neighbor distance for RbCl 79
5.7 Energy shifts for the pure phases of RbCl 82
5.8 Pressure dependence of $\theta_{\mathrm{Debye}_i}$ and C_3 for the pure phases of RbCl . . 83
5.9 Sample pressure for the pure phases of RbCl 84
5.10 $|\tilde{\chi}(R)|$ and $\mathrm{Im}\tilde{\chi}(R)$ data and model for the pure phases of RbCl . . . 85
5.11 The Grüneisen relationship for the B1- and B2-phases of RbCl 86
5.12 $|\tilde{\chi}(R)|$ and $\mathrm{Im}\tilde{\chi}(R)$ data and mixture model for RbCl at the transition 90
5.13 Fraction of B1-phase as a function of pressure 92
5.14 $|\tilde{\chi}(R)|$ and $\mathrm{Im}\tilde{\chi}(R)$ data and restricted KOH-type model for RbCl . . 93
5.15 $|\tilde{\chi}(R)|$ and $\mathrm{Im}\tilde{\chi}(R)$ data and KOH-type model for RbCl 96

6.1 A phase diagram for AgCl 97
6.2 A diagram of the relationship between the NaCl-type structure and the KOH-type structure 99
6.3 A starting model for HPPI of AgCl 100
6.4 A starting model for HPPII of AgCl 101
6.5 B1-phase of AgCl and a list of paths. 103
6.6 Comparison of $|\tilde{\chi}(R)|$ data for AgCl 104
6.7 Example of background function for AgCl 105
6.8 Data and results of theoretical fit for the B1-phase of AgCl 107
6.9 The Grüneisen relationship for the B1-phase of AgCl 109
6.10 Data and theoretical model for the starting model for the HPPI phase of AgCl 111
6.11 Radial distribution of atoms for the final model HPPI of AgCl 113
6.12 The final model for HPPI of AgCl 114

6.13 Data and theoretical model for HPPI of AgCl 116
6.14 Best-fit values for HPPI of AgCl 118
6.15 Data and theoretical model based on the starting model for HPPII of AgCl 120
6.16 Radial distribution of atoms for the final model of HPPII of AgCl . . 121
6.17 A diagram of the final model for HPPII of AgCl 122
6.18 Data and the best-fit theoretical model for HPPII of AgCl 123
6.19 Best-fit values for HPPII of AgCl 124
6.20 A diagram of the best-fit model of HPPII of AgCl in terms of the KOH and TlI space groups 126
6.21 KOH-type parameters for all phases of AgCl 127
6.22 A diagram of the KOH-type unit cell for each phase of AgCl 128
6.23 Volume per chemical formula as a function of pressure for AgCl . . . 128
6.24 A comparison of the starting and final models for HPPI of AgCl . . . 129
6.25 A comparison of the starting and final models for HPPII of AgCl . . 130

7.1 Pressure dependence of $|\tilde{\chi}(R)|$ for AgBr 133
7.2 Example of background function for AgBr data. 135
7.3 Comparison of the data and the best-fit theoretical model for the B1-phase of AgBr 136
7.4 The Grüneisen relationship for the B1-phase of AgBr 139
7.5 Radial distribution of atoms for HPPI of AgBr based on the best-fit to the XAFS data 142
7.6 A diagram of HPPI for AgBr 143
7.7 A comparison of the data and the theoretical model based on the best-fit to the XAFS data for HPPI of AgBr 144
7.8 A comparison of the data and the theoretical model based on the best-fit to the XAFS data for mixture of HPPI and B1 phases of AgBr . . 145
7.9 KOH-type parameters for all phases of AgBr 146
7.10 Volume per chemical formula as a function of pressure of AgBr 146

A.1 Part of a `feffit.inp` file specifying the path paragraph 157
A.2 Part of a `feffit.inp` for Nb 159
A.3 Part of a `feffit.inp` for B1-phase of RbCl 162

A.4 Part of a `feffit.inp` for mixture phase of RbCl 164
A.5 Part of a `feffit.inp` for mixture phase of RbCl 165
A.6 Part of a `feffit.inp` for mixture phase of RbCl 166
A.7 Part of a `feffit.inp` for mixture phase of RbCl 167
A.8 Part of the `feffit.inp` file for KOH-type phase of AgCl 170
A.9 Part of a `feffit.inp` for HPPII of AgCl 171
A.10 Part of a `feffit.inp` for HPPII of AgCl 172
A.11 Part of a `feffit.inp` for HPPII of AgCl 173

LIST OF TABLES

1.1 List of transition pressure for several alkali-halides 1

3.1 The energy ranges for several silicon monochromator crystals 38
3.2 The appropriate gasket and anvils for the experiment 47
3.3 The absorption sample coefficients for the AgBr experiment 50

4.1 Fourier transform parameters along with fit and data ranges for Nb . 58
4.2 Parameters used to calculate the compression of Nb. 64
4.3 Fit results for Nb 68
4.4 List of σ_i^2 and the corresponding θ_{Debye} for Nb 69
4.5 Extrinsic helium pressure to intrinsic sample pressure. 70

5.1 List of paths for the pure phases of RbCl 74
5.2 Fourier transform parameters along with fit and data ranges for RbCl 77
5.3 List of σ_i^2 and the corresponding θ_{Debye} for the B1-phase of RbCl . . . 85
5.4 List of σ_i^2 and the corresponding θ_{Debye} for the B2-phase of RbCl . . . 86
5.5 Best-fit values for the transition data of RbCl 88
5.6 Best-fit values for data corresponding to the structure before and after the transition for RbCl modeled as a mixture of B1 and B2 phases . . 89
5.7 Comparison of the goodness-of-fit parameters for the transition data of RbCl 93
5.8 Comparison of the intermediate and mixture of phases models for transition region of RbCl 94

6.1 Fourier transform parameters along with the fit and data ranges for AgCl105
6.2 The best-fit values for the B1-phase of AgCl 108
6.3 List of σ_i^2 and θ_{Debye} for the B1-phase of AgCl 110
6.4 List of σ_i^2 and θ_{Debye} for the KOH-type phase of AgCl 117
6.5 Atomic positions for HPPII of AgCl 121

6.6 List of σ_i^2 and θ_{Debye} for the TlI-type phase of AgCl 124
6.7 List of equivalent KOH atomic positions for HPPII of AgCl 125

7.1 A list of the first three shell distances and their degeneracy for the B1-phase of AgBr 134
7.2 Fourier transform parameters along with the fit and data ranges for AgBr 134
7.3 The best-fit values for the B1-phase of AgBr 137
7.4 List of σ_i^2 and θ_{Debye} for the B1-phase of AgBr 139
7.5 The best-fit values for the HPPI of AgBr 141
7.6 List of σ_i^2 and θ_{Debye} for the KOH-type phase of AgBr 142

A.1 Key words used in FEFFIT 156
A.2 Change of parameters for Nb calibrant 158
A.3 Change of parameters for the B1-phase of RbCl 160
A.4 Change of parameters for mixture of phases for RbCl 161
A.5 Change of parameters for the KOH-type phase of AgCl 168
A.6 Change of parameters for the TlI-type phase of AgCl 169

ACKNOWLEDGMENTS

"Thank you!" to my mentors, Bob Ingalls and Ed Stern. Bob is a caring and understanding teacher that has been incredibly patient. Ed is an expert problem solver, who has given me direction. The best part of my graduate study has been my relationship with Michael Kelly who is now my husband and has given me my memorable name. He has supported me emotionally and acted as a sounding board and an editor. He is simply the most amazing man I have ever known. I am also grateful to my colleagues. They have freely given their time and guidance. In particular I thank Bruce Ravel, Dani Haskel, Matt Newville, John Rehr and Fuming Wang.

To my mother Vicki, my father Stephen, my brothers: Wesley, Brandon and Travis, my sister–in–law Melinda, my nephew Taylor, and my new step–mother Connie and step–sister Megan: I love you all.

Chapter 1

INTRODUCTION

The goal of this thesis is to contribute to the study of the mechanism for the B1→B2 pressure-induced phase transitions. The B1-phase has the NaCl-type structure which is the crystal structure of many alkali-halides at ambient pressure and room temperature. The B2-phase has the CsCl-type structure which is the crystal structure of many of the same alkali-halides at higher pressures and temperatures. Table 1.1 lists several of these alkali-halides and their transition pressures at room temperature. Therefore the B1→B2 pressure-induced phase transition applies to a wide variety of materials. Several neutron and x-ray-diffraction studies have investigated the mechanism of the pressure-induced B1→B2 phase transition[1–5], from which two distinct displacive mechanisms have been proposed. In the first, the crystal structure at the transition consists of a mixture of B1 and B2 phases[2]. In the second, the crystal structure at the transition consists of an intermediate structure which is a distortion of the B1-phase[1].

Substance	Pressure (GPa)
NaCl [6]	18
KF [7]	1.7
KCl [6]	2.1
KBr [8]	1.8
KI [8]	1.8
RbF [7]	3.1
RbCl [6]	0.6
RbBr [8]	0.5
RbI [8]	0.4

Table 1.1: List of transition pressure for several alkali-halides

To explain the mixture of B1 and B2 phases at the transition Onodera *et at.*[2] proposed a displacive mechanism, with many martensitic-like properties, for the transition in RbCl. In martensitic transitions, excess pressure is required to nucleate the B2-phase. This property of martensitic transitions was confirmed in a single-crystal neutron-diffraction study in which an excess pressure of 0.16 GPa was needed to start the transition. Another property of the phase transition[2] is diffraction peaks that occurred at a constant angle across the transition. This is expected in martensitic transitions, where the nucleation of the parent phase is followed by a wave of shearing and deforming planes that transforms the B1-structure to the B2-structure. The wave is stopped by grain boundaries or imperfections in the crystal structure. At this point there is a mixture of both structures, which is stable until the pressure is raised and more of the B2-structure nucleates. This transition is depicted in Fig. 1.1. A stable coexistence of both phases was reported at 0.49 GPa[2]. References [2–5] showed that the diffraction lines at the transition became very broad, indicating a breakdown of the original B1-crystal into many grains. Again this is expected in a martensitic-like transition and makes the interpretation of diffraction peaks difficult.

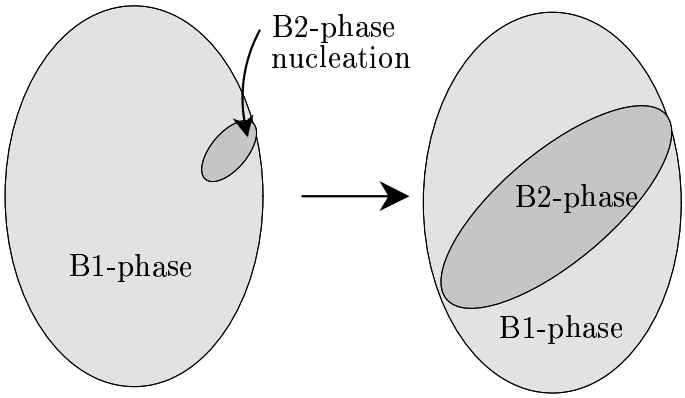

Figure 1.1: A cartoon of a martensitic-like transition. Excess pressure is required to nucleate the B2-phase which is followed by a shearing and deformation of planes transforming the B1-phase to the B2-phase. The wave is stopped by grain boundaries and imperfections in the crystal lattice. The crystal is now stable with some of both phases present. More pressure must be applied to nucleate more of the B2-phase.

Kusaba *et at.* [1] has proposed a different displacive mechanism for the B1→B2 phase transition based on energy-dispersive x-ray-diffraction spectroscopy of AgCl.

This mechanism involves the distortion of the original B1-phase to form two intermediate phases, the KOH-type structure and the TlI-type structure. They suggest that this transition mechanism is a continuous deformation of the B1-phase crystal planes. A diagram of this transition mechanism is shown in Fig 1.2. The crystal structure of the two intermediate phases has not been completely determined since the atomic positions within the unit cell are unknown. In the proceeding figure, the atoms have been placed in the positions found for actual TlI and KOH which has not been confirmed. This is because it is difficult to determine the absolute intensity of the energy-dispersive diffraction peaks due to the variation of the intensity with wavelength of the x-ray source. This creates a unique opportunity for x-ray absorption fine structure (XAFS) spectroscopy which can determine the local structure given the space group and unit cell dimensions from the x-ray diffraction study[1]. Although his work is based on AgCl, the author generalized his work to all B1→B2 type transitions. Therefore this model is also considered for our analysis of RbCl as well as AgCl and AgBr.

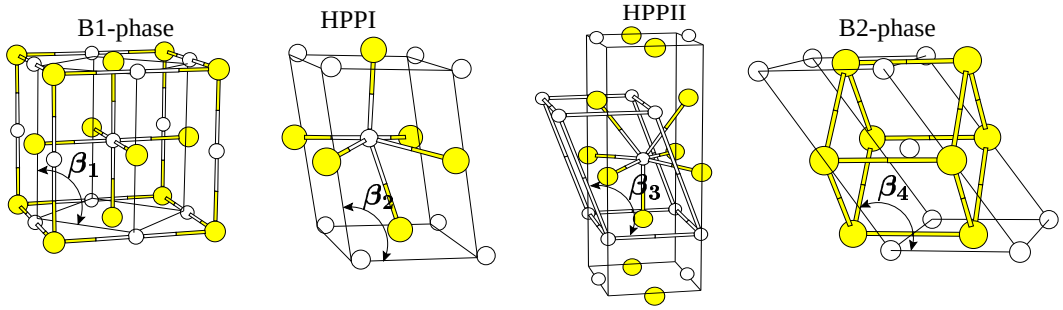

Figure 1.2: Cartoon of the proposed topological phase transition where there is a "topological" relationship between each of the phases in terms of the KOH-type unit cell. Left: The KOH-type unit cell for the B1-structure is shown as the outlined rectangle where $\beta_1 = 90°$. Middle Left: High pressure phase I, KOH-type unit cell where $\beta_2 = 101°$. Middle Right: High pressure phase II, KOH-type unit cell for TlI-type structure is shown by the tilted rectangle where $\beta_3 = 109°$. Right: The KOH-type unit cell for the B2-structure is shown as the outlined rectangle where $\beta_4 = 125.27°$. The continuous deformation of the planes resulting in larger β angles is an important feature of the transition mechanism.

XAFS probes the radial distribution of atoms surrounding a specific species.[9] In this thesis three systems are studied. They are the local structure about Rb and Ag atoms in RbCl, and AgCl and AgBr, respectively. XAFS measures only short-

range order, therefore, the structure surrounding the particular atoms at the phase transition can be determined where diffraction lines are broad due to broken grains in the crystal structure.

For RbCl I fit the data with the known crystal structure well below and above the transition and characterize the pressure dependence of the XAFS parameters so that I can construct a model for the transition based on a simple mixture of the two phases. This model is used to test for the martensitic-like transition proposed by Onodera *et at.* [2] as discussed above. As stated, I also explore the possibility of an intermediate structure at the transition by constructing a model for a distorted B1-structure based on the KOH-type structure proposed by Kusaba *et at.* [1] for the B1→B2 phase transition.

For AgCl and AgBr I fit the data with the known crystal structure well below the transition. As I discuss in more detail in Chapter 6, the B2-phase is only found a high temperatures therefore I do not have this other end point as my data was taken only at 150K. Again like the RbCl analysis I model data corresponding to the transition region as a mixture of B1 and B2 phases and as the distorted B1-structure based on the KOH-type and TlI-type structures.

Based on my analysis of the crystal structure at the transition region of the RbCl, AgCl and AgBr systems I plan to confirm a particular transition mechanism for each system. If the martensitic-like transition is found, I will be able to (1) confirm the excess pressure required to start the transition, (2) determine the pressure range in which the transition exists and, (3) characterize the distortion of the B1 and B2 phases during the transition. If the distorted B1-structure is found to have a KOH-type and TlI-type structures, I will be able to (1) determine the position of the atom within the unit cell, and (2) characterize the pressure dependence of the deformation process. Since there is some indication that RbCl will have the martensitic-like transition and AgCl and AgBr will have the distorted B1-structure transition. The most interesting possibility will be if both transitions can be related, since both have the B1-structure at ambient pressure and the B2-structure at high pressure (and high temperature for AgCl). It seems reasonable to assume that the transition mechanism would be similar or at least related in some way. This is the type of argument presented in Ref. [1] leading to the claim that the AgCl transition mechanism can be used to understand all B1→B2 phase transitions.

Chapter 2

X-RAY ABSORPTION FINE STRUCTURE: METHOD OF ANALYSIS

2.1 X-ray Absorption Fine Structure (XAFS)

There are three fundamental interactions of photons with matter[10]. These are the photoelectric effect, Compton scattering and pair production. The characteristic energy for XAFS, due to the photoelectric process, ranges from $\sim$ 3 to 40 keV which is in the x-ray region[11]. In this energy regime pair production is very energetically forbidden since it requires a photon energy of at least two times 511 keV to create both the electron and positron. The probability for electron scattering is also very small since the x-ray wavelength is much larger than the effective electron cross section. Scattering that does occur only adds a background whose energy dependence is smooth and easily subtracted. XAFS and the photoelectric process involves the total absorption of an x-ray by an atom. There is a dramatic increase in the probability for the absorption of an x-ray whose energy is equal to the binding energy of an electron compared to the absorption probability for an x-ray with slightly less energy. This increase in the absorption probability is referred to as an absorption edge. Every atomic electron has an associated absorption edge. To distinguish between the edges due to the excitation of an electron from the most tightly bound n=1 shell and the next most tightly bound n=2 shell, they are called the K-edge and L-edge, respectively. Therefore every atom with at least three electrons has a K- and L-edge. These are the most commonly studied XAFS edges. The K-edge for copper is shown in Fig. 2.1a. XAFS is the oscillatory part of the absorption coefficient shown within the box in Fig. 2.1a and alone in Fig. 2.1b.

X-rays that are absorbed with energy greater than the binding energy of the electron may result in a photoelectron with some kinetic energy. If the kinetic energy of the electron is large compared to its interaction energy with the neighboring atoms, the photoelectron is freed from the absorbing atom to the conduction band. Since this interaction energy is about 3 eV, the x-ray energy needs to be at least 15 eV

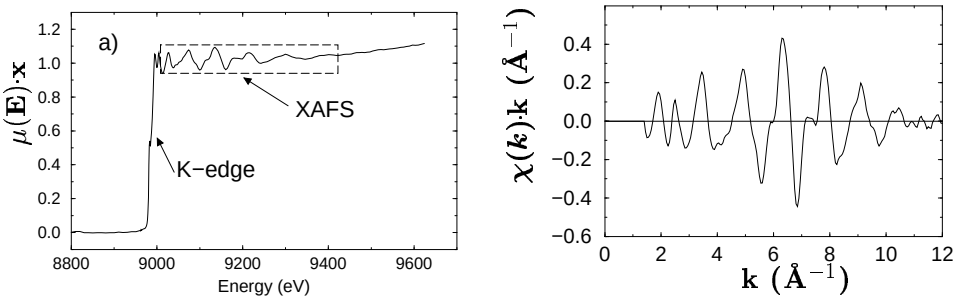

Figure 2.1: Left panel: The absorption coefficient for copper. The K-edge of copper is at 8987 eV and corresponds to the excitation of a n=1 shell electron. X-ray absorption fine structure, XAFS, is shown above the absorption edge in the dashed box. Right panel: Isolated XAFS signal from the boxed area in the left panel. Here the energy scale has been changed to the wavenumber of the photoelectron. The edge energy, 8987 eV, corresponds to a wave number of zero.

above the edge energy to completely free the electron. The distinction between a photoelectron with energy greater than or less than 15 eV is important in determining the main source of XAFS. For this reason XAFS has been historically split into two regions. The first contains the fine structure from the absorption edge to about 50 eV above the edge energy and is referred to as x-ray absorption near edge structure (XANES). The second region contains the fine structure from 50 eV to about 1000 eV above the edge energy and is referred to as extended x-ray absorption fine structure (EXAFS). Recently the theoretical calculations used to predict EXAFS have improved and much of the XANES has been incorporated into EXAFS making the distinction unnecessary[12]. Here I use the latter convention, referring to the x-ray absorption fine structure from approximately 20 eV to several hundred eV above the edge energy as XAFS.

2.1.1 Basic Principles Involved in XAFS

XAFS and its relationship to the local structure of a material can be understood intuitively. The ideas of this heuristic approach have been described previously in Refs. [13] and [14]. Since theses ideas are fundamental to the understanding of XAFS, they are presented again here. Detailed derivations of XAFS can be found in Refs. [15] and [16].

XAFS is due to the photoelectric effect which is described quantum mechanically

as the probability for the absorption of an x-ray by an atom. This probability, as contained in Fermi's Golden Rule, is proportional to the square of the matrix element between the initial and final states. The initial state consists of the electron in an atomic core. The final state consists of a core hole and a photoelectron in the conduction band, free from the absorbing atom. Since the initial state is well localized at the absorbing atom it is only necessary to determine the final state of the photoelectron at the absorbing atom.

Next, consider the free photoelectron as a wave propagating away from the absorbing atom with a wavelength given by the DeBroglie relation

$$\lambda = \frac{\mathrm{h}}{\mathrm{p}} \tag{2.1}$$

where h is Plank's constant and p is the momentum of the photoelectron. This momentum is simply related to the photoelectron's kinetic energy and is equal to the difference between the x-ray energy and the electron binding energy and is written as

$$\frac{\mathrm{p}^2}{2\mathrm{m}} = \mathrm{h}\nu - \mathrm{E}_0. \tag{2.2}$$

Here m is the mass of the photoelectron, E_0 is the binding energy of the electron and $\mathrm{h}\nu$ is the x-ray energy.

The interaction between the free photoelectron and the neighboring atoms can be treated as a perturbation. As shown in Fig. 2.2 the photoelectron propagates away form the absorbing atom and scatters off of the neighboring atoms. The interference between the outgoing and scattered part of the photoelectron at the absorbing atom modifies the photoelectron. This interference changes the probability for the absorption of an x-ray and is responsible for XAFS. The path of the photoelectron, to the neighboring atoms and then back to the absorbing atom, as well as the wavelength of the photoelectron determines the phase of the interference. The amplitude is determined, in part, by the type of neighboring atoms since they determine how strongly the photoelectron will be scattered.

In an XAFS experiment the energy of the incident x-ray is increased from approximately 200 eV below to 1000 eV above the absorption edge energy. This changes the wavelength of the photoelectron and results in the oscillations in the measured absorption coefficient. A maximum (minimum) occurs when the wavelength of the photoelectron, determined by the x-ray energy, and the path of the photoelectron

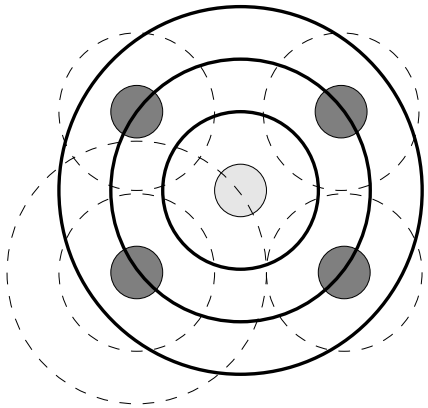

Figure 2.2: The central circle represents the x-ray absorbing atom. The photoelectron propagates away from the absorbing atom with a wavelength given by the DeBroglie relation. Crests of this wave are represented by the solid lines. The photoelectron may scatter from the neighboring atom(s). The crests of the scattered wave are represented by the dashed lines. A maximum (minimum) in the absorption probability for the x-ray occurs when the wavelength of the photoelectron, determined by the x-ray energy, and the path of the photoelectron which is the distance to and from the neighboring atoms, corresponds to constructive (destructive) interference between the photoelectron waves at the absorbing atom.

which is the distance to and from the neighboring atoms, corresponds to constructive (destructive) interference between the outgoing and scattered photoelectron waves at the absorbing atom. An example of theses oscillations in the absorption coefficient for the copper K-edge is shown in Fig. 2.1b.

Several other factors have helped XAFS become a powerful probe of local atomic structure. The sum rule for the interference of waves implies that the total contribution from all single scattering events of the photoelectron is equivalent to the sum of the individual contributions. A Fourier transform of the XAFS signal separates the contrition form each group of scattering atoms according to their radial distance. This allows information to be separated if a particular shell is isolated from its neighbors by at least an Å. Another fortunate consequence of the photoelectron and core hole is that their lifetimes are very short compared to atomic vibrations so that XAFS is an instantaneous "snap shot" of the local structure[13]. This allows thermal as well as static disorder in many materials to be distinguished.

2.1.2 Understanding the XAFS Equation

The XAFS equation is the basis for the theoretical models and the resulting fit parameters used to extract structural information. A physical interpretation of each term in the XAFS equation is essential to understanding the parameters and constraints used to fit the theoretical models to the data. First, I present the XAFS equation for a photoelectron which has scattered from a single atom. This equation is then generalized to account for all single scattering events of the photoelectron and to include multiple scattering events and non-symmetric disorder.

The XAFS signal, $\chi_i(\mathrm{k})$, for a photoelectron which scatters from a single atom at r_i is written as

$$\chi_i(\mathrm{k}) = \frac{\mathrm{S}_0^2 \mathrm{F}_i(k)}{\mathrm{kr}_i{}^2} e^{\frac{-2\mathrm{r}_i}{\lambda(\mathrm{k})}} \sin(2\mathrm{kr}_i + \delta_i(\mathrm{k})). \tag{2.3}$$

This relation maybe logically separated into three pieces: (1) the photoelectron wave, $\frac{\mathrm{F}_i(\mathrm{k})}{\mathrm{r}_i{}^2}\sin(2\mathrm{kr}_i + \delta_i(\mathrm{k}))$; (2) the lifetime of the photoelectron and core hole, $\mathrm{e}^{\frac{-2\mathrm{r}_i}{\lambda(\mathrm{k})}}$; (3) the passive electron reduction factor, S_0^2. Each part is described in the following subsections.

The Photoelectron Wave

As discussed in Sec. 2.1.1, XAFS is due to the interference between the original photoelectron and the scattered part of the photoelectron wave at the absorbing atom. A cartoon of this process is shown in Fig. 2.2. The outgoing photoelectron wave has the form $\mathrm{e}^{i\mathrm{kr}}/\mathrm{r}$, where k is the wavenumber of the photoelectron. The scattered wave has the same form except that the origin of the wave is shifted to the scattering atom at r_i

$$\frac{\mathrm{e}^{\mathrm{ik}|\mathrm{r}-\mathrm{r}_i|}}{|\mathrm{r}-\mathrm{r}_i|}. \tag{2.4}$$

The amplitude of this wave is proportional to the amplitude of the original wave at r_i and to the scattering amplitude $\mathrm{F}_i(\mathrm{k})$. The scattered wave at the absorbing atom ($\mathrm{r}_0 = 0$) becomes

$$\mathrm{F}_i(\mathrm{k})\frac{\mathrm{e}^{2\mathrm{ikr}_i}}{(\mathrm{r}_i)^2}. \tag{2.5}$$

Here the phase shift $2\mathrm{kr}_i$ is due to the photoelectron with wave number k that travels the distance $2\mathrm{r}_i$ to and from the scattering atom. This is called the path of the photoelectron with a path length of $2\mathrm{r}_i$. If the photoelectron traveled in a constant potential this would be the only phase shift factor. In fact, the photoelectron travels in a varying potentials of the absorbing and neighboring atoms. These varying potentials modify the phase by an additional term $[\delta(\mathrm{k}) - (\pi/2)]$. Accounting for these extra phase factors, the expression for the scattered wave becomes

$$\mathrm{F}_i(\mathrm{k})\frac{\mathrm{e}^{\mathrm{i}[2\mathrm{kr}_i+\delta_i(\mathrm{k})-(\pi/2)]}}{(\mathrm{r}_i)^2}. \tag{2.6}$$

The real part of Eq. 2.6 comprises the main components of the XAFS equation (see Eq. 2.3) for a single scattering path of the photoelectron and is written as:

$$\frac{\mathrm{F}_i(\mathrm{k})}{{\mathrm{r}_i}^2}\sin(2\mathrm{kr}_i + \delta_i(\mathrm{k})). \tag{2.7}$$

Lifetime of the Photoelectron and Core Hole

Another important term in the XAFS equation is due to the finite lifetime of the photoelectron and the core hole. Because XAFS is a direct measure of the interference between the original photoelectron and the scattered part of the photoelectron wave, the degradation of the wave due to inelastic scattering destroys its coherence and therefore the XAFS signal. This is interpreted as the finite lifetime of the photoelectron. The lifetime of the core hole depends on the atomic species and the photoelectron shell. In general the core hole exists for about 10^{-15} seconds before it is re-populated. (Tabulated values can be found in Ref. [17].) The net effect of the finite core hole lifetime and the finite lifetime of the photoelectron is an exponential decay of the XAFS signal written as

$$\mathrm{e}^{\frac{-2\mathrm{r}_i}{\lambda(\mathrm{k})}} \tag{2.8}$$

where $\lambda(\mathrm{k})$ is the mean free path of the photoelectron. This term can be interpreted as the probability for the photoelectron to travel to the scattering atom and back again while core hole is not filled by another electron.

The Passive Electron Reduction Factor

The S_0^2 term in the XAFS Eq. 2.3 is usually called the passive electron reduction factor[18]. Its value is completely determined by the absorbing atom where the passive electrons include all the electrons except the photoelectron. These electrons were neglected in my initial consideration of the initial and final states for the probability of the absorption of an x-ray. If these electrons are completely passive, they do not react to the absorption of the x-ray, then their contributions to the initial and final states are identical. The overlap of identical states gives unity which justifies their omission. In fact, the final state of these passive electrons may differ from the initial state because after the core electron has been freed from the atom the remaining passive electrons are pulled further in by the net positive charge of the nucleus. However, since the core hole life time is only about 10^{-15} seconds the passive electrons may not have time to fully adjust to the new potential. If the electrons react the potential of the absorbing atom, it is considered screened, otherwise, it is unscreened. The net effect of these passive electrons is to attenuate the XAFS signal. Values for S_0^2, therefore, range from 0.7 to 1.0 where 1.0 represents an fully screened potential.

Many Single Scattering Paths

A photoelectron can be considered a wave (see Fig. 2.2) which scatters from all the neighboring atoms. We can think of this as many pieces of the photoelectron scattering once from the neighboring atoms before the scattered pieces recombine with the original wave at the absorbing atom. Each piece of the photoelectron travels along a single scattering path. The XAFS equation for many single scattering paths is simply the sum of all the single scattering contributions described in detail above. Thus, the XAFS equation is written as $\chi(\mathrm{k}) = \sum_i \chi_i(\mathrm{k})$ where the sum is over all single scattering paths of the photoelectron and $\chi_i(k)$ is defined in Eq. 2.3.

It is convenient to consider equivalent single scattering paths since all identical atoms at the same radial distance from the absorbing atom give identical contributions to the XAFS signal. Often, I will refer to the equivalent paths by the coordinate shell or the nearest neighbor number of the neighboring atoms since it is these atoms that define the photoelectron path. A coordinate shell or the nearest neighbor is defined as all the atoms with the same average radial distance from the absorbing atom. In this context, the equivalent single scattering path is understood to be from the absorbing

atom to one atom in the shell and then back to the absorbing atom. To modify the summation, the XAFS equation must be multiplied by the number of atoms in the coordinate shell. The XAFS equation becomes $\chi(\mathrm{k}) = \sum_i \mathrm{N}_i \chi_i(\mathrm{k})$ where the sum is over the number of shells and N_i is the degeneracy of the shell.

This process introduces some error due to the thermal and static disorder which accounts for the true radial distance to each atom in the shell. If the disorder within the shell is assumed to be Gaussian about the average distance, r_i, a Debye-Waller factor type term similar to that used in x-ray diffraction measurements is added to the XAFS equation and is written as,

$$\mathrm{e}^{-2\mathrm{k}^2\sigma_i^2}. \tag{2.9}$$

The factor σ_i is the relative mean square displacement (RMS) between the atoms pairs which define the path length r_i.

The final form of the XAFS equation is

$$\chi(\mathrm{k}) = \sum_i \frac{\mathrm{N}_i \mathrm{S}_0^2 \mathrm{F}_i(k)}{\mathrm{kr}_i{}^2} e^{-\frac{2\mathrm{r}_i}{\lambda(\mathrm{k})} - 2\mathrm{k}^2\sigma_i^2} \sin(2\mathrm{kr}_i + \delta_i(\mathrm{k})) \tag{2.10}$$

where the sum is over coordinate shells for a specific atom type, N_i is the number of atoms in the shell and r_i is the radial distance to the shell.

After a brief description of the generalizations of this XAFS equation to account for multiple scattering of the photoelectron and non-symmetric disorder of the atoms within a shell the data analysis method, including the theoretical model of XAFS and the parameters used to extract the structural information, is presented.

2.1.3 Extras in the XAFS Equation

Two important additions to the XAFS Eq. 2.10 have been overlooked. They are the multiple scattering events and the cumulant expansion, the latter accounting for non-symmetric disorder within a coordinate shell.

Multiple Scattering

A multiple scattering event is one where the photoelectron scatters from more than one neighbor before it returns to the absorbing atom. As described in Refs. [19] and [20] the contribution of these events to the XAFS equation can be included without

changing the basic form of Eq. 2.10. There are two important advances that have aided in the development of the multiple scattering formalism. First, the use of the plane-wave approximation to quickly judge the importance of a multiple scattering path so that only a small fraction of the total are actually calculated. Second, the curved-wave multiple scattering formalism of Rehr and Albers [21]. Briefly, this formalism includes a scheme for a separable representation of the propagator which uncouples the product of scattering matrices as discussed below.

The fundamental idea is that the contribution from each multiple scattering event can be cast into a form which is equivalent to a single scattering event. This is accomplished by generalizing the basic elements in the XAFS equation which for comparison is written again:

$$\chi(\mathrm{k}) = \sum_i \frac{\mathrm{N}_i \mathrm{S}_0^2 \mathrm{F}_i(k)}{\mathrm{kr}_i{}^2} e^{-\frac{2\mathrm{r}_i}{\lambda(\mathrm{k})} - 2\mathrm{k}^2\sigma_i^2} \sin(2\mathrm{kr}_i + \delta_i(\mathrm{k})) \tag{2.11}$$

and now in terms of single and multiple scattering this equation is written as

$$\chi(\mathrm{k}) = \sum_\Gamma \frac{\mathrm{N}_\Gamma \mathrm{S}_0^2 |F_{\mathrm{eff}}^\Gamma(\mathrm{k})|}{\mathrm{kR}_{\mathrm{eff}}^2} e^{-\frac{2\mathrm{R}_{\mathrm{eff}}}{\lambda(\mathrm{k})} - 2\mathrm{k}^2\sigma_\Gamma^2} \sin(2\mathrm{kR}_{\mathrm{eff}} + 2\delta_c(\mathrm{k}) + \phi^\Gamma(\mathrm{k})) \tag{2.12}$$

The form of these two equations are very similar although many of the fundamental ideas have changed. The major changes are: in the sum where $i \rightarrow \Gamma$, the path length where $2r_i \rightarrow 2\mathrm{R}_{\mathrm{eff}}$, the scattering amplitude and phase where $\mathrm{F}_i(k) \rightarrow |F_{\mathrm{eff}}^\Gamma(\mathrm{k})|$ and $\delta_i(\mathrm{k}) \rightarrow 2\delta_c(\mathrm{k}) + \phi^\Gamma(\mathrm{k})$ and the relative mean square displacement where $\sigma_i^2 \rightarrow \sigma_\Gamma^2$. Each of these changes are described below.

The sum in Eq 2.11 over the i shells for a single scattering path becomes a sum of equivalent paths, Γ, in Eq. 2.12. Similarly, the degeneracy, N_i, of each shell for a single scattering contribution becomes the number of equivalent paths, N_Γ. For a single scattering event these symbols are the same and often I will refer to them in the single scattering context.

The path length $2\mathrm{r}_i$ used in Eq. 2.11 is the distance the photoelectron travels to the neighboring atom and then back to the original atom. Therefore, r_i simply represents the radial distance to the neighboring atom. In terms of multiple scattering $2\mathrm{r}_i \rightarrow 2\mathrm{R}_{\mathrm{eff}}$ where $2\mathrm{R}_{\mathrm{eff}}$ is the total path length of the photoelectron. For example if the photoelectron scatters from two atoms, atom A located at $\vec{\mathrm{r}}_\mathrm{A}$ and atom B located at $\vec{\mathrm{r}}_\mathrm{B}$ and the absorbing, "central", atom is located at $\vec{\mathrm{r}}_\mathrm{C}$ then the total path length

becomes $2\mathrm{R}_{\mathrm{eff}} = |(\vec{\mathrm{r}}_{\mathrm{A}} - \vec{\mathrm{r}}_{\mathrm{C}})| + |(\vec{\mathrm{r}}_{\mathrm{B}} - \vec{\mathrm{r}}_{\mathrm{A}})| + |(\vec{\mathrm{r}}_{\mathrm{B}} - \vec{\mathrm{r}}_{\mathrm{C}})|$. Each term in parenthesis is called a leg of the scattering path. As required for a single scattering event both $2\mathrm{r}_i$ and $2\mathrm{R}_{\mathrm{eff}}$ have the same meaning.

The scattering amplitude, $\mathrm{F}_i(k)$, of Eq. 2.11 is the amplitude of the part of the original photoelectron which is scattered from the neighboring atom. In terms of the multiple scattering this is replaced by an "effective" scattering amplitude, $|F^{\Gamma}_{eff}(k)|$, which is the product of $N-1$ scattering matrices where N is the number of legs of the path. This "effective" scattering amplitude takes into account the scattering angle between the incoming and outgoing directions of the photoelectron as well as the distance to each scatterer and curved wave effects. Each of these matrices are coupled since the amplitude and direction of the photoelectron scattered from atom A, of our previous example, determines in part the amplitude and direction of the photoelectron wave scattered from atom B. The separable representation of this product is one of the recent advances of the Rehr and Albers formalism which makes the multiple scattering computationally feasible.[1] The phase shift, $\phi^{\Gamma}(\mathrm{k})$, is the "effective" scattering phase associated with the product of these complex scattering matrices. $2\delta_c(k)$ is simply twice the central atom phase shift. Both of these terms, $2\delta_c(k) + \phi^{\Gamma}(\mathrm{k})$, were included in $\delta_i(\mathrm{k})$ of the single scattering equation.

The mean square displacement, $\sigma^2_{\Gamma} = \langle\langle \delta R_{\mathrm{eff}} \rangle\rangle$, accounts for the total variation in the path.

Including the multiple scattering events in this transparent manor allows these paths to be easily included in the analysis of the XAFS data. The geometry of these paths can be determined in a fit to the data giving a direct measure of disorder.

Cumulant Expansion

The cumulant expansion accounts for disorder in the atom's radial position and comes about since we are summing over the average path length and multiplying by the number of equivalent paths. As discussed in the Sec. 2.1.2 the first order correction is the addition of a Debye-Waller type factor which accounts for Gaussian disorder about an average radial distance. This correction describes the thermal disorder of atoms in a symmetric potential and is necessary since the time scale for XAFS goes

[1] The algorithm FEFF that calculates the theoretical model takes its name from $|F^{\Gamma}_{eff}(k)|$ because of its central role in the calculation.

like the core-hole lifetime (approximately 10^{-15} seconds) and the frequency for the vibration of the atoms is several orders of magnitude smaller, therefore XAFS gives an instantaneous "snapshot" of the position of all the atoms. Higher order terms in the cumulant expansion account for non-symmetric disorder.

Since the cumulant expansion is rarely worked out in detail, I will do so here. This involves taking a thermodynamic average of the XAFS equation, expanding several terms in a Taylor series, and then applying the definition of the cumulants. The final corrections to the phase and amplitude of the XAFS equation are derived from the cumulants and shown at the end of this section in Eq. 2.26. Finally the XAFS equation is rewritten in Eq. 2.27 to include these terms.

To include all orders of the cumulant expansion the sum about the average atom position should be replaced by a sum over the a thermodynamic average of the contribution from each atoms average position. The most important term in the thermodynamic average depends on the radial distance r_i to the neighboring atom. Removing these terms from the XAFS Eq. 2.10 gives

$$\left\langle \frac{e^{i2kr_i} e^{-2r_i/\lambda}}{{r_i}^2} \right\rangle_T . \tag{2.13}$$

If r_i is replaced with R_0+x were R_0 is the average position and x is a small displacement the thermal average becomes

$$\frac{e^{i2kR_0} e^{-2R_0/\lambda}}{{R_0}^2} \left\langle \frac{e^{i2kx} e^{-2x/\lambda}}{1 + (\frac{x}{R_0})^2} \right\rangle_T . \tag{2.14}$$

The largest contribution is from the phase term e^{i2kr_i}. A Taylor series expansion, therefore, of the smaller terms is written as:

$$\frac{e^{-2x/\lambda}}{1 + (\frac{x}{R_0})^2} \sim \left[1 - \left(\frac{2}{\lambda} + \frac{2}{R_0} \right) x + \left(\frac{2}{\lambda^2} + \frac{4}{R_0 \lambda} + \frac{3}{{R_0}^2} \right) x^2 \right]. \tag{2.15}$$

Substituting this expansion into Eq. 2.14 noting that the product of x and the exponential can be rewritten in terms of a partial derivative with respect to k, I can take all but the largest term out of the thermal average. The product of terms and the

remaining thermal average is given by

$$\frac{\mathrm{e}^{\mathrm{i2kR_0}}\mathrm{e}^{-2\mathrm{R_0}/\lambda}}{\mathrm{R_0}^2}\left[1-\left(\frac{2}{\lambda}+\frac{2}{\mathrm{R_0}}\right)\frac{1}{2\mathrm{i}}\frac{d}{d\mathrm{k}}+\left(\frac{2}{\lambda^2}+\frac{4}{\mathrm{R_0}\lambda}+\frac{3}{\mathrm{R_0}^2}\right)\left(\frac{1}{2i}\right)^2\frac{d^2}{d\mathrm{k}^2}\right]\left\langle \mathrm{e}^{\mathrm{i2kx}}\right\rangle_{\mathrm{T}}. \tag{2.16}$$

The last term within the thermal average can be rewritten in terms of the cumulant expansion. The definition of the cumulants, denoted C_n, as defined in Ref. [22] are written as

$$\exp\left(C_1\mathrm{t}+\frac{C_2\mathrm{t}^2}{2!}+\ldots+\frac{C_n t^n}{n!}+\ldots\right)\equiv 1+\langle\mathrm{r}\rangle t+\frac{\langle\mathrm{r}^2\rangle t^2}{2!}+\ldots+\frac{\langle\mathrm{r}^\mathrm{n}\rangle t^2}{n!}+\ldots \tag{2.17}$$

where $\langle\mathrm{r}^\mathrm{n}\rangle$ denotes the n-th moment of the distribution. Taking the logarithm of this definition and expanding the right side in terms of a power series,

$$\log(1+\mathrm{x})=\mathrm{x}-\frac{\mathrm{x}^2}{2}+\frac{\mathrm{x}^3}{3}-\frac{\mathrm{x}^4}{4}+\ldots, \tag{2.18}$$

and matching like powers of t gives the first four cumulants:

$$\begin{aligned}
\Delta\mathrm{r} &= C_1=\langle\mathrm{r}\rangle\\
\sigma^2 &= C_2=\langle(\mathrm{r}-\langle\mathrm{r}\rangle)^2\rangle=\langle\mathrm{r}^2\rangle-\langle\mathrm{r}\rangle^2\\
C_3 &= \langle(\mathrm{r}-\langle\mathrm{r}\rangle)^3\rangle=\langle\mathrm{r}^3\rangle-3\langle\mathrm{r}^2\rangle\langle\mathrm{r}\rangle+2\langle\mathrm{r}\rangle^3\\
C_4 &= \langle(\mathrm{r}-\langle\mathrm{r}\rangle)^4\rangle-3\langle(\mathrm{r}-\langle\mathrm{r}\rangle)^2\rangle^2\\
&= \langle\mathrm{r}^4\rangle-3\langle\mathrm{r}^2\rangle^2-4\langle\mathrm{r}^3\rangle\langle\mathrm{r}\rangle+12\langle\mathrm{r}^2\rangle\langle\mathrm{r}\rangle^2-6\langle\mathrm{r}\rangle^4
\end{aligned} \tag{2.19}$$

The first and second cumulants are just the average position and the mean square displacement term introduced in the preceding section. Written in terms of this cumulant expansion our thermal average becomes

$$\left\langle \mathrm{e}^{\mathrm{i2kx}}\right\rangle_{\mathrm{T}}=\exp\left[\sum_{n=1}^{\infty}\frac{(2\mathrm{ik})^n}{n!}C_n\right] \tag{2.20}$$

where t has been replaced with 2ir. Substituting this expression into equation 2.16, taking the partial derivatives with respect to k and keeping only the largest terms we

are left with

$$\frac{\mathrm{e}^{\mathrm{i2k(R_0+\Delta r)}}\mathrm{e}^{-2\mathrm{R_0}/\lambda}}{\mathrm{R_0}^2}\mathrm{e}^{-2\sigma^2k^2-\frac{4}{3}\mathrm{i}C_3k^3+\frac{2}{3}C_4k^4}\left[1-\mathrm{i}\left(\frac{1}{\lambda}+\frac{1}{\mathrm{R_0}}\right)4\sigma^2\mathrm{k}-\frac{2\Delta\mathrm{r}}{\mathrm{R_0}}-\frac{2\Delta\mathrm{r}}{\lambda}\right]. \quad (2.21)$$

The terms in the square brackets are small so we can approximate them as a product given by

$$\left[1-\frac{2\Delta\mathrm{r}}{\mathrm{R_0}}\right]\left[1-\mathrm{i}\left(\frac{1}{\lambda}+\frac{1}{\mathrm{R_0}}\right)4\sigma^2\mathrm{k}\right]\left[1-\frac{2\Delta\mathrm{r}}{\lambda}\right]. \quad (2.22)$$

The left term is just the Taylor series expansion of $(1+\frac{\Delta\mathrm{r}}{\mathrm{R_0}})^{-2}$. The imaginary part, in the middle term, and the real part in the left most term are small so they can be approximated by an exponential written as:

$$\exp\left[-\frac{4i\sigma^2\mathrm{k}}{\mathrm{R_0}}(1+\frac{\mathrm{R_0}}{\lambda})-\frac{2\Delta\mathrm{r}}{\lambda}\right]. \quad (2.23)$$

Putting both of these pieces back into Eq. 2.21 gives

$$\frac{\mathrm{e}^{\mathrm{i2k(R_0+\Delta r)}}\mathrm{e}^{-2(\mathrm{R_0}+\Delta\mathrm{r})/\lambda}}{(\mathrm{R_0}+\Delta\mathrm{r})^2}\cdot\exp\left[-2\sigma^2k^2+\frac{2}{3}C_4k^4\right]\cdot\exp\left[-\frac{4}{3}\mathrm{i}C_3k^3-\frac{4i\sigma^2\mathrm{k}}{\mathrm{R_0}}(1+\frac{\mathrm{R_0}}{\lambda})\right]. \quad (2.24)$$

For comparison, the original piece of the XAFS equation which will be replaced by Eq. 2.24 is written as

$$\left\langle\frac{\mathrm{e}^{\mathrm{i2kr}_i}\mathrm{e}^{-2\mathrm{r}_i/\lambda}}{\mathrm{r}_i^{\,2}}\right\rangle_{\mathrm{T}} \quad (2.25)$$

Comparing Eq. 2.24 and Eq. 2.25, we find that r_i has been replaced by $(\mathrm{R_0}+\Delta\mathrm{r})$ where $\Delta\mathrm{r}$ is the first order cumulant and the XAFS equation is modified by the addition of the amplitude term, A', and a phase term, ϕ', given by

$$\begin{aligned} A' &= \mathrm{e}^{-2\sigma^2k^2+\frac{2}{3}C_4k^4} \\ \phi' &= -\frac{4}{3}C_3k^3-\frac{4\sigma^2\mathrm{k}}{\mathrm{R_0}}(1+\frac{\mathrm{R_0}}{\lambda}) \end{aligned} \quad (2.26)$$

Here the first order correction to the amplitude was introduced previously as the Debye-Waller factor term $\mathrm{e}^{-2\sigma^2k^2}$. Including these modifications to the XAFS equation

the final form is written as

$$\chi(\mathrm{k}) = \sum_i \frac{\mathrm{N}_i \mathrm{S}_0^2 \mathrm{F}_i(k)}{\mathrm{kr}_i{}^2} e^{\frac{2\mathrm{r}_i}{\lambda(\mathrm{k})} - 2\mathrm{k}^2\sigma_i^2 + \frac{2}{3}C_4 k^4} \sin\left[2\mathrm{kr}_i + \delta_i(\mathrm{k}) - \frac{4}{3}C_3 k^3 - \frac{4\sigma^2\mathrm{k}}{\mathrm{r}_i}(1 + \frac{\mathrm{r}_i}{\lambda})\right] \tag{2.27}$$

where $\mathrm{r}_i = \mathrm{R}_{0i} + \Delta\mathrm{r}_i$. It is important to note that the disorder introduced by the cumulant expansion is model independent and is therefore applicable to a wide variety of systems and can be included in a path by path basis when the higher order cumulants are found necessary to describe the XAFS data.

2.2 Data Analysis

In an XAFS experiment the incident and transmitted x-ray intensities are measured as a function of energy. The intensity of the x-rays after passing through a sample of thickness x is given by

$$\mathrm{I} = \mathrm{I}_0 \mathrm{e}^{-\mu(\mathrm{E})\cdot\mathrm{x}} \tag{2.28}$$

where I_0 is the incident intensity, E is the incident energy of the x-rays, and $\mu(\mathrm{E})\cdot\mathrm{x}$ is the energy dependent absorption coefficient times the sample thickness x. The product of $\mu(\mathrm{E})\cdot\mathrm{x}$ is obtained experimentally by taking the logarithm of the ratio of I_0 to I. $\mu(\mathrm{E})\cdot\mathrm{x}$ data for copper is shown in Fig. 2.1a.

The next step is to isolate the XAFS signal in $\mu(\mathrm{E})\cdot\mathrm{x}$ and perform a Fourier transform to R-space. The theoretical model is then fitted to the data and local structure parameters are extracted. Each of these steps is discussed in more detail in the following sections.

2.2.1 Isolation of the XAFS Signal

An example of the isolated XAFS signal, $\chi(k)$, is shown in Fig. 2.1b. $\chi(\mathrm{E})$ is defined as the normalized oscillatory part of the x-ray absorption coefficient which is written as

$$\chi(\mathrm{E}) \equiv \frac{\mu(\mathrm{E})\cdot\mathrm{x} - \mu_0(\mathrm{E})\cdot\mathrm{x}}{\mu_0(\mathrm{E})\cdot\mathrm{x}} \tag{2.29}$$

where $\mu(\mathrm{E})\cdot\mathrm{x}$ is the measured data shown in Fig. 2.1a and $\mu_0(\mathrm{E})\cdot\mathrm{x}$ is the absorption coefficient times the sample thickness which would result if the scattered parts of the photoelectron from the surrounding atoms were turned off. The data, $\mu(\mathrm{E})\cdot\mathrm{x}$, contains some low frequency structure due to scattering of the photoelectron from the changing potential of the surrounding atoms, therefore $\mu_0(\mathrm{E})$ is not the absorption coefficient for an isolated atom and it is difficult to determine either from first principles or experimentally. In this thesis AUTOBK is used to generate $\mu_0(\mathrm{E})\cdot\mathrm{x}$. This procedure is outlined in Sec. 2.2.1. Examples of AUTOBK input files can be found in the AUTOBK documentation [23].

$\chi(\mathrm{E})$ is usually expressed as a function of photoelectron wave number k. As

discussed in Sec. 2.1.1, the wave number is given by:

$$k = \sqrt{2\mathrm{m}(\mathrm{E} - \mathrm{E}_0)/\hbar^2} \tag{2.30}$$

where E_0 is the Fermi energy chosen to be the value at approximately the middle of the edge step (see Sec. 2.1.1) as shown in Fig. 2.3.

Determination of $\mu_0(E)\cdot x$

The actual form of $\mu_0(\mathrm{E})\cdot\mathrm{x}$ is unknown but this is not a serious problem for XAFS as long as the contribution to $\chi(\mathrm{E})$ from the neighboring atoms contains frequencies which are much larger than that of the background, $\mu_0(\mathrm{E})\cdot\mathrm{x}$.

Based on information theory, AUTOBK, calculates an approximation to $\mu_0(\mathrm{E})\cdot\mathrm{x}$ which will not interfere with the XAFS data. The general principle is based on the Fourier transform conjugate variables k and $2R$. The signal in R-space of the Fourier transformed $\chi(k)$ corresponds to a frequency in the k-space $\chi(k)$. This implies that the first neighbor distance sets a low frequency limit for the k-space data. All frequencies less than this limit are not part of the data and are therefore subtracted. The minimum frequency of the relevant data therefore determines a maximum frequency for the background. The background frequencies correspond to peaks at R values that are less than the first nearest neighbor distance. AUTOBK uses this maximum background frequency to calculate $\mu_0(\mathrm{E})\cdot\mathrm{x}$ that minimizes the signal in the Fourier transform of $\chi(k)$ in the region from zero to $\mathrm{R}_{\mathrm{bkg}}$ where $\mathrm{R}_{\mathrm{bkg}}$ is typically set to half the first neighbor distance.

One important contribution to signal at low R has been overlooked. Some "leakage" of the first neighbor signal can extend into the low R range because of the finite data range. The best method for keeping this part of the spectrum is to include a theoretical calculation of $\chi(k)$ in the AUTOBK procedure. Then AUTOBK will minimize the difference between the data and the theoretical calculation in R-space between zero and $\mathrm{R}_{\mathrm{bkg}}$. Using this approach $\mu_0(\mathrm{E})\cdot\mathrm{x}$ determined by AUTOBK contains all the contributions to the data that are not due to the scattered photoelectron from the surrounding atom. This includes the energy response of the detectors, any multi-electron excitations, and scattering of the photoelectron from the excited atom potential called AXAFS [24] and [25].

AUTOBK uses piecewise continuous fourth order splines, which are third order

polynomials, to construct μ_0(E)·x because they permit only one full oscillation in between knots which are the points that joins two of the splines. This sets the upper bound on the maximum frequency of the background preventing it from interfering with the frequencies contained in the XAFS data. The number of splines depends on R_{bkg} and is determined by the number of independent points available for the background. This is given by

$$N_{bkg} = \frac{2\Delta R \Delta k}{\pi} + 1 \tag{2.31}$$

where $\Delta R = [0, R_{bkg}]$ and Δk is the data range in k-space. The N_{bkg}-1 knots of the splines are evenly spaced in k-space and the abscissa is calculated so that the optimal background is obtained while the first and second derivatives of the splines at the knots are continuous. An example of μ_0(E)·x determined by AUTOBK is shown in Fig. 2.3.

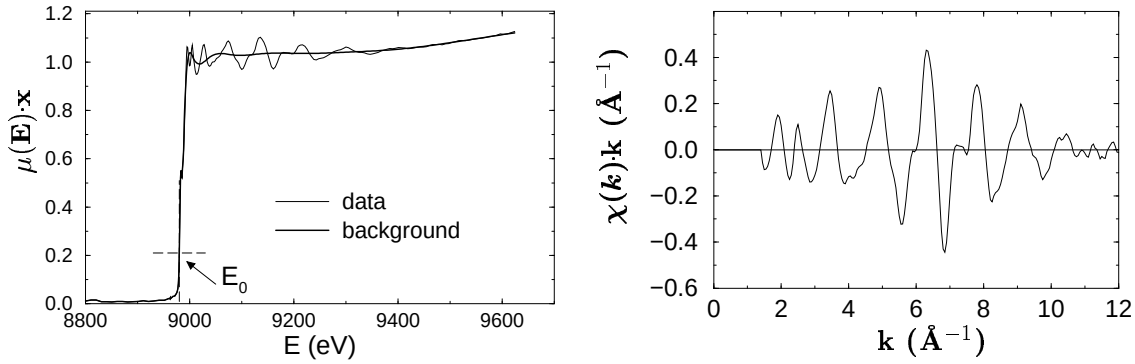

Figure 2.3: Left panel: An example of copper K-edge μ(E)·x data and the background function μ_0(E)·x calculated by AUTOBK. Right panel: The isolated XAFS signal, $\chi(k)\cdot k$, which is the difference between the μ(E)·x and μ_0(E)·x of the right panel weighted by k to emphasize the oscillations at high k. The wave number k is given by $k = \sqrt{2m(E - E_0)/\hbar^2}$ where E_0 is the energy threshold for the 1s electron excitation as labeled in the left panel.

Normalization

Before AUTOBK determines μ_0(E)·x, the pre-edge background is removed and the edge step normalized to 1.0. This procedure is referred to as normalization of the μ(E)·x

data and is done prior to the AUTOBK process so that the energy scale for all data sets can be easily aligned.

To normalize the edge step the μ(E)·x data is divided by $\Delta\mu_0(E_0)$. To determine this normalization factor a line is fitted to the pre-edge region of the absorption coefficient, defined as -200 to -50 eV before E_0, and to the post-edge region of the absorption coefficient, defined as 100 to 300 eV after E_0. These lines are then extrapolated to E_0 where their difference determines $\Delta\mu_0(E_0)$ which is essentially the magnitude of the edge step.

We do not divide by μ_0(E)·x determined by AUTOBK as described in the previous section because this function will follow any low frequency oscillations in the data due to experimental artifacts[2]. Errors due to the use of $\Delta\mu_0(E_0)$ are assumed to be small at the edge step where the absorption coefficient changes rapidly with energy.

When dividing by the constant $\Delta\mu_0(E_0)$ an energy dependent error is introduced. The ideal energy dependence of μ_0(E)·x is given by the energy dependence of the absorption cross-section of the absorbing atom and these values are tabulated in the McMaster tables[26]. This error is corrected by including an extra Debye-Waller factor coefficient to the XAFS Eq. 2.10. This factor, denoted as σ^2_{mcm}, is calculated by the code ATOMS and is determined by fitting the natural logarithm of the energy dependent cross section of the absorbing atom to a polynomial in energy.

Next the pre-edge background is removed. This is the linear part of the absorption coefficient due to the absorption of other atoms in the path of the x-rays and other absorption edges of the central atom. It is calculated by fitting a line to the absorption coefficient before the edge step and is the same line used to determine $\Delta\mu_0(E_0)$ as described above. The line is then extrapolated through the entire data range and then subtracted from the data. A very steep slope for a pre-edge line is an indication of a large total absorption coefficient. An example of a change in the pre-edge line slope is shown in Fig. 2.4 for copper inside and outside the pressure cell. The added absorption of the anvils for the data taken inside the pressure cell results in a steeper pre-edge background.

Two codes, NORMAL and E0ALI, have been written to produce normalized and aligned μ(E)·x data. These programs are often use with several sets of data since they determine the steepest part of the absorption edge and align the energy axes for

[2]For example, artifacts due to the energy response of the detectors and changes in the harmonic content of the x-ray beam

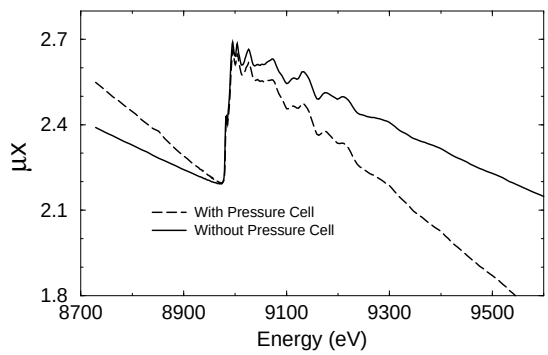

Figure 2.4: Example of K-edge μ(E)·x data for a copper sample inside and outside of the pressure cell. The addition of the anvils increases the total absorption by a factor of 1.23 resulting in a steeper background.

all data sets. This alignment process is necessary since the absolute energy scale of the monochromator often shifts slightly when moved through several thousand eV. Fig. 2.5 shows an example of copper K-edge μ(E)·x data before and after normalization.

Background Removal Procedure

For completeness I will elaborate on the background subtraction procedure. There are only two important values that need to be determined E_0 and R_{bkg}. E_0 determines k according to Eq. 2.30 and represents the Fermi energy as described in Sec. 2.1.1. R_{bkg} determines the number of knots used in the spline according to Eq. 2.31 and represents the maximum frequency of the background function. The steps for determining these parameters and removing the background are as follows:

- Data is normalized using either E0ALI or NORMAL. An alignment energy may be input or calculated as described previously. For consistency I choose the value at mid-point of the edge step. This produces normalized data as shown in Fig. 2.5.
- The background is removed from the normalized data using AUTOBK. A choice for R_{bkg} and E_0 must be made. To begin, I chose R_{bkg} equal to half the first nearest neighbor distance and E_0 equal to the value at the mid-point of the edge step as shown in Fig. 2.3.
- Once the background has been removed the resulting $\chi(k)$-data is given as

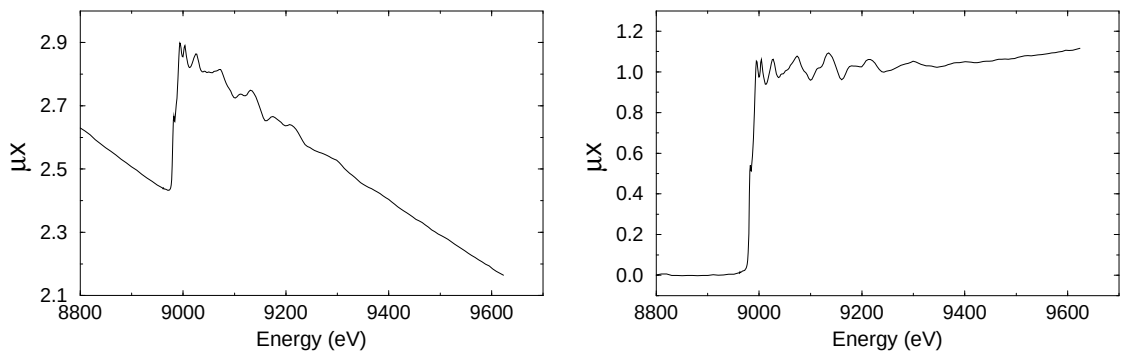

Figure 2.5: Example of Copper K-edge μ(E)·x data before and after normalization. E0ALI was given the edge energy of copper together with the data in the left panel. A line was fit to the pre-edge region and extrapolated through the entire data range and then subtracted from the data. The edge step is also normalized. The result is shown in the right panel.

input to FEFFIT, a theoretical model for the first shell is fitted to the data in R-space and a value for ΔE_0 is determined. This is a direct comparison of the value calculated for the Fermi energy by FEFF to the value used by AUTOBK which is usually set at half the edge step. Ideally ΔE_0 is about one eV. If the value is larger than a few eV then the value for E_0 given to AUTOBK in the second step needs to be adjusted accordingly and this step is repeated.

- Now that the data and theoretical model are reasonably aligned, the step height of the normalized data which corresponds to this value for E_0 is then determined. Fig. 2.3 shows this step height as a dashed line at 0.20 of the step. The intersection of this line with each data set determines the E_0 for each data set. Usually this corresponds to the same value for $E_0 \pm$ 1 eV for all data sets.
- Then the final background is removed using AUTOBK.

For simplicity I left out the determination of R_{bkg} which in the above procedure is left at the original value of half the first nearest neighbor distance. This value is usually adequate for an open structure where R_{bkg} is greater than 1.2 Å but may underestimate the maximum possible value for R_{bkg}. For structures where the first nearest neighbor distance is less than 2.5 Å the number of frequencies in the background as determined by R_{bkg} becomes so few that R_{bkg} must be chosen more carefully.

In this case FEFFIT can vary a spline which represents a background function based on a trial R_{bkg} value. FEFFIT then reports the correlation coefficients between the background and the fitted parameters. Iterating this process, R_{bkg} may be determined so that the background is reasonable. The most important restriction on R_{bkg} is that it cannot overlap with the fit range.

2.2.2 Fourier Transforms

Next, the Fourier transform of the data, $\chi(k)$, from k-space to R-space is considered. The theoretical model is fitted to the data in R-space which allows information from individual shells to be easily separated. An example, of transformed data for a copper sample is shown at the end of this section.

The Fourier transform of $\chi(k)$ is defined as

$$\tilde{\chi}(R) \equiv \frac{1}{\sqrt{2\pi}} \int_0^\infty k^w \chi(k) \mathrm{W}(k) \mathrm{e}^{\mathrm{i}2kr} \mathrm{d}k \tag{2.32}$$

where $\mathrm{W}(k)$ is the Fourier transform window and k^w is a k-weight used to emphasize the high-k region of $\chi(k)$. The effect of the Fourier transform window is to smooth the $\tilde{\chi}(R)$. In this work the default Hanning window, which is a piecewise continuous function that is zero outside the data range and equal to one over the data range, is used. The transition region, called the window sills, are governed by squared sine and cosine terms which are centered about the maximum and minimum k values. An example of the window for copper is shown in Fig. 2.6 where k_{min} and k_{max} are labeled. The expression for this window and the others that are available may be found in the FEFFIT documentation[27]. If k^w used in the Fourier transform of data is not given, the units of $|\tilde{\chi}(R)|$ can be used to determine its value. The power of the inverse Å minus one corresponds to the k-weighting.

In practice the integral equation for the Fourier transform is replaced by a fast Fourier transform which is a sum over points given by

$$\tilde{\chi}(R_m) = \frac{\mathrm{i} \cdot \delta k}{\sqrt{\pi \mathrm{N}_{\mathrm{fft}}}} \sum_{n=1}^{\mathrm{N}_{\mathrm{fft}}} k_n^w \tilde{\chi}(k_n) \mathrm{W}(k_n) \mathrm{e}^{\mathrm{i}2\pi nm/\mathrm{N}_{\mathrm{fft}}} \tag{2.33}$$

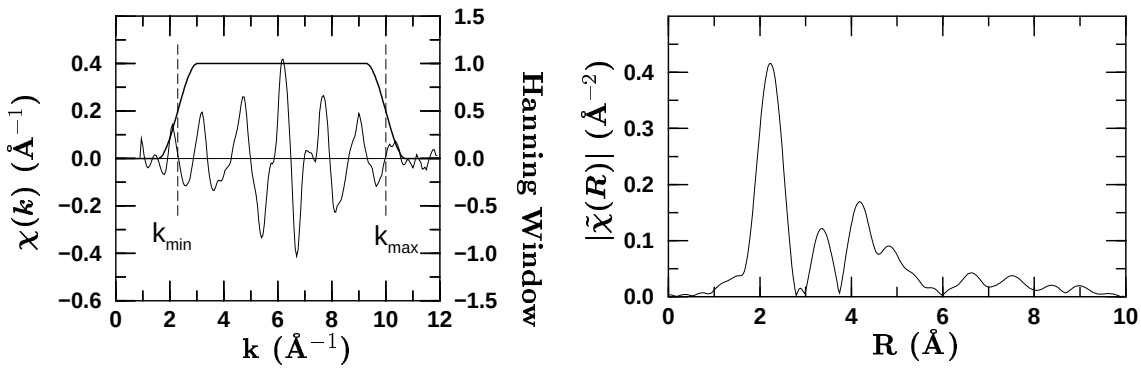

Figure 2.6: The left panel shows the $\chi(k)\cdot k$ data for copper along with the Hanning window used in the Fourier transform. The window is specified by the values $k_{\rm min}$ and $k_{\rm max}$ which should go through a node in the $\chi(k)$ data and dk which specifies the total width of the sills. In this example dk = 1.5 Å^{-1}. The right panel shows the result of the Fourier transform.

and

$$\tilde{\chi}(k_n) = \frac{2\mathrm{i}\cdot\delta\mathrm{R}}{\sqrt{\pi\mathrm{N}_{\rm fft}}}\sum_{n=1}^{\mathrm{N}_{\rm fft}} k_n^w \tilde{\chi}(R_m)\mathrm{W}(k_n)\mathrm{e}^{-\mathrm{i}2\pi nm/\mathrm{N}_{\rm fft}} \tag{2.34}$$

where $k_n = n\cdot\delta k$ and $\mathrm{R}_m = m\cdot\delta\mathrm{R}$. The k-space grid is $\delta k = 0.05$ Å^{-1} and the array sizes are $\mathrm{N}_{\rm fft} = 512$, 1024, or 2048. Details can be found in Ref. [27]. An important point is that measuring $\chi(k)$ at intervals smaller than the grid spacing is unnecessary since this information is not used in the fit. This grid spacing is small enough to resolve signals in R-space out to 31 Å, well beyond the required range of about 10 Å.

Fitting the theoretical model to the data in R-space allows the information from specific paths to be easily separated. For example, the face center cubic structure for copper means that the first and second nearest copper shells have a degeneracy of 12 and 6 respectively. For a unit cell length of $a = 3.61$ Å the first shell is at a distance of 2.55 Å from a central copper atom and well separated from the next shell at 3.61 Å, therefore, a model for the first shell alone can be fitted to the data in R-space from 1.6 to 2.8 Å. Fig. 2.7 shows the data and theoretical model in R-space and in k-space. These figures demonstrate how the long frequencies due to the first shell in k-space are separated from the higher frequencies of the other shells which are shown together with the noise in k-space. The theoretical models are discussed in the next

section.

2.2.3 Theoretical Models: FEFF

The basic ideas used in the FEFF calculation of the theoretical models are discussed here. These ideas are important in interpreting the fit results as explained in Ref. [28] where many important references to more detailed discussions can be found.

One of the goals of FEFF is to calculate a theoretical model in a way that requires very little expertise from the user. With this goal in mind FEFF requires the specification of the central absorbing atom and its relationship to its neighboring atoms including their type and position. Given this information FEFF calculates the expected XAFS signal represented by Eq. 2.10 with the passive-electron reduction factor, S_0^2, set to one and with no disorder represented by a zero Debye-Waller factor coefficient, σ^2. These options may be given as input but I will use FEFFIT, a code that fits the model to the data, to determine these parameters. FEFFIT is to be discussed in the next section.

The theoretical model on which FEFF is based comes from the theoretical framework of Ref.[15]. The model system is made up of a central absorbing atom with atomic number, Z_c, surrounded by N neighbors of atomic number, Z_n, at a distance, R, each of which are surrounded by N′ neighbors of their own. The absorbing atom is assumed to have a neutral atomic configuration. This is effectively what would be expected on a very short time scale in a conductor. In a conductor a free electron from the conduction band is attracted to the central atom by the Coulomb potential created by the core hole. This is approximated by the electronic configuration of the $Z_c + 1$ atom with the core electron removed. Effectively, one removes a core electron and places it in the next unoccupied electron state.

Next the "muffin-tin" potentials for each atom type within the model system are calculated. Then the atomic charge densities for each atom in the model are overlayed and spherically averaged about the atomic centers. These spherically averaged densities are then integrated out to the "Norman" radius, R_{nm}, where the total charge is equal to the atomic number of the atom. The muffin-tin radius, R_{mt}, is calculated by proportionally decreasing R_{nm} until the spheres of radius R_{mt} just touch. The interstitial potential and charge density is determined by averaging the charge left between R_{mt} and R_{nm} for all atoms. This model for the atom potential works best for monatomic solids but may overestimate the interstitial charge density in open

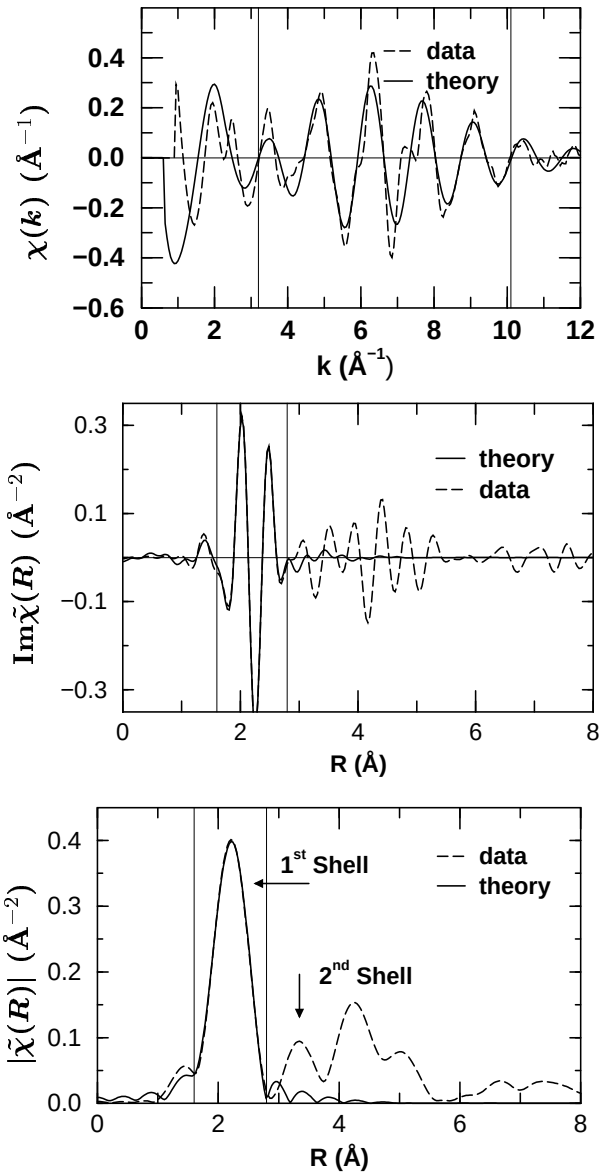

Figure 2.7: Top: $\chi(k)$-data and theoretical model for copper. The vertical line represent the data range, $k_{\min}$ and $k_{\max}$. Middle: Im $\tilde{\chi}(R)$-data and theoretical model. Bottom: $|\tilde{\chi}(R)|$ data and theoretical model. The theoretical model includes the scattering paths from the 12 copper atoms of the first shell only. The vertical lines represent the fitting range.

structures and molecules. This error can be partially corrected for by adding additional energy shifts to the equation for the photoelectron wave number which travels between these "muffin-tin" potentials which represent the atomic potentials in the solid (see Eq. 2.37 to be discussed in the next section). Additional energy shifts are used to model RbCl, AgCl and AgBr as discussed in Chs. 5 – 7.

After the atomic potential are calculated the energy reference is determined. The energy reference, experimentally set to approximately half the edge step, is fundamentally the Fermi energy which lies at the last filled electron state of the solid. It is represented by the chemical potential, μ, of a homogeneous electron gas at the average interstitial charge density. This approximation tends to be a few eV higher than that calculated from self-consistent calculations which are a part of FEFF8 but not used in this thesis.

With a model for the atomic potentials and the energy reference calculated, the scattering amplitude of the photoelectron from these atomic potentials is determined. The unperturbed system consists of a photoelectron with some energy and angular momentum moving in a uniform electron gas with charge density of the interstitial region containing a complex part to account for energy losses[29]. This is a representation the photoelectron in the region in between the atoms were phonon vibrations and other interactions can cause the photoelectron to lose energy. The perturbation is the scattering from the muffin-tin potentials centered at the atomic sites. This is a representation of the actual scattering of the photoelectron from the surrounding atoms. The Partial-wave phase shifts are determined by matching the solutions to free spherical waves in the complex interstitial scattering potential to the XAFS equation.

The results of the FEFF calculation are in terms of the effective scattering amplitude, total phase shift and mean free path of the photoelectron as a function of wave number for all possible scattering paths of the photoelectron. Splitting up the contribution to the XAFS signal from each scattering path is important for the analysis of the data. As discussed in Sec. 2.2.2, the magnitude of the Fourier transform of the XAFS data, $|\tilde{\chi}(R)|$, peaks at positions related to the half path length of the photoelectron. In the fitting process we choose the fitting range in R-space which corresponds to particular scattering paths. Since FEFF outputs its results for every scattering path the model includes only the paths that contribute to the fitting range in R-space. (see Fig. 2.7)

2.2.4 Fitting Theoretical Model to Data: FEFFIT

The theoretical model of FEFF is fitted to the data using FEFFIT[27]. The model, χ_{model}, used by FEFFIT is written as

$$\chi_{\mathrm{model}}(k) = \sum_{j}^{\mathrm{N_{paths}}} \mathrm{Im}[\tilde{\chi}_j(k)] \tag{2.35}$$

where $\mathrm{N_{paths}}$ are only the paths that contribute to the fitting range in R-space and $\tilde{\chi}_j(k)$ is the complex contribution from each path. The contribution from each path used by FEFFIT is very similar to our previous expressions for the XAFS Eq. 2.27. A physical interpretation of each of the components of the XAFS equation are described in Sec. 2.1. There are a few differences between the XAFS Eq. 2.27 and the equation used by FEFF which make it desirable to look at the form used by FEFF and distinguish between the parts calculated by FEFF and those that may be varied in the fit.

$$\begin{aligned}\tilde{\chi}_j(\mathrm{k}) =& \frac{(\mathbf{N}_j\mathbf{S_0^2})\mathrm{F}_j(k)}{\mathrm{k}(\mathrm{R}_{0j} + \Delta\mathbf{R}_j)^2} \exp\left\{-2p\mathrm{R}_{0j} - 2p^2\boldsymbol{\sigma_j^2} + \frac{2}{3}p^4\mathbf{C_{4j}}\right\} \\ &\cdot \exp\left\{i[2\mathrm{kR}_{0j} + \delta_j(\mathrm{k}) - \frac{4}{3}\mathbf{C_{3j}}p^3 + 2p(\Delta\mathbf{R}_j - 2\boldsymbol{\sigma_j^2}/\mathrm{R}_{0j})]\right\}\end{aligned} \tag{2.36}$$

Each of these terms is discussed in detail in the first three sections of this Chapter and only differences are discussed here. For simplicity the fitted parameters are shown in **bold** type. We have replaced r_i with $\mathrm{R}_0 + \Delta\mathbf{R}_j$ where R_0 is the half path length given as input to FEFF and $\Delta\mathbf{R}_j$ is a fit parameter. There are two momentum references p and k in Eq. 2.36. This is because FEFF calculates the XAFS as a function of p, the complex local momentum with respect to the zero of the muffin-tin potentials described in the previous section, and writes the scattering amplitudes, $\mathrm{F}_j(k)$, and phase shifts, $\delta_j(k)$, as a function of k_{feff}, the real momentum with respect to the Fermi energy. The value of k_{feff} is directly compared to the experimental value for E_0 chosen to be the energy at the midpoint of the edge step as described in Sec. 2.2.1. Because the Fermi energy calculated by FEFF is typically in error by a few eV, the scale can be shifted by fitting an energy shift, $\boldsymbol{\Delta}\mathbf{E_{0j}}$. The shifted scale is given by

$$k = \sqrt{k_{\mathrm{feff}}^2 - \boldsymbol{\Delta}\mathbf{E_{0j}}\frac{2m}{\hbar^2}}. \tag{2.37}$$

The complex momentum, p, can also be determined in a fit to the data and is given by the following expression

$$p = \sqrt{\left\{\mathrm{Re}[p_j(k)] + \frac{i\hbar}{\lambda_j(k)}\right\}^2 + i\boldsymbol{\Delta}\mathrm{Ei}_{\boldsymbol{j}}\frac{2m}{\hbar^2}}. \tag{2.38}$$

where $\mathrm{Re}[p_j(k)]$ and $\lambda_j(k)$ are taken from the FEFF calculation and $\boldsymbol{\Delta}\mathrm{Ei}_{\boldsymbol{j}}$, an imaginary energy shift, is a fitted broadening term to account for finite experimental resolution.

In this picture up to seven parameters for each path may be determined by a fit to the data. These parameters are: $(\mathbf{N_j S_0^2})$ the degeneracy of the path and an amplitude reduction factor, $\boldsymbol{\Delta}\mathrm{Ei}_{\boldsymbol{j}}$ a broadening term, $\boldsymbol{\Delta}\mathbf{E}_{0j}$ a shift in the energy reference, $\Delta\mathbf{R}_j$ a change in the half path length, $\boldsymbol{\sigma_j^2}$ a mean square displacement about the half path length and $\mathbf{C_{3}}_j$ and $\mathbf{C_{4}}_j$ the non-symmetric disorder terms. Not all of these parameters should be allowed to vary independently. Fortunately, FEFFIT is ideal for writing mathematical constraints in terms of these fundamental parameters.

For our previous copper example (see Fig. 2.7) the first shell requires 4 parameters: α = -0.0036(2), σ^2 = 0.0081(1) Å^2, S_0^2 = 0.68(1), ΔE_0 = 1.5(1) eV. Here all the parameters expect α are fundamental XAFS parameters described above. N was set to 12, the known degeneracy of the first copper shell. The third and fourth cumulants and the imaginary broadening parameters were not needed. α was defined in terms of Δr to represent the fractional change in the radial distance to the first shell, $\Delta r = \alpha \cdot R_{eff}$ where R_{eff} = 2.555 the original distance given to FEFF. This change of parameters is often used when the the distance to each shell is expected to change by the same fractional amount. Therefore a single α parameter can be used to determine the distance to each shell used in the fit.

FEFFIT also calculates several statistical quantities for judging the quality of the model. These quantities include: the number of independent points and the number of degrees of freedom in the data, several measures of the goodness-of-fit, and error estimation and correlation coefficients for fitted parameters.

The best-fit values determined by FEFFIT minimize the sum over f_i where f_i is the squares of the difference of the real and imaginary parts of the model and data

in R-space. This is written as

$$\sum_{\mathrm{i}=1}^{\mathrm{N}} f_{\mathrm{i}} = \sum_{\mathrm{i}=1}^{\mathrm{N}} \tilde{\chi}_{\mathrm{data}}(R_{\mathrm{i}}) - \tilde{\chi}_{\mathrm{model}}(R_{\mathrm{i}}). \tag{2.39}$$

Here, N is the number of evaluations of the function. The meaning of N is a bit tricky since the measurement of each point of $\mu(\mathrm{E})$ is independent but these points are not an independent measurements of the atomic distribution function that we are interested in finding the best-fit for. In analyzing the data one looks for a frequency in k-space. The resolution, therefore, depends on the length of the k-space data, the bandwidth, and the fitting range in R-space which specifies the frequency range. More precisely, the number of independent points in the data is given by

$$\mathrm{N}_{\mathrm{idp}} = \frac{2\Delta R \Delta k}{\pi} + 2 \tag{2.40}$$

where ΔR and Δk are the data ranges in R-space and k-space respectively[30]. The number of variables fitted to the data must be less than the number of independent points and their difference, ν, represents the degrees of freedom in the fit. The correct function to minimize in the Fourier transform analysis becomes

$$\sum_{\mathrm{i}=1}^{\mathrm{N}} f_{\mathrm{i}} = \frac{\mathrm{N}_{\mathrm{idp}}}{\mathrm{N}} \sum_{\mathrm{i}=1}^{\mathrm{N}} \tilde{\chi}_{\mathrm{data}}(R_{\mathrm{i}}) - \tilde{\chi}_{\mathrm{model}}(R_{\mathrm{i}}). \tag{2.41}$$

Goodness-of-Fit

The usual measure of the goodness-of-fit is chi-squared, χ^2, defined as

$$\chi^2 = \sum_{\mathrm{i}=1}^{\mathrm{N}} \left(\frac{f_{\mathrm{i}}}{\epsilon_{\mathrm{i}}} \right)^2 \tag{2.42}$$

where f_i is the difference between the data and fitted function as defined in Eq. 2.41, N is the number of function evaluations and ϵ_i are the uncertainties in the function[31]. As discussed above the number of functional evaluations in XAFS data does not have the usual significance expected in this definition. The quantity of importance in XAFS data analysis is the number of independent points so the definition for χ^2

becomes,

$$\chi^2 = \sum_{\mathrm{i}=1}^{\mathrm{N_{idp}}} \left(\frac{f_\mathrm{i}}{\epsilon_\mathrm{i}}\right)^2 = \frac{\mathrm{N_{idp}}}{\mathrm{N}} \sum_{\mathrm{i}=1}^{\mathrm{N}} \left(\frac{f_\mathrm{i}}{\epsilon_\mathrm{i}}\right)^2 . \tag{2.43}$$

The uncertainty in the measurement, ϵ_i, has both statistical and systematic contributions. Its contribution from statistical noise can be obtained by measuring the fluctuations in R-space between 15 and 25 Å. One assumes that there is no structural contribution in this range due to the exponentially decreasing Debye-Waller factor term in the XAFS equation which dominates for large R. With this interpretation ϵ no longer depends on i and can be brought out of the sum in Eq. 2.43. Other sources of uncertainty in the measurement include systematic experimental errors and uncertainties in the FEFF theoretical model itself. These uncertainties are difficult to estimate and are, therefore, left out of the calculation done by FEFFIT. This typically results in an overestimate of the value for χ^2.

A poorly scaled χ^2 is not a problem when comparing two different models where the value for ϵ is consistently chosen. In general the model with the lowest χ^2 is the best. For two models with a different number of variables the reduced-χ^2, χ^2_ν, should be compared. χ^2_ν is equal to χ^2 divided by, ν, the number of degrees of freedom in the fit. Therefore, if χ^2 decreases when adding an additional parameter but χ^2_ν increases, the fit has not been improved. In this way χ^2_ν can be used to determine the usefulness of a particular parameter.

Typical values for χ^2_ν are as large as several hundred making it difficult to establish the correctness of the model. Since large values of χ^2_ν may result from either a poor model or from an underestimation of the value of ϵ, FEFFIT also calculates an $\mathcal{R}$-factor defined as

$$\mathcal{R} = \frac{\sum_{\mathrm{i}=1}^{\mathrm{N}} \{[\mathrm{Re}(f_\mathrm{i})]^2 + [\mathrm{Im}(f_\mathrm{i})]^2\}}{\sum_{\mathrm{i}=1}^{\mathrm{N}} \{[\mathrm{Re}(\tilde{\chi}_{\mathrm{data_i}})]^2 + [\mathrm{Im}(\tilde{\chi}_{\mathrm{data_i}})]^2\}}. \tag{2.44}$$

to help distinguish between these two cases[31]. The $\mathcal{R}$-factor gives a sum of the fractional error and is directly proportional to χ^2. As long as the $\mathcal{R}$-factor is less than a few percent one is confident that the large χ^2_ν value comes from an underestimation in the systematic errors.

In our copper example the number of parameters determined in the fit is four and the number of independent points in the data is $\mathrm{N_{idp}} = 19$ as determined by Eq. 2.40

therefore the degrees of freedom in the fit is $\gamma = 15$. The $\mathcal{R}$-factor = 0.1%, $\chi^2 = 97$ and the $\chi^2_\nu = 6$. (see Fig. 2.7)

Error Estimation and Correlations

FEFFIT also calculates an estimated error and correlation coefficients for the fitted parameters. Similar to the procedure of Bevington[31], each parameter is varied about its best-fit value until the value of χ^2 increases by one from its minimum. The correlation coefficients range from zero to one and express the degree to which each parameters depends on the other parameters. All correlation coefficients greater than 25% are reported by FEFFIT.

Correlations greater than 80% need to be considered with special care. There are different methods for breaking these correlations depending on the type of parameters that are correlated. Most of the parameters have unique k-dependences which can be used to break the correlation by varying the k-weighting in relation Eq. 2.32. The amplitude parameters S_0^2 and σ^2 and the phase parameters $\Delta E_0{}^i$ and ΔR_i are examples of parameters which are often strongly correlated. For the phase parameters energy shifts dominate at low k, therefore, small k-weightings will give the best-fit values for energy shifts while the changes in the half path length dominate at high k, therefore, larger k-weightings will give the best values for the changes in the half path lengths. Another invaluable tool for breaking correlations is to use a parameter's expected dependence on an extrinsic parameter such as temperature and pressure. For example, the value for S_0^2 should be constant for all temperatures or pressures while one expects changes of the mean square displacements in the half path length as a function of temperature and/or pressure. In general, simultaneously fitting several k-weightings for a data set and several data sets at different pressures or temperatures is a powerful tool for breaking the correlation between parameters and is used extensively in this thesis.

For the copper example three k-weightings of $w = 1, 2, 3$ were used. The data was simultaneously fit to the corresponding data sets in R-space so that the best-fit values are independent of the k-weighting used in the analysis process. The uncertainty in the fit parameters was shown in the preceding section. The correlation coefficient for S_0^2 and σ^2 is 94% and for α and E_0 is 91%. Unfortunately FEFF calculates the correlation coefficients for a single k-weighting even when several are used. The reduction in the correlation coefficients due to the use of the different k-weightings is definitely not as

large as one might hope. The Chapter 4 shows how this can be estimated.

Chapter 3

XAFS EXPERIMENTS

A high pressure x-ray absorption fine structure (XAFS) experiment can be separated into three parts, the experimental setup, the sample preparation and the measurement. Each of these parts is discussed below.

3.1 Experimental Setup

Fig. 3.1 shows a schematic of an XAFS transmission experiment. The main components are: the monochromator used to select the x-ray energy, the pinhole used to define the cross section of the x-ray beam, the ion chambers used to sample the incident and transmitted x-ray intensities and the pressure cell and oil pump used to generate a high pressure sample. Each of these components is discussed in the following sections.

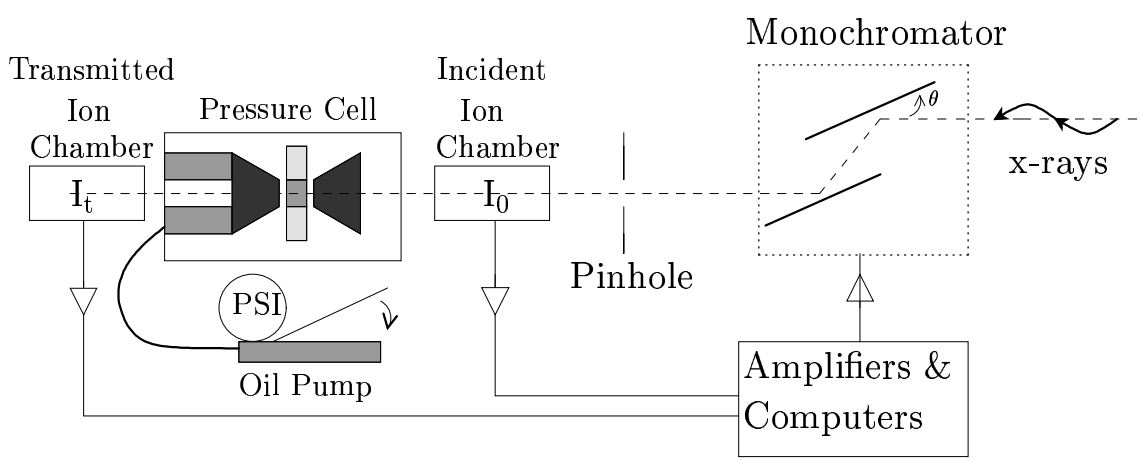

Figure 3.1: A schematic of a high pressure XAFS transmission experiment.

3.1.1 Monochromator

The main component of the monochromator is its two parallel silicon crystals. The first crystal is set at an angle θ with respect to the incoming x-ray beam to select the desired x-ray energy. The second crystal is set parallel to the first so that the x-ray beam is reflected in the direction of the experiment as shown in Fig. 3.1.

The x-ray energy selected by the monochromator is determined by the Bragg condition which states that the x-rays reflected from two neighboring planes of atoms must coherently interfere. This condition is satisfied when the extra distance traveled by the x-rays to the farther plane of atoms is equal to a multiple of the x-ray wavelength, i.e. $2d \cdot \sin\theta = m \cdot \lambda$ where m is an integer, as illustrated in the Fig. 3.2. For m greater than 1 the x-ray energy is called the (m-1)-th harmonic. From Bragg's condition the higher harmonics are selected along with the desired energy. There are many methods for eliminating the higher harmonics. Their elimination is necessary since they will distort the XAFS signal (see Sec. 3.3.2). The most common methods used in this thesis will be discussed here.

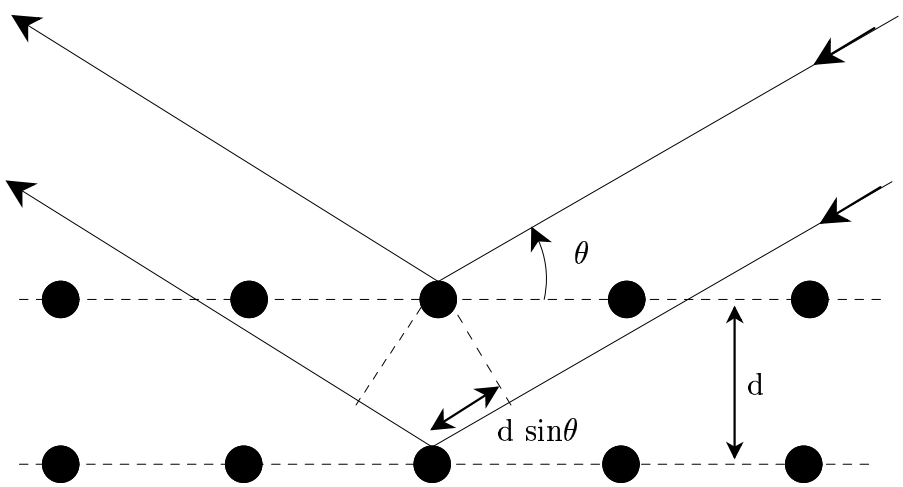

Figure 3.2: The Bragg condition, $2d \cdot \sin\theta = m \cdot \lambda$ where m is an integer, states that the x-rays reflected form two neighboring planes of atoms must coherently interfere. This means that the extra distance traveled by the x-rays to the farther plane of atoms must be equal to a multiple of the x-ray wavelength.

One of the simplest methods for completely eliminating several of the harmonics

is to choose a crystal cut in which, as a result of its basis, the two reflected x-rays completely destructively interfere. This is referred to as a zero structure factor for that particular harmonic. Ideally we would like to to choose a crystal with a zero structure factor for the second harmonic. This is because the second harmonic will have the greatest intensity of the harmonics due to the profile of the source. Briefly, the profile of the source has a maximum x-ray intensity at about 11.2 keV for Stanford Synchrotron Radiation Light Source (SSRL) and at about 4.3 keV for Brookhaven National Laboratory (BNL). The exponential decrease in the intensity leaves a usable x-ray energy range from about 3 keV to about 40 keV with virtually no intensity above 100 keV so that the second harmonic will have the greatest intensity of the harmonics and therefore we would like to eliminate it completely. The structure factor is determined by the cut of the crystal which is referred to by the (hkl) indices for the crystal plane parallel to the surface. Silicon has the diamond structure so a harmonic will have a zero structure factor if its wavelength given by m·$(h + k + l)$, where m is the harmonic number, is equal to twice an odd number[32]. Since we are interested in a zero structure factor for the second harmonic, the relation for this harmonic to vanish simply becomes $(h + k + l) =$ odd. Table 3.1 lists several common silicon monochromator crystals used at SSRL and BNL along with their lattice spacings, energy ranges and whether the second harmonic is allowed.

Table 3.1: Several silicon monochromator crystals, lattice spacings and energy ranges. The crystal cuts are referred to by the (hkl) indices for the plane parallel to the surface of the crystal. The energy range depends on the plane spacing and the size of the crystal which determines the θ range. Here we have used a minimum and maximum angles of 17° and 31° respectively to calculate the energy ranges. Second harmonics, are not allowed when the structure factor vanishes, h + k + l = odd[32].

h	k	l	2d (Å)	Energy range (keV)	Second harmonics
1	1	1	6.2708	5 to 26	not allowed
2	2	0	3.8400	12 to 42	allowed
3	1	1	3.2744	17 to 50	not allowed
4	0	0	2.7154	24 to 60	allowed

To further reduce the number of x-rays with high harmonic energy we slightly misalign the second crystal. This process is called detuning. Detuning works because

the profile of the x-rays with the high harmonic energies is much sharper with respect to θ than that of the x-rays with the fundamental energy. Taken from Ref. [33] Fig. 3.3 shows the reduction of higher harmonics by detuning. In this example the second silicon (111) crystal is misaligned by 3.5 arcsec at an energy of 10 keV. As shown in the figure the fundamental x-ray intensity is reduced to about 50% of its original intensity while the third harmonic x-ray intensity is reduced to about 0.01% of its original intensity. The second harmonic is not allowed because its structure factor vanishes.

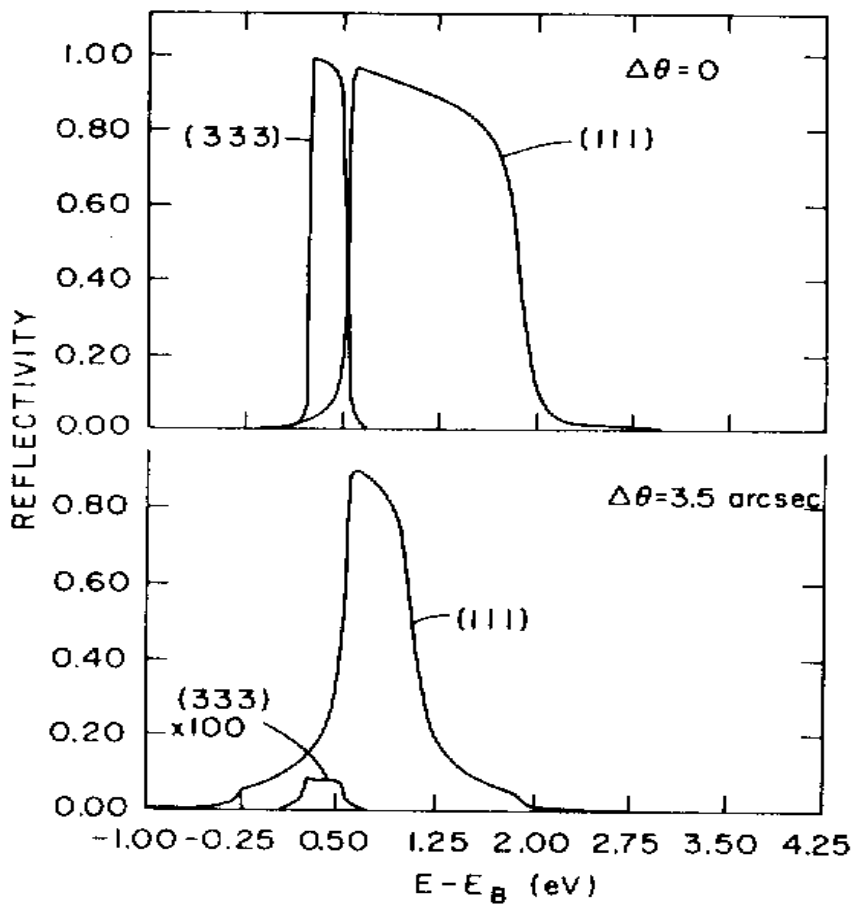

Figure 3.3: The reduction of harmonics by detuning. The silicon (111) crystal is misaligned by 3.5 arcsec at E_B=10 keV. The fundamental x-ray intensity is reduced by 50% while the third harmonic is reduced by 99.99% of their original intensities.

In practice, when we detune the monochromator, we monitor the percent decrease in the voltage reading of the I_0 ion chamber, which is directly proportional to the intensity of the x-ray beam, for a specific angle at a specific energy. The energy is usually chosen to be 100 eV above the edge energy (see Chap. 2). We refer to this as the percentage detuned at the specified energy. A slight complication to the detuning process occurs because the height of the x-rays reflected from the crystal in relation to the height of the optical table depends on the angle of the crystal. Since we use a very small pinhole, 500-300 μm in diameter, detuning often leads to a dramatic decrease in the intensity reading due to a change in height of the x-ray maximum with respect to the table. To detune properly table alignment and the detuning processes must be iterated.

Another common detuning problem can occur because the misalignment of the second crystal is fixed while the energy of the x-rays is incremented over a range of several hundred eV. This will cause the percentage detuned to either increase or decrease depending on the direction in which the second crystal is misaligned. This change does not cause a problem unless the monochromator becomes (almost) fully tuned. To identify this problem one checks the intensity spectrum for the I_0 ion chamber. A normal intensity spectrum will change slowly with energy where as this detuning problem will show a dramatic peak. One solution is to detune by a larger percentage so that the monochromator never becomes fully tuned. Another solution is to detune the crystal in the other direction so that the percentage detuned increases throughout the energy scan. I usually choose to misalign the crystal in the direction that corresponds to the least amount of detuning at the end of the energy scan where the XAFS signal is smallest.

3.1.2 Pinhole

A clever pinhole design was devised by Y. Yacoby. A schematic is shown in Fig. 3.4. It consists of a sheet of lead about 2 mm thick sandwiched in between an optical mount and a sheet of copper about 5 mm thick. The copper sheet has a small hole and a groove to mark the placement of a cylindrical tool that holds the needle used to make the pinhole. By adjusting the length of the set screw at the base of the tool the length the needle plunges into the lead can be changed determining the size of the pinhole. In practice this becomes an iterative process where we start with an undersized pinhole, check the size with a microscope and then shorten the length of

the set screw. Typical pinhole sizes are from 300 to 500 μm in diameter depending on the size of the sample. Generally the pinhole diameter is chosen to be 100 μm smaller than the sample diameter. This is to insure that the all the x-rays pass through the sample and not the edge of the gasket. The pinhole assembly is then easily attached

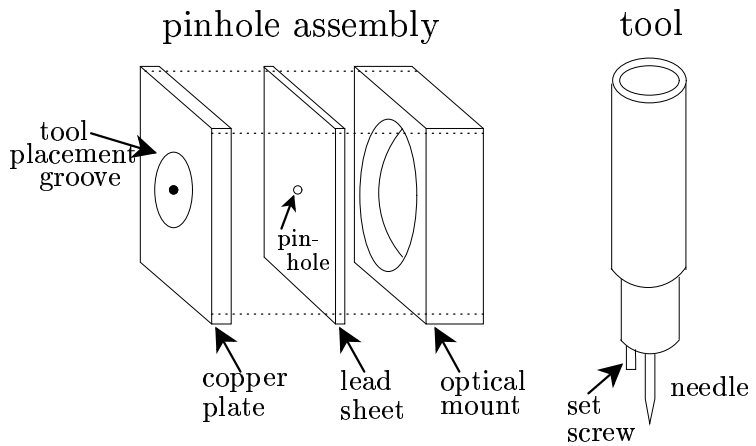

Figure 3.4: A schematic of the pin hole assembly and tool. A lead sheet is placed between an optical mount and a copper plate. The copper plate has a small hole and a groove to mark the placement of a cylindrical tool that holds the needle used to make the pinhole. The length of the set screw at the base of the tool determines the pinhole size which typically ranges from 300 to 500 μm.

to four optical motors which give it two rotational and two linear degrees of freedom. These motors are then adjusted to optimize the x-ray flux through the pin hole.

3.1.3 Ion Chambers

The ion chambers consist of two parallel plates and a region in between that is filled with a gas. The chambers are aligned so that the x-rays travel through the gas and between the plates. A high voltage is applied across the plates so that they become parallel plate capacitors with a strong electric field in between and perpendicular to the plates. When the x-rays travel through the gas a fraction of them will ionize the gas molecules. The electrons and ions are then pulled to opposite plates of the capacitor by the electric field. When these ionized parts hit the plates they produce a current that we measure. The current is sent directly to a preamplifier which outputs a voltage that is sent to an amplifier and then a voltage to frequency converter that

outputs a digital form of the voltage. The digital voltage is directly proportional to the amount of ionization. These ion chambers are described in some detail in Refs. [34] and [35].

The digital voltage reading from the ion chamber is simply related to the actual number of x-rays absorbed and should be checked to determine the correct sampling time:

$$\text{Voltage} = \frac{\text{e-X-Ray Energy}}{\text{Effective Ionization Energy}} \cdot \text{Amplifier Gain} \cdot \frac{\text{Number of X-Rays}}{\text{Second}}. \tag{3.1}$$

Since the effective ionization energy is about 30 eV the number of x-rays per second becomes

$$\frac{\text{Number of X-Rays}}{\text{Second}} = \frac{2\text{x}10^{20} \cdot \text{Voltage}}{\text{Amplifier Gain} \cdot \text{X-Ray Energy(eV)}}. \tag{3.2}$$

As discussed in Sec. 3.3.1 we should have a voltage reading due to approximately 5×10^8 x-rays in the incident ion chamber for each measurement.

Several precautions should be taken to ensure an accurate ion chamber current. First, the appropriate gas or gas mixture needs to be decided and is discussed below. Second, the bias voltage applied to the plates which creates the electric field should be checked. It should be well into the saturation region for the response of the ions to the electric field, usually chosen to be about 500 Volts, which ensures that the ions do not recombine with each other. The third precaution is to keep the ion chambers clear of any other ions or polarizable molecules that could combine with the ionized gas molecules. The major source of this type of contamination is the oxygen molecules in air which attracts the electrons.

The appropriate gases in the ion chambers are determined by the optimum absorption coefficients. The usual choices consist of He, N_2, Ar and Kr and in general higher x-ray energies require heavier gases. As discussed in Sec. 3.3.1 the absorption coefficients need to be about 1/4 for the incident ion chamber, I_0, and about three for the transmitted ion chamber, I_t. The edge energies of the sample and pressure calibrant are used to determine the appropriate gases with the help of the McMaster tables[26] or an extremely useful version compiled by Matt Newville[36] which contains a graph for each ion chamber depicting the x-ray absorption coefficients for the available gases as a function of x-ray energy.

3.1.4 High Pressure Experiment

In the vast majority of high pressure experiments diamond anvils are used instead of sintered boron carbide, B_4C, anvils. Diamond anvils have several advantages based on their transparency and hardness. The alignment of the diamond tip to the surface of the gasket is made extremely accurate by producing Newton rings that vanish when the alignment is within a wavelength of light. This and the hardness of the diamonds makes the maximum attainable pressure very high at about 100 GPa. The pressure and pressure gradients are accurately determined using the optical properties of ruby fluorescence. The one short fall of the diamond anvil in an XAFS experiment is its crystal structure. In an XAFS experiment the energy of the x-rays is incrementally increased over a range of several hundred eV. This process will inevitably encounter energies that satisfy Bragg conditions for the crystal structure of the diamond. This causes the x-rays to be reflected out of the line of the x-ray beam leading to large dips in the transmitted x-ray intensity. As shown in Fig. 3.5 these Bragg glitches destroy the XAFS signal. Remember, $\mu(E)\cdot x = \ln(I_0/I_t)$ so these dips appear as peaks in the figure.

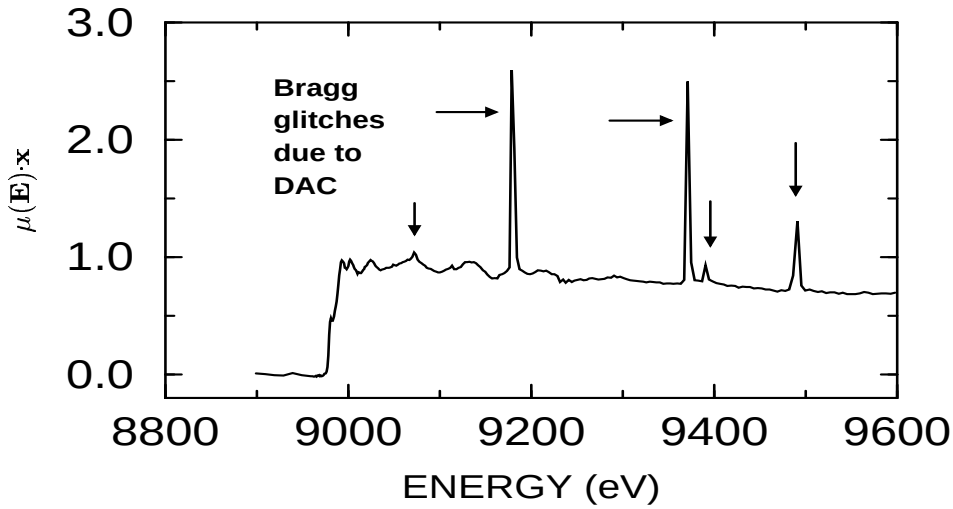

Figure 3.5: XAFS data of copper in a diamond anvil cell, DAC. The large peaks are a result of the x-ray energy satisfying a Bragg condition for the crystal structure of the diamond. The x-rays are then deflected from the transmitted ion chamber.

We use sintered B_4C anvils because they are polycrystalline, thereby yielding no Bragg glitches. The alignment is based on precision machining of the pressure cell bore and the pistons[37], (see Fig. 3.6). This type of cell allows for a maximum pressure of about 20 GPa. We determine the pressure by taking XAFS data of a cubic material for which we can accurately determine the amount of compression. The compression is then related to the pressure by a compressibility table. We have found that this method produces an uncertainty of about $\pm$ 0.5 GPa, the largest source of error being in the compressibility tables. Another disadvantage of using B_4C anvils is that pressure gradients cannot be measured directly.

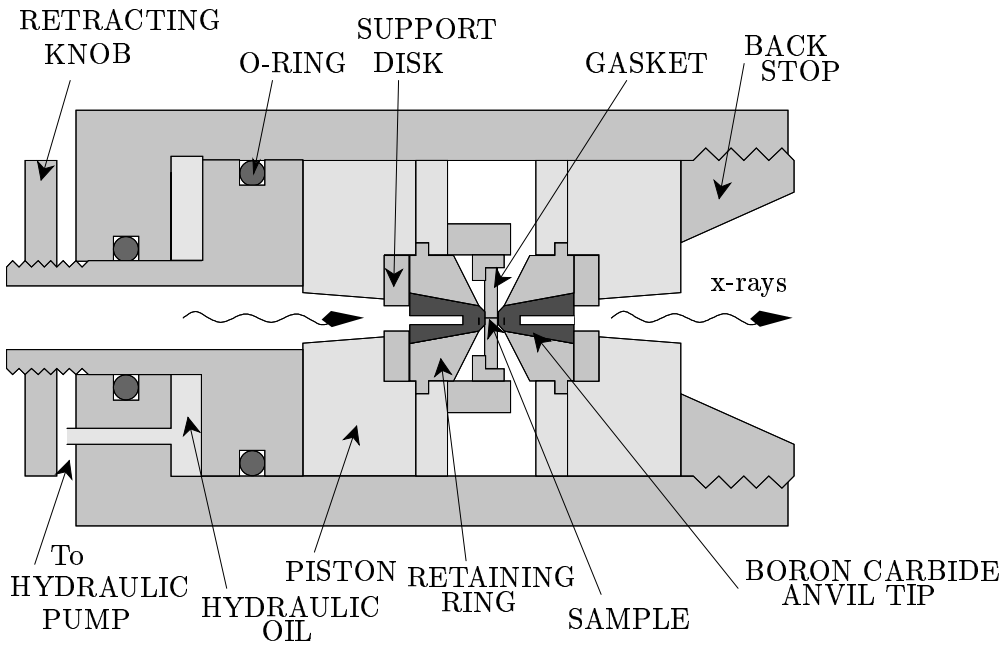

Figure 3.6: A schematic of the high pressure XAFS cell[37]

Sintered B_4C Anvils

Since the x-rays pass through the boron carbide (B_4C) anvils, their absorption coefficients contribute to the XAFS signal and must be considered when determining the optimum sample thickness as discussed in Sec. 3.2.2. Here we will derive a simple equation to calculate their absorption at any energy. The energy dependent absorp-

tion coefficient of the B_4C anvils is given by

$$\mu(\mathrm{E})\cdot\mathrm{x} = (\rho_B\sigma(E)_B + \rho_C\sigma(E)_C)x \tag{3.3}$$

where ρ_B and ρ_C are the partial densities of boron and carbon respectively, σ_B and σ_C are the energy dependent absorption cross sections and x is the thickness of the anvils. Given that the partial densities of B_4C are 1.97 gr/cm^3 for boron and 0.55 gr/cm^3 for carbon and that the total thickness of two anvils is about 0.4 cm, Eq. (3.3) reduces to

$$\mu(\mathrm{E})\cdot\mathrm{x} = 0.79\cdot\sigma(E)_B + 0.22\cdot\sigma(E)_C \tag{3.4}$$

where σ_C and σ_B are measured in cm^2/gr. Fig. 3.7 shows the energy dependent absorption coefficient for two B_4C anvils. The maximum total absorption $\mu(\mathrm{E})\cdot\mathrm{x}$ for the anvils and sample is about 2.5 therefore the energy that corresponds to an absorption coefficient of about 2 just for the anvils is about 8 keV. This sets a low energy limit on high pressure experiments corresponding to the k-edge energy of nickel which is the lightest element that we can look at under very high pressures. One obvious solution is to make the anvils thinner with the trade off of a lower maximum pressure.

Gaskets

The gaskets are made from the inconel 600 series which is a soft nickel alloy. The pieces of inconel are rolled to the proper thickness and then punched out in disks with a 10 mm diameter. Sample holes are then drilled in the center. Finally the inconel is heat treated to relieve stresses caused by the rolling and drilling processes.

The gaskets' sample hole size and thickness is determined by the pressure range of the experiment and are listed in Table 3.2. In general the diameter of the sample hole should be $\frac{1}{3}$ the diameter of the anvil tips. For a full treatment of the gasket in a high pressure cell see Ref. [38].

High Pressure Sample

For room temperature measurements, a hydrolic oil pump is used to generate a high pressure sample. As shown in Fig. 3.1 the hydrolic pump pushes oil into a chamber

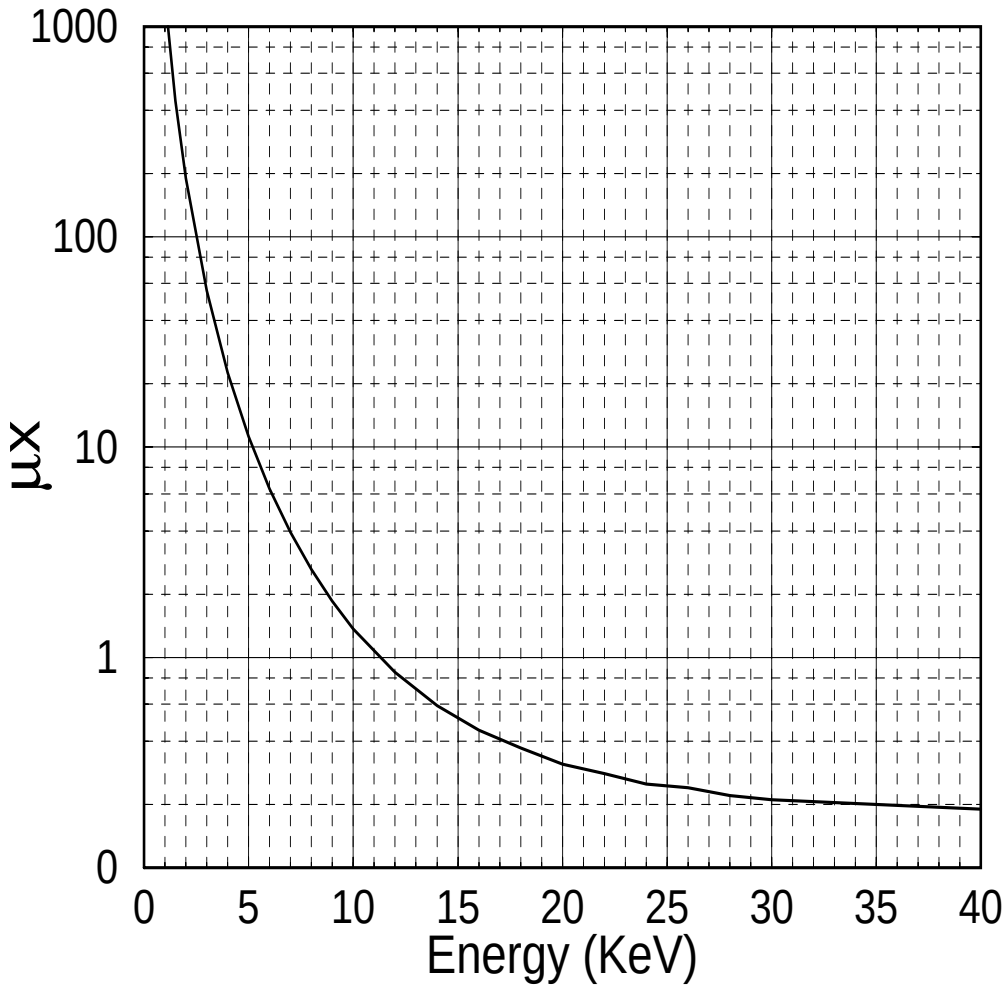

Figure 3.7: The energy dependence of the x-ray absorption coefficient for two 2 mm thick B_4C anvils.

Table 3.2: The appropriate gasket thickness, sample hole diameter and anvil tips diameter for the pressure range of the experiment.

Pressure range (GPa)	Anvil tip diameter (mm)	Sample hole diameter (mm)	Gasket thickness (μm)
0 to 2	2.5	0.8	500
0 to 8	2.0	0.8 to 0.5	400 to 250
5 to 20	1.5 to 1.4	0.5 to 0.4	250 to 200

which advances the piston. The piston is attached to a BC_4 anvil which is in direct contact with the gasket containing the sample. This system will relax, therefor a minimum of 15 minutes should be allowed between raising the pressure and taking the data.

It is advised to take reference data, of both the sample and the pressure calibrant, before the gasket and sample is loaded in the pressure cell. This is important because the pressure can be raised simply by tightening the pistons in the loading process, without the data outside the pressure cell you do not have a known reference point. For low temperature measurements, high pressure helium gas is used to generate a high pressure sample. The design is based on Ref. [39] and uses a inflatable diaphragm to advance the piston. A cold finger is used to cool the entire pressure cell. The basic design is shown in Ref. [40]. This design has the draw back that ice was allowed to form in the path of the x-rays. This changes the total absorption leading to strange background functions. I re-designed the apparatus as shown in Fig. 3.8 replacing the Styrofoam insulation with a vacuum to eliminate this problem. My design was also flawed in that the system cooled to 150 K, instead of to liquid nitrogen temperature (77 K) but this temperature was sufficient for my AgCl and AgBr data.

3.2 Sample Preparation

This section is broken up into two parts: the choice of pressure calibrant and the sample preparation. The high pressure calibrant is also a sample that needs to be prepared in much the same way as the sample of interest therefore this discussion is

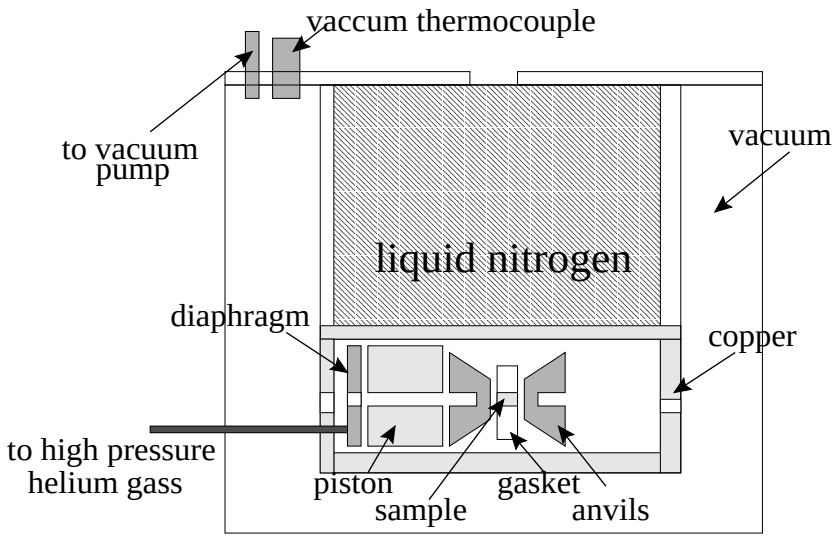

Figure 3.8: A diagram of the low temperature apparatus.

left to the second section on sample preparation.

3.2.1 Choice of Pressure Calibrant

The choice of material used as the pressure calibrant depends on several factors. The analysis process and the availability of equation of state data are among the most important considerations. The approximations used in theoretical calculations of the XAFS parameters are best suited for monoatomic materials[28]. Equation of state data for simple metals are easily found so we usually choose between copper, niobium and silver as our calibrants which are cubic so that they compress uniformly. Other materials such as NaBr and RbCl have also been used but are difficult to analyze given their ionic bonding, non-symmetric atomic potentials, and phase transitions at 5 and 17 GPa respectively. The edge energy is another important factor. The edge energy of the sample and calibrant should be close so that we minimize the time needed to move the monochromator. It is optimal for the edge energy of the calibrant to be much lower than that of the sample so that the absorption at the edge energy of interest will be dominated by the sample. Still another consideration in choosing a calibrant is its stability. To verify that no pressure induced chemical reactions have

occurred it is essential to compare the XAFS data of the sample and calibrant before and after the release of pressure.

3.2.2 Samples

The most important characteristics of an XAFS sample are its thickness, homogeneity and purity. For all of our experiments the sample consists of not only the substance which we want to study but also the pressure medium (carbon grease) and a pressure calibrant, usually chosen to be Nb, Ag or Cu powder. The calibrant is then mixed with the grease in the proper weight ratios. If the sample is also a powder as for RbCl then it is also mixed with the calibrant and grease. If the sample is a pellet as for AgCl and AgBr then the pellet is sandwiched in between the calibrant and grease mixture. The final combination is placed in the gasket as illustrated in Fig. 3.6. At each pressure XAFS data is collected for the calibrant and the sample both of which are together in the pressure cell.

Sample Purity

Most of the samples used in this thesis came from the Alpha Co and are at least 99.99% pure. Some specific precautions needed to be taken with just about every sample used in this thesis. RbCl is hygroscopic so this sample was heated to about 400K for about one hour to remove any water and then it was stored in a desiccator until it was used. The calibrants, copper or niobium powders, can oxidize so it is important to keep them packed in an air tight container filled with an inert gas. AgCl and AgBr are light sensitive so they were stored in a special foil used for this purpose.

Sample Homogeneity

The homogeneity of the sample is important because the XAFS signal will be attenuated if part of the x-rays do not pass through the sample as discussed in Sec. 3.3.2. Uniform powder samples are achieved by requiring the particle size to be less than the thickness of the sample and then mixing the powder very well with the pressure medium. For thin foils and soft materials the sample is squeezed to the appropriate thickness and then cut to fit in the sample hole of the gasket. For these types of samples it is important that the pinhole which defines the x-ray beam is considerably

smaller than the gasket sample hole so that all the x-rays pass through the sample.

Sample Thickness

The sample thickness is determined by optimizing the signal to noise ratio. As discussed in Sec. 3.3.1 this corresponds to an edge step absorption coefficient of about 1.0 while the total absorption coefficient does not exceed 2.55. The edge step absorption coefficient is defined as the change in the absorption coefficient evaluated at 50 eV below and 50 eV above the edge energy. The total absorption coefficient is evaluated at 50 eV above the edge energy. For our pressure experiments these absorption coefficients include not only the sample of interest but also a pressure calibration sample, the pressure medium and the anvils. Table 3.3 lists the appropriate absorption coefficients and their corresponding thicknesses for the AgBr experiment.

Table 3.3: The absorptions coefficients for the AgBr experiment. Nb was used as the pressure calibrant and carbon grease was used as the pressure medium. The initial thickness of the gasket was 250 μm which equals the thickness of the AgBr and Nb samples plus the grease. The thicknesses were determined so that the total absorption coefficient, μ(E)·x, was about 2.5 while the edge step absorption coefficient, $\Delta\mu$(E)·x, was about one for both the Ag and Nb k-edges.

		Ag k-edge		Nb k-edge	
	x (μm)	μ(E)·x	$\Delta\mu$(E)·x	μ(E)·x	$\Delta\mu$(E)·x
AgBr	63	1.64	1.00	1.43	0.21
Nb	10	0.34	0.04	0.71	0.59
grease	177	0.01	-	0.01	-
anvils	4000	0.23	0.01	0.35	0.03
total		2.22	1.05	2.50	0.83

3.3 XAFS Measurements

The most important decisions in an XAFS measurement are the appropriate absorption coefficients for ion chambers and sample and the appropriate time needed to accurately determine the incident and transmitted x-ray intensities. These quantities can be determined to maximize the signal to noise ratio. Here we consider noise

due to the statistical fluctuations in sampling a finite number of x-rays. For a more general and complete derivation of the signal to noise ratio see Ref. [41].

3.3.1 Signal to Noise

The noise in the XAFS signal due to statistical fluctuations is defined as the standard error in the absorption coefficient of the sample, $\mu_s \cdot x_s$, which we will denote as

$$N \equiv \delta(\mu_s \cdot x_s). \tag{3.5}$$

The absorption coefficient for the sample, $\mu_s \cdot x_s$, is the natural logarithm of the ratio of the transmitted to incident x-ray intensities and is written as

$$\mu_s \cdot x_s = \ln \frac{I_t}{I_0} \tag{3.6}$$

where I_0 and I_t are the quantities we measure. Using the rule for the propagation of error[31] we find that the error in $\mu_s \cdot x_s$ can be expressed as

$$\delta(\mu_s \cdot x_s)^2 = \left(\frac{\delta(\mu_s \cdot x_s)}{\delta I_0}\right)^2 \delta {I_0}^2 + \left(\frac{\delta(\mu_s \cdot x_s)}{\delta I_t}\right)^2 \delta {I_t}^2. \tag{3.7}$$

From Eq. 3.6 we substitute the partial derivatives of $\mu_s \cdot x_s$ with respect to I_0 and I_t in the previous expression which becomes

$$\delta(\mu_s \cdot x_s)^2 = \left(\frac{1}{I_0}\right)^2 \delta {I_0}^2 + \left(\frac{1}{I_t}\right)^2 \delta {I_t}^2. \tag{3.8}$$

Since δI_i is the standard error in the number of x-rays measured, $\delta I_i = \sqrt{I_i}$, the noise in the XAFS signal is simply the square root of the reciprocal sums of the incident and transmitted intensities,

$$N \equiv \delta(\mu_s \cdot x_s) = \sqrt{\frac{1}{I_0} + \frac{1}{I_t}}. \tag{3.9}$$

Now I can write the signal to noise ratio as

$$\frac{S}{N} = \frac{\alpha \Delta \mu_s \cdot x_s}{\sqrt{\frac{1}{I_0} + \frac{1}{I_t}}} \tag{3.10}$$

where the XAFS signal is simply a fraction α of the step height that contains the oscillations. The x-ray intensities in the signal to noise ratio can be related to the

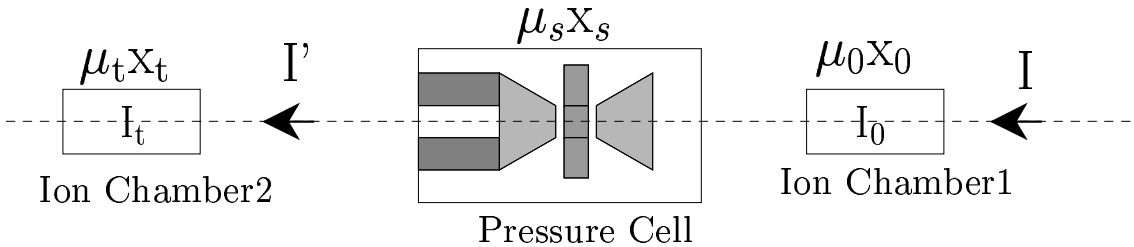

Figure 3.9: The intensity of x-rays attenuated by each ion chamber and sample. I have labeled the absorption coefficients and the lengths of the incident and transmitted ion chambers and the sample with the subscripts 0, t and s respectively.

geometry of the experiment. Fig. 3.9 shows the labels for the attenuation of the x-rays by each ion chamber and the sample. I have labeled the absorption coefficients and the lengths of the incident and transmitted ion chambers and the sample with the subscripts 0, t and s respectively. The x-rays absorbed in the first ion chamber can be written as

$$\mathrm{I}_0 = \mathrm{I} - \mathrm{I}e^{-\mu_0 x_0} \tag{3.11}$$

where I is the initial x-ray intensity. If the incident intensity for the second ion chamber is I′ then the x-rays absorbed in the second ion chamber can be written similarly as

$$\mathrm{I}_t = \mathrm{I}' - \mathrm{I}'e^{-\mu_t x_t}. \tag{3.12}$$

I′ is equal to the initial x-ray intensity attenuated by the first ion chamber and the sample,

$$\mathrm{I}' = \mathrm{I}e^{-\mu_0 x_0 - \mu_s x_s}. \tag{3.13}$$

Using these expressions for the x-ray intensities the signal to noise ratio of Eq. 3.10 becomes

$$\frac{\mathrm{S}}{\mathrm{N}} = \sqrt{I}\alpha\Delta\mu_{\mathrm{s}}\cdot\mathrm{x_s}\left(\frac{1}{1-\mathrm{e}^{-\mu_0\mathrm{x}_0}} + \frac{\mathrm{e}^{\mu_{\mathrm{s}}\mathrm{x}_{\mathrm{s}}+\mu_0\mathrm{x}_0}}{1-\mathrm{e}^{-\mu_t\mathrm{x}_t}}\right)^{-\frac{1}{2}}. \tag{3.14}$$

The optimum values for the absorption coefficients can be found by setting their partial deviates to zero. The nontrivial solutions are $\mu_0\cdot\mathrm{x}_0 = 0.22$ and $\mu_{\mathrm{s}}\cdot\mathrm{x}_{\mathrm{s}} = 2.55$ with infinite absorption coefficient for the 2nd ion chamber. In practice the 2nd ion chamber is set to absorb no more than 95% of the incoming x-rays which corresponds to $\mu_t\cdot\mathrm{x}_t = 3.0$ so that the entire length of the ion chamber is used.

Another important decision in any XAFS experiment is the amount of time needed to accurately determine the x-ray intensities. This corresponds to the amount of x-ray flux needed to give a reasonable signal to noise ratio. The signal to noise relationship in Eq. 3.14 goes like the square root of the initial x-ray intensity. Using the optimum values for the absorption coefficients of the ion chambers and sample Eq. 3.14 can be solved for the initial x-ray intensity and becomes

$$\mathrm{I} = 3.2\left(\frac{\mathrm{S}}{\mathrm{N}}\right)^2\left(\frac{\mu_{\mathrm{s}}\cdot\mathrm{x_s}}{\alpha\Delta\mu_{\mathrm{s}}\cdot\mathrm{x_s}}\right)^2. \tag{3.15}$$

Usually the fraction of the step height that contains the XAFS signal is about .01 for a step height of one and a reasonable signal to noise ratio is about 100 to 1 so the number of x-rays needed for each measurement is roughly 2 x 10^9. Since I sample about 22% of these x-rays in the $\mathrm{I_0}$ ion chamber I need to have a signal in the first ion chamber due to approximately 5 x 10^8 x-rays for each measurement of $\mathrm{I_0}$ and $\mathrm{I_t}$.

3.3.2 Errors in XAFS Measurements

Besides the random error discussed in Sec. 3.3.1, systematic errors can occur. The most common source of systematic errors in an XAFS measurement is due to thickness effects. Thickness effects refers to a group of problems that results in some fraction of the x-rays that are not uniformly absorbed. The name thickness effects comes from the most common source of this error a non-uniform sample thickness. This can occur with a powder sample if the sample is not well mixed with the pressure medium or if the grain size is large compared to the sample thickness[42]. Other sources of this same problem can be poor alignment of the sample and the x-rays or x-rays with

higher harmonic energies. If the sample is poorly aligned then some of the x-rays will not be attenuated by the sample which results in more absorption in the I_t ion chamber. Therefore $\mu(E)\cdot x$ will be smaller because we divide by a signal which is too large, $\mu(E)\cdot x = \ln(I_0/I_t)$.

Similarly, if the harmonic content of the beam is large then the I_0 ion chamber will not absorb many of these x-rays because it is much too thin whereas the I_t ion chamber will absorb them since it is still considered thick. For example, for x-rays with an energy of 7 keV we can set the absorption coefficients so that 20% of the x-rays are absorbed by the first ion chamber (I_0), while the sample absorbs 93% and the last ion chamber (I_t) absorbs 95%. In this case the percent of the x-rays absorbed by each component for the third harmonic, with an energy of 21 keV, will drop to 8%, 14% and 15% for I_0, the sample and I_t respectively. If we further assume that for each 1000 x-rays 20% have an energy corresponding to the third harmonic, then the ratio of the number of x-rays absorbed in I_0 to the number absorbed in I_t will be 160:43 for the fundamental energy (7keV) and 16:24 for the third harmonic. Since our detectors do not know the energy of the x-rays being absorbed, our signal with 20% third harmonics goes like 176:67 whereas a pure source without any harmonics would go like 200:53. Since the quantity that we are actually interested in is $\mu(E)\cdot x = \ln(I_0/I_t)$ the total number of photons does not matter but only their ratio. If we scale the ratio for the signal with harmonics so that the same number of photons are absorbed in I_0 for both cases the harmonic ratio goes from 176:67 $\rightarrow$ 200:76. Now compare the two ratios. The ratio of the number of x-rays absorbed in I_0:I_t in the case where there is zero harmonics is 200:53 and in the case where there is 20% harmonics is 200:76 so we find that it is the division by a number that is about 43% too big that diminishes our XAFS signal.

All errors that belong to the class of "thickness effects" result in a diminished XAFS signal which leads to inaccurate amplitude factors in the XAFS equation[43].

Chapter 4

NIOBIUM PRESSURE CALIBRANT

I collected the XAFS data for Nb and AgCl together according to the procedure described in Chap. 3. The main goal for the analysis of the Nb data is to determine it's compression. This compression is related to pressure through previously measured values for the change in volume of Nb with pressure. The resulting pressure is used as a known extrinsic parameter in the data analysis of AgCl presented in Chapter 6. Hence, the Nb-data is used as a pressure calibrant for the AgCl-data.

In Sec. 3.2.1 I discussed the choice of a pressure calibrant. As discussed the usual choices are Cu, Nb, and Ag. Obviously, a Ag calibrant cannot be used with a AgCl sample. One criteria for the pressure calibrant is that both the calibrant and sample edges can be reached with the same monochromator crystal (see Sec. 3.1.1). The Nb calibrant has a k-edge energy at 19 keV which is closest to the Ag k-edge at 25.5 keV and can be reached with a (400)-monochromator crystal whereas the Cu edge energy is too low at 9 keV, therefore Nb is our choice.

Sec. 3.2.2 describes the preparation of the Nb powder which I mixed with carbon grease and placed in the gasket along with the AgCl pellet. In Sec. 3.1.4 I describe the low temperature apparatus and its use of high pressure nitrogen gas to apply pressure to the sample. Liquid nitrogen is used to cool the sample to 150K. I collected the data at the Nb k-edge and at the Ag k-edge at 0, 1500, 1900, 2100, 2300, 2400, 2500, 2700, 2900 and 3100 PSI (pounds per square inch) for the nitrogen gas.

Here I will discuss the determination of pressure from the XAFS determined fractional change in the first nearest neighbor distance. Tabulated values for the fractional change in volume for Nb at several pressures can be found in Ref. [44]. From each datum listed in the table, I calculate the fractional change in the first nearest neighbor distance. I show the results, represented by the diamonds, in Fig. 4.1. I have smoothed the relationship by performing least squares fit which I also show in the figure represented by the solid curve. The uncertainty in this fit, represented by the dashed curves in the figure, is caused by the spread in the data points as no uncertainty in the individual datum were reported. As a result these dashed curves

represent a minimum uncertainty. Once I determine the change in the first nearest neighbor distance from the XAFS data, I will use the solid curve in this figure to convert the fractional change in the first nearest neighbor distance to pressure. For the error estimation in the pressure I will account for all uncertainties including the error in this curve and the error in my determination of the fractional change in first nearest neighbor distance.

The data shown in Fig. 4.1 was determined at room temperature. Using these results to determine the pressure at 150 K, neglects the temperature dependence of the compressibility. This results in an under-prediction of the actual pressure. I will estimate this error in the Sec. 4.3.

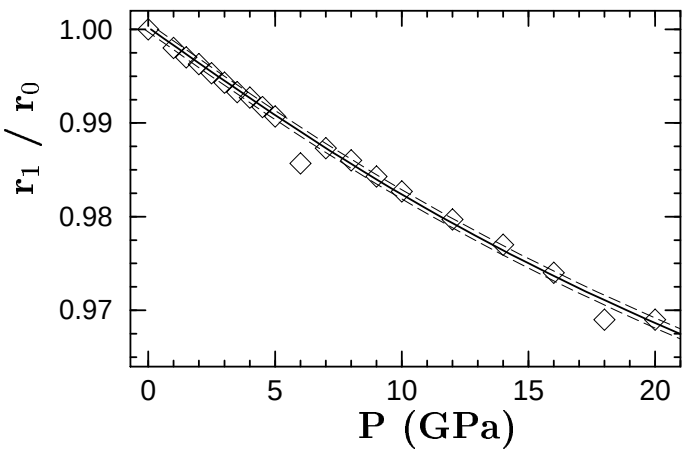

Figure 4.1: The pressure dependence of the fractional change in the first nearest neighbor distance for Nb. The diamonds represent the experimental results converted from bulk volume measurements which can be found in Ref. [44]. The line represents the fit to these experimental data and the error in the line is shown by the dashed lines which is about ± 0.5 GPa.

The following is an outline of the analysis procedure:

- Compare the crystal structure of Nb to $|\tilde{\chi}(R)|$-data in order to decide how many paths to include in the theoretical model.
- Compare the $|\tilde{\chi}(R)|$-data taken at different pressures and explain the expected changes that occur as the pressure is increased.
- Describe the alignment and background removal procedure for the data.
- Describe the parameters varied in the fit of the theoretical model to the data.

- Determine the pressure independent parameters and then the pressure dependent parameters.
- Convert the fractional change in the first nearest neighbor distance to pressure as described above.
- Discuss the pressure dependence of the Debye temperature.

4.1 Crystal Structure of Nb

The crystal structure for Nb is body centered cubic (bcc)[45]. At ambient pressure and room temperature the lattice constant a is 3.3004 Å[45]. The expected lattice constant at 150K, the temperature of my measurements, is $a = 3.2973$ Å. I determined this value using the fractional expansion $\epsilon = -940 \times 10^{-6}$ at 150K from Ref. [44] where $\epsilon = (a_{150} - a_{293})/a_{293}$, a_{150} is the lattice constant at 150K, and a_{293} is the lattice constant at room temperature.

I will use parameter ϵ_{p} throughout this thesis to characterize the pressure dependence of the distances determined from my measurements. I have added the subscript p to distinguish it from the temperature dependent value. In this context, I will drop the negative sign and refer to it as a fractional compression.

4.1.1 Fourier Transform as a Finger-Print

The magnitude of the Fourier transform of the $\chi(k)$ can be considered a finger-print for a particular local structure. I described the Fourier transform procedure of XAFS data in Sec. 2.2.2. From the XAFS Eq. 2.10 the position of the peaks in $|\tilde{\chi}(R)|$-data are related to the half-path length. Here only single scattering paths are considered, so that this distance is equivalent to the bond length between the atoms. The XAFS equation also prescribes that the peak height is related to the number of atoms with the same bond length and the relative mean square deviation in the bond length, σ_i^2. Examples of $|\tilde{\chi}(R)|$ for Nb at several pressures are shown in Fig. 4.2. I have labeled the peaks from the first three coordination shells. These data were obtained using the Fourier transform parameters and data ranges listed in Table 4.1.

If the central atom is placed at the center of the bcc unit cell, the atoms which contribute to the the first three shells are located at: (a) the corners of the unit cell, (b) the center of each of the 6 surrounding unit cells, and (c) the 4 far corners of each of the six surrounding unit cells. The distances to each of these shells are given, in terms of the unit cell dimension a, by $\mathrm{r}_1 = \sqrt{3}a/2$, $\mathrm{r}_2 = a$ and $r_3 = \sqrt{11}a/2$. Using

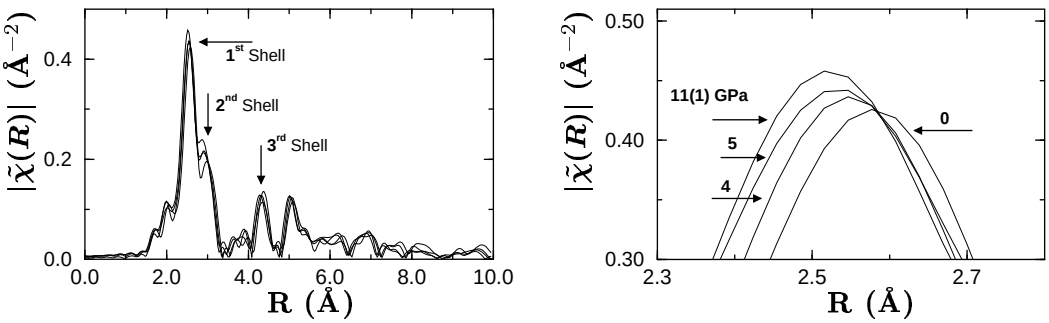

Figure 4.2: $|\tilde{\chi}(R)|$ at 0, 4, 5, 11 $\pm$ 1 GPa for Nb. Left panel: I show the full R-range and I have labeled the peaks due to the first three shells of atoms. That there are no significant changes in $|\tilde{\chi}(R)|$ implies that Nb does not undergo any phase transitions in this pressure range. Right panel: An enlargement of the tip of the 1st shell peak. As the pressure is increased the amplitude of the 1st shell peak increases and the peak moves to lower R.

Table 4.1: Fourier transform parameters along with fit and data ranges for Nb. A detail description of these parameters can be found in Sec. 2.2.2. The fit range is listed in R-space. The data range is listed in k-space. The Fourier transform parameters including the k-weighting, the window type and the sill widths dk are listed.

R-range (Å)	k-range (Å^{-1})	Window type	dk(Å^{-1})	k-weighting
[1.9:3.4]	[2.9:15]	Hanning	2.0	1

the previously determined a for ambient pressure and 150K, I find that $r_1 = 2.8555$ Å, $r_2 = 3.2973$ Å and $r_3 = 5.4679$ Å. From these distances the first and second shells are separated by only 0.4 Å whereas the second and third shells are separated by 2.1 Å. As shown in the $|\tilde{\chi}(R)|$ data (Fig. 4.2) the peaks caused by the first and second shells overlap because of their small radial separation whereas the peak caused by the third shell is well separated from the first two. Since the first and second shells overlap in R-space both are included in the theoretical model. The contribution from the third and higher shells do not overlap in R-space so they can be left out of the fit without loss of accuracy.

4.1.2 Pressure Dependence of $|\tilde{\chi}(R)|$

I have included in Fig. 4.2 data sets at ambient pressure and at the maximum pressure as well as at two intermediate pressures. Since the gross features, including the peak positions and heights, are about the same for each data set I conclude that no structural change has occurred and all data sets represent the bcc structure. The right panel of Fig. 4.2 shows only the top of the first peak. In this panel it is evident that the peak position moves to lower R values and that the peak height *slightly* increases as the pressure is increased. These trends are expected and have a physical interpretation. The increase in pressure compresses the Nb resulting in shorter bond lengths therefore the peak positions move to lower R values. The increased pressure results in steeper atomic potentials which corresponds to a decrease in the relative mean-square displacements between the atom pairs, the σ^2 term in Eq. 2.10, resulting in an increase in the peak height. As you can see from the data the increase in the peak height is just *slightly* outside the noise level in the data. This noise level can be estimated by comparing the variation in amplitude of the $|\tilde{\chi}(R)|$ at large R shown in the left panel.

4.2 Alignment and Background Removal

A detailed discussion of the alignment and background removal procedure can be found in Sec. 2.2.1. Here I will state the important parameters used in this procedure and show an example of the results. As outlined in Sec. 2.2.1, the value for the Fermi energy, E_0, is set to 45% of the step height at 18983 $\pm$ 1 eV in the normalized and aligned data and R_{bkg} parameter is set to 1.8 Å. Given these parameters, AUTOBK

finds the resulting spline of 19 knots, as indicated by Eq. 2.31, which it subtracts from the data to isolate the XAFS signal. An example of the μ(E)·x-data and -background for Nb at ambient pressure is shown in Fig. 4.3.

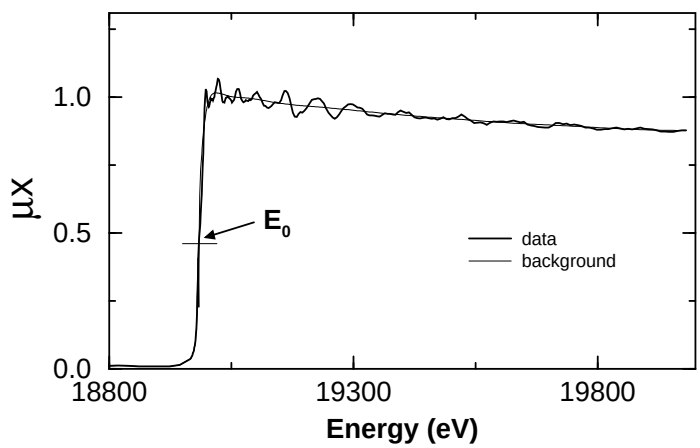

Figure 4.3: μ(E)·x-data and background function for Nb at ambient pressure and 150K. E_0, the Fermi energy, is labeled and was set to correspond to 45% of the step height.

At each sampled pressure at least two complete sets of data are collected. After they are aligned and the background is removed, the resulting $\chi(k)$ data for the same pressure are averaged to reduce shot-noise. An example is shown in Fig. 4.4.

4.3 XAFS Parameters and Meaningful Parameters

As we discussed in Sec. 4.1.1 the first two shells are included in the theoretical model. Many of the XAFS parameters for these two shells are related in a fundamental way. A detailed discussion of all possible XAFS parameters can be found in Sec. 2.2.4. The basic parameters needed for these fits are S_0^2, $\Delta E_0{}^i$, σ_i^2 and Δr_i. In this picture there are a total of 7 parameters. They are S_0^2, $\Delta E_0{}^1$, $\Delta E_0{}^2$, σ_1^2, σ_2^2, Δr_1 and Δr_2 where the script 1 and 2 refers to the parameters for first and second shells respectively.

Several of these parameters can be physically related reducing the number of fit parameters. The first physical relation is caused by the uniform compression of the Nb sample. Since Nb has cubic symmetry, each bond length is expected to compresses by the same factor therefore $\Delta r_i = -\epsilon_p \cdot r_{ref_i}$ where r_{ref_i} is the initial reference bond

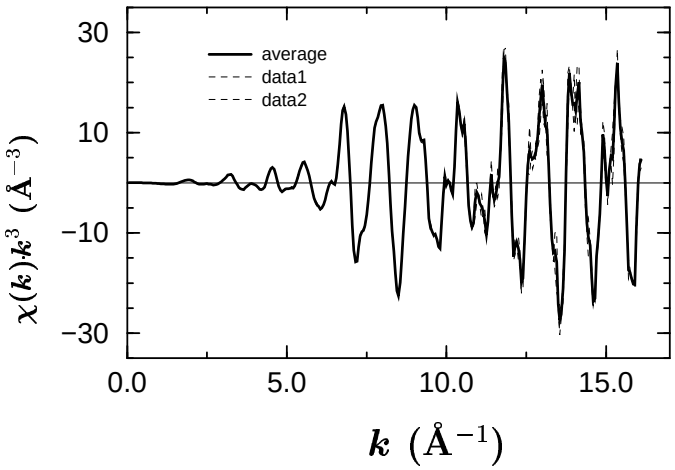

Figure 4.4: Averaged $\chi(k)\cdot k^3$ data are shown with the thick line. The individual contributions are shown with dashed lines. These data are weighted with k^3 to emphasize the high k region where the differences are largest just so we can see the differences.

length and ϵ_{p} is the fractional compression and is defined as:

$$\epsilon_{\mathrm{p}} = \frac{\mathrm{r}_{\mathrm{ref}_i} - \mathrm{r}_i}{\mathrm{r}_{\mathrm{ref}_i}}. \tag{4.1}$$

In this way, the best-fit value for a single parameter ϵ_{p} determines both bond lengths. The second physical relation is for the relative mean-square displacements between the atoms pairs; this is a relationship between the values for σ_1^2 and σ_2^2. The relationship is made through the Einstein or Debye model. Both of these models are included in FEFFIT. Theses models depend on the reduced mass of the atoms, their separation, the temperature and a Debye or Einstein temperature. FEFFIT is given the first two parameters from FEFF and since the temperature is known there is only a Debye or Einstein temperature as a variable in the fit, denoted as θ_{Debye} or θ_{Eins} respectively. As long as the relative stiffness of the bond between the atoms is about the same, one Debye or Einstein temperature can be used to determine each σ_i^2. This is expected to be true for Nb were all the atom are of the same type and is discussed in more detail in the following subsection. Through the use of these physical constraints the original 7 fitted parameters are reduced to 5. They are ϵ_{p}, θ_{Debye}, $\Delta\mathrm{E}_0{}^i$ and S_0^2.

As described in Sec. 2.2.4 when I consider each constraint, the reduced-chi squared

is compared with the constraint to the value without the constraint. In each case where I have chosen to use the constraint it does not decrease the quality of the fit. Seldom does the constraint actually improve the quality of the fit since I am restricting its freedom. The constraints are an important implication of real physical relationships that are often necessary to extract meaningful parameters.

Pressure and the Debye Model

For temperature studies, a single θ_{Debye} or θ_{Eins} is often used to predict the temperature dependence of σ^2 for a particular shell. In this case it is important to choose the model carefully. Numerous paper have been written explaining different systems in which either the Debye or Einstein models have worked best[46, 47].

The pressure dependence of σ_i^2 is not described in this way. For pressure measurements, the temperature is a constant and θ_{Debye} or θ_{Eins} changes for each pressure point. This change in θ_{Debye} or θ_{Eins} describes the change in the phonon cutoff frequency for the atom pairs as the pressure is increased. The Grüneisen relationship predicts that θ_{Debye} should increase linearly with the compression, ϵ_{p} which is defined in Eq. 4.1. The slope of this relationship is related to the Grüneisen parameter, γ, and is defined [32] as:

$$\frac{\theta_{\mathrm{Debye}_0} - \theta_{\mathrm{Debye}}}{\theta_{\mathrm{Debye}_0}} \equiv -3\gamma\epsilon_{\mathrm{p}}. \tag{4.2}$$

The Debye model is used here because the phonon frequencies scale linearly with θ_{Debye};

$$\mathrm{k_B}\theta_{\mathrm{Debye}} = \hbar\omega_{\mathrm{D}ebye}, \tag{4.3}$$

where $\mathrm{k_B}$ is Bolzmann's constant, $\hbar$ is Planck's constant and, $\omega_{\mathrm{D}ebye}$ is a measure of the maximum phonon frequency. Because of the Grüneisen relationship to the Debye model, I use it to predict the pressure dependence of σ_i^2.

In this way, the Debye model is used to characterize the stiffness of the bond between atom pairs. Therefore if the sample has more than one type of atom or if the bond length changes by more than 0.5 Å a different Debye temperature should be used to distinguish between the different types of bonding [48].

The Grüneisen parameter does depend on temperature. At temperatures larger

than θ_{Debye} the Grüneisen parameter reaches a different constant value than that found a temperatures much less than θ_{Debye}. Examples of the temperature dependence of Grüneisen parameter can be found in Ref. [32].

Often a different kind of Grüneisen parameter is reported from XAFS measurements which is defined in terms of σ^2 as

$$\frac{\sigma_0^2 - \sigma^2}{\sigma_0^2} \equiv -6\gamma\epsilon_{\mathrm{p}}. \tag{4.4}$$

This relationship holds as long as the temperature is much greater than θ_{Debye}. In this limit σ^2 is related to ω by

$$\sigma^2 = \frac{\mathrm{k_B{\cdot}T}}{\mathrm{M_r{\cdot}}\omega^2} \tag{4.5}$$

where $\mathrm{k_B}$ is Boltzmann constant, $\mathrm{M_r}$ is the reduced mass of the atom pairs and T is the temperature. For all temperatures the relationship is more complicated, written [13] as:

$$\sigma^2 = \frac{\hbar}{\mathrm{M_r{\cdot}}\omega}\left[\frac{1}{\exp\frac{\hbar\cdot\omega}{\mathrm{k_B{\cdot}T}} - 1} + 1\right] \tag{4.6}$$

The general relationship between σ^2 and the Grüneisen parameter becomes

$$\frac{\Delta\sigma^2}{\sigma^2} = -3\gamma\left[1 + \omega{\cdot}\frac{\hbar}{\mathrm{k_B{\cdot}T}}\left(\frac{1}{\exp\frac{\hbar\omega}{\mathrm{k_B{\cdot}T}} - 1}\right)\right]\epsilon_{\mathrm{p}}. \tag{4.7}$$

For example, the large term in parenthesis becomes 1.49 for a Ag→Br bond at 150 K with a $\theta_{\mathrm{Debye}} = 200$ K. To determine this value I calculate ω from Eq. 4.3. This illustrates that the ratio between $\frac{\Delta\sigma^2}{\sigma^2}$ and $\frac{\Delta\theta_{\mathrm{Debye}}{}^2}{\theta_{\mathrm{Debye}}{}^2}$ become more similar at lower temperatures as compared to the factor of 2 in Eq. 4.4 obtained in the high temperature limit.

Pressure and Compressibility

As I stated in the introduction, the data shown in Fig. 4.1 was determined from room temperature measurements. Using these data to determine the pressure at 150 K neglects the temperature dependence of the compressibility, χ which is defined as the

change in volume per change in pressure times one over the initial volume, written as

$$\chi \equiv \frac{1}{\mathrm{V}}\frac{\Delta \mathrm{V}}{\Delta \mathrm{P}}. \tag{4.8}$$

The compressibility can also be related to several thermodynamic quantities,

$$\chi = \frac{\alpha_{\mathrm{v}}\mathrm{V}}{\gamma \mathrm{C}_{\mathrm{v}}^{\mathrm{l}}}. \tag{4.9}$$

where α_{v} is 3 times thermal expansion coefficient, V is the volume per mol, γ is the Grüneisen parameter and, $\mathrm{C}_{\mathrm{v}}^{\mathrm{l}}$ is the lattice contribution to the specific heat. Table 4.2 lists these parameters for Nb at 298 K and 100K from which I calculate the fractional change in the compressibility $\chi_{300}/\chi_{100} = 1.02$. This indicates that using the compressibility measurements at room temperature to determine the pressure at 150K results in a 2% underprediction in the pressure, which as I will show in Sec. 4.6 is well within my 10% uncertainty in the determination of the pressure.

Table 4.2: Parameters used to calculate the compression of Nb.

Parameter	100 K	298 K	Reference
$\alpha_{\mathrm{v}}(10^{-6}/K)$	14.1	21.3	[44]
V (cm^3/mol)	10.78	10.82	[44]
$\mathrm{C}_{\mathrm{v}}^{\mathrm{l}}$ (J/mol K)	17.4	24.3	[49]
γ	1.49	1.58	[49]

4.4 Determination of S_0^2

An initial step in the analysis is to determine the value for S_0^2, the passive electron amplitude reduction factor. A detailed description of this parameter can be found in Sec. 2.1.2. As I discussed in Sec. 2.2.4, the amplitude terms S_0^2 and σ_i^2 are highly correlated. The k-weighting I use in the Fourier transform of $\chi(k)$ influences the values found for these amplitude terms since S_0^2 and σ_i^2 have different k dependencies: S_0^2 does not depend on k while the σ_i^2 is a decreasing exponential in k^2 (see Eq. 2.10). The change in the $|\tilde{\chi}(R)|$ is quite obvious therefore I show an example of $|\tilde{\chi}(R)|$ for

Nb at ambient pressure and 150K determined from the Fourier transform of $\chi(k)\cdot k^w$ with k-weightings, $w = 1, 2$ and 3 in Fig. 4.5. The Fourier transfrom procedure is discussed in Sec. 2.2.2. Because of the different k dependencies of the amplitude

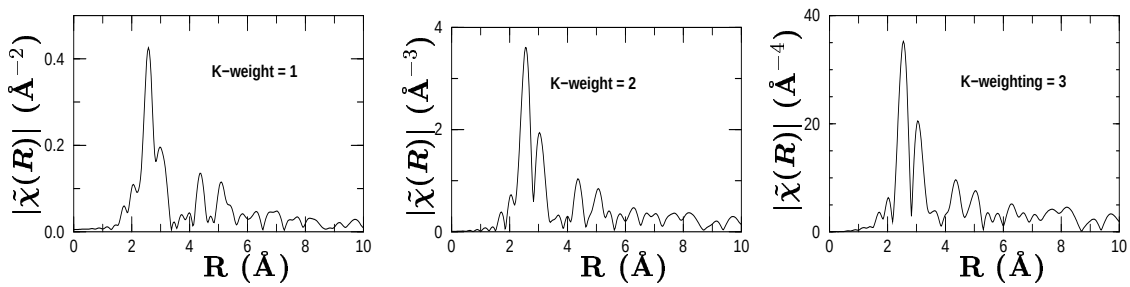

Figure 4.5: $|\tilde{\chi}(R)|$ data for Nb at ambient pressure and 150K. From left to right the k-weighting of the $\chi(k)\cdot k^w$ data is varied as $w = 1, 2$ and 3. The physical parameters should not depended on the k-weighting and therefore we often fit all three sets of data to the same theoretical model. This method is most useful in determining amplitude terms such as S_0^2 and σ^2 as shown in Fig. 4.6.

terms it can be used to break their correlation. To demonstrate this correlation, I set the value for S_0^2 to 0.7, 0.8, 0.9 and 1.0 and, set the value for the k-weighting, w, to 1, 2 and 3. Then I find the best-fit value for θ_{Debye} for each of these combinations of S_0^2 and w (σ^2 is determined through the Debye model). In this way I have 12 different fits to the data. I show the best-fit results for θ_{Debye} in Fig. 4.6 for each of these combinations. The lines connect the values found for each k-weighting. The point were the three lines intersect at approximately $\theta_{\text{Debye}} = 350$ and $S_0^2 = 0.77$ give the best-fit values independent of k-weighting. A simpler "short cut" is to simply include all three k-weightings in one fit and determine both S_0^2 and θ_{Debye}. This is what I will call a simultaneous fit with k-weightings of w= 1, 2 and 3. From this single fit I get a similar result: $\theta_{\text{Debye}} = 344 \pm 10$ and $S_0^2 = 0.76 \pm 0.03$. The "short cut" method gives results that are consistent with the long 12-fit method, therefore the "short cut" will be used throughout this thesis.

Another parameter that can be used to break the correlations between the amplitude terms is the pressure: S_0^2 has no pressure dependence while θ_{Debye} is expected to increase as the pressure is increased as I discussed in Sec. 4.3. Here the "long method" would be to repeat the process described above for the data at each pressure and then to average the resulting S_0^2-values. Another option is to simply use the "short cut" and simultaneously fit the theoretical models with one S_0^2 to each of the data sets

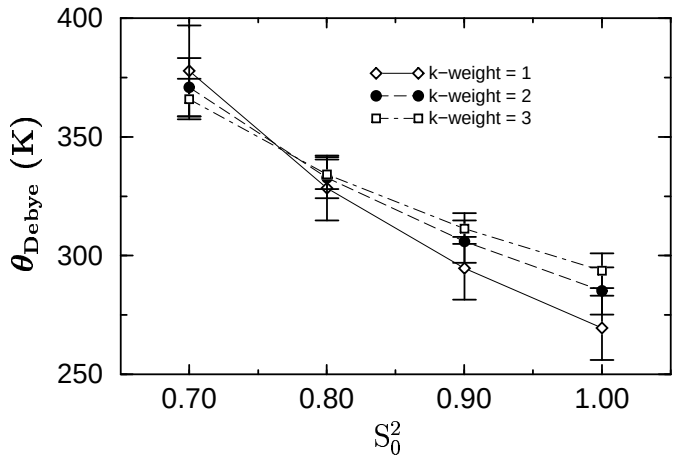

Figure 4.6: Example of using different k-weightings to break the correlation between the amplitude terms, S_0^2 and θ_{Debye}. Each point on the line represents the best-fit value for θ_{Debye} while the value for S_0^2 was set to 0.7, 0.8, 0.9 and 1.0. The solid, dashed and dot-dashed line connects the best-fit results for θ_{Debye} to data with a k-weight of w= 1, 2 and 3 respectively. The physical parameters should not depend on the k-weighting and therefore the best value for S_0^2 and θ_{Debye} is the point where all three lines intersect at approximately $\theta_{\mathrm{Debye}} = 350$ and $S_0^2 = 0.77$.

using a k-weighting of w= 1, 2 and 3. As shown explicit in the previous example both methods give results which are consistent therefore I only discuss the "short cut" method. For each data set the total number of pressure dependent parameters is three: ϵ_{p}, ΔE_0 and θ_{Debye}. I choose data from 5 different pressures giving a total of 15 pressure dependent fitted parameters plus the one S_0^2. The resulting best-fit value for $S_0^2 = 0.82 \pm 0.02$, similar to the value found at ambient pressure although slightly outside the uncertainty. Since this value for S_0^2 incorporates both the multiple k-weighings and the pressure dependence of the data it is the more reliable value.

The data ranges and Fourier transform parameters that I used here are listed in Table 4.1 except for the k-weighing as described above. Examples of the data and theoretical fits can be found in Sec. 4.6 where the pressure is determined.

4.5 Determination of ΔE_0

Next, I determine an average ${\Delta E_0}^i$. As I discussed in Sec. 2.2.4, it is highly correlated with the compression, ϵ_{p}. These phase terms have unique k-dependences so that each parameter can be determined independently. From the XAFS Eq. 2.10 the majority

of the Δr dependence comes from the exp(i2kΔr) term which is small for small k. An energy shift depends on the inverse of k, $\Delta E = 2E\Delta k/k$, which is small for large k. I have taken the partial derivative of Eq. 2.2 to obtain this relationship. Therefore energy shifts will dominate at low k while changes in the bond length will dominate at high k. So that the fit is most sensitive to changes in energy the low k-region of the data is emphasized. Therefore a k-weighting of one is used where the Fourier transform parameters and, data and fit ranges are as listed in Table 4.1. Here I fit the data at each pressure independently. The value for S_0^2 is fixed at 0.82 ± 0.02 as I determined in Sec. 4.4. Each of these fits contains four parameters: ϵ_p, $\Delta E_0{}^i$ and θ_{Debye} with 12 independent points as given by Eq. 2.40. The resulting average value for $\Delta E_0{}^1 = 1.52 \pm 0.7$ eV and $\Delta E_0{}^2 = 3.82 \pm 1.0$ eV. The largest deviation in the best-fit values for $\Delta E_0{}^i$ is about one eV.

The use of separate energy shifts for the first and second shells is surprising since Nb is a metal in which the models for neutral atomic potentials and screening of the core-hole should work well, requiring no additional energy shifts for the second shell. One indication that the core-hole is not completely screened is the relatively low value for $S_0^2 = 0.82 \pm 0.02$ compared to the value of one which represents a completely screened core-hole (see Sec. 2.1.2). This indicates that there is some charge transfere which is also indicated by the seperate energy shifts for the first and second shells. The average χ_ν^2 reduced by a factor of two or more by including the additional energy shift indicating that they are both needed.

4.6 Determination of Compression and Pressure

The final step determines the pressure dependent parameters: the fractional compression, ϵ_p, and the Debye temperature, θ_{Debye}. I show the data and the fitted model in R-space in Fig. 4.6 at ambient pressure. The vertical lines in this figure represent the fit range. These fit and data ranges specify 12 independent points per data set as determined by Eq. 2.40. Our Fourier transform parameters are listed in Table 4.1. I list the resulting best-fit values in Table 4.3 in terms of the change in the first nearest neighbor distance and θ_{Debye} along with the goodness-of-fit parameters. A description of the goodness-of-fit parameters can be found in Sec. 2.2.4. The pressure depence of ϵ_p and θ_{Debye} are discussed in the following subsections. For completeness I have listed the θ_{Debye} and the corresponding values for σ_i^2 as a function of pressure in Table 4.4.

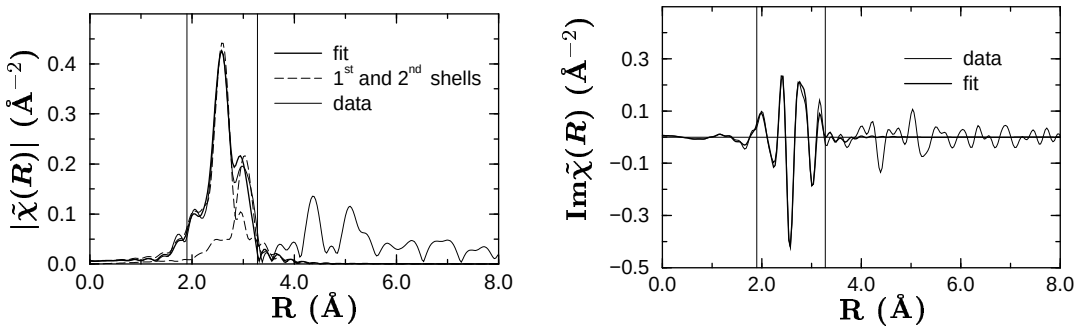

Figure 4.7: The left panel and right panels show the $|\tilde{\chi}(R)|$ and Im$\tilde{\chi}(R)$ for the data and the theoretical fit for Nb at ambient pressure and 150K. The individual contributions for each shell are shown in the left panel. The fit range is indicated by the vertical lines. The Fourier transform parameters are listed in Table 4.1.

Table 4.3: Fit results for Nb listed in terms of the first path parameters: the change in the half path length, Δr_1 and the mean-square displacement of the path, σ_1^2 along with the goodness-of-fit parameters: χ_ν^2 and R-factor. The reference value for the first nearest neighbor distance found at ambient pressure is 2.867 ± 0.004 Å.

PSI	Δr_1 (Å)	θ_{Debye} (K)	χ_ν^2	R-factor
0	0.000(2)	318(8)	25	0.2
1500	-0.012(1)	319(6)	3	0.2
1900	-0.022(1)	319(8)	24	0.4
2100	-0.027(1)	325(5)	7	0.1
2300	-0.026(1)	328(12)	522	0.7
2400	-0.036(2)	328(10)	400	0.6
2500	-0.038(2)	328(12)	233	0.2
2700	-0.037(2)	307(11)	264	0.9
2900	-0.048(2)	332(13)	459	0.7
3100	-0.052(2)	322(10)	341	0.3

Table 4.4: List of σ_i^2 and the corresponding θ_{Debye} for Nb.

Pressure (GPa)	θ_{Debye} (K)	σ_1^2 (Å^2)	σ_2^2 (Å^2)
0	321(13)	0.0033(5)	0.0037(5)
2.3	322(12)	0.0033(5)	0.0037(5)
4.2	324(12)	0.0033(5)	0.0037(5)
5.2	327(13)	0.0032(5)	0.0036(5)
4.9	325(15)	0.0031(5)	0.0035(5)
7.0	333(15)	0.0031(5)	0.0035(5)
7.3	310(12)	0.0034(5)	0.0038(5)
7.2	305(17)	0.0035(5)	0.0039(5)
9.4	311(16)	0.0034(5)	0.0038(5)
10.2	322(14)	0.0032(5)	0.0036(5)

Sample Pressure

Finally, I calculate r_1/r_0 and determined the pressure. Our best-fit value for r_0, the first nearest neighbor distance at ambient pressure, is 2.867 ± 0.004 Å which differs from the expected value of 2.856 Å, calculated using the room temperature value[45] using the coefficient of linear expansion[44] in Sec. 4.1.1. The difference, 0.011 Å, is outside of our uncertainty of 0.004 Å although an error of 0.011 Å for the absolute value of a distance is quite typical for XAFS measurements. This disagreement is not a serious problem since it is certain that our best-fit value for the first nearest neighbor distance corresponds to ambient pressure and 150K therefore it becomes an offset which does not effect the fractional change in the distance as a function of pressure. We will use the best-fit value for $r_0 = 2.867 \pm 0.011$ Å at ambient pressure to calculate r/r_0 with an error given by

$$\delta\left(\frac{r}{r_0}\right) = \sqrt{\left(\frac{\delta r}{r_0}\right)^2 + \left(\frac{r}{r_0^2}\delta r_0\right)^2}. \tag{4.10}$$

The results can be found in Table 4.5 with the corresponding pressure determined through the solid curve discussed in the introduction as shown in Fig. 4.1. Fig. 4.8 shows the results for the pressure within the sample as a function of the extrinsic helium pressure.

Table 4.5: List of extrinsic helium pressure in PSI to intrinsic sample pressure in GPa. The first nearest neighbor distances from Table 4.3 was converted to the fractional change from ambient pressure listed as r_1/r_0. These values were then converted to the intrinsic pressure through the equation of state data as shown in Fig. 4.1. The error in the final pressure value includes the error in the equation of state data and the error in determining the change in the first neighbor distance.

P (PSI)	r_1/r_0	P (GPa)
0	1.0000(5)	0.0(4)
1500	0.9958(3)	2.3(4)
1900	0.9924(4)	4.2(6)
2100	0.9905(3)	5.2(7)
2300	0.9910(3)	4.9(6)
2400	0.9873(6)	7.0(9)
2500	0.9869(5)	7.3(10)
2700	0.9870(7)	7.2(9)
2900	0.9834(7)	9.4(14)
3100	0.9820(6)	10.2(16)

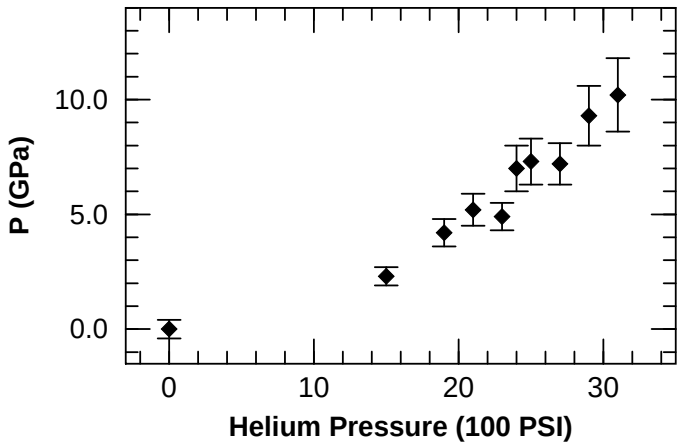

Figure 4.8: Sample pressure as a function of helium gas pressure measured in PSI.

Pressure Dependence of θ_{Debye}

As listed in Table 4.3 the pressure dependence of θ_{Debye} is just outside the uncertainties in our measurement. This is constant with Fig 4.2 where the increase in the first peak height is just outside the noise in the data, as discussed in Sec. 4.1.2.

As I discussed in Sec. 4.3, the pressure dependence for θ_{Debye} is expected to be positive and the relationship between the compression and θ_{Debye} is determined by a Grüneisen parameter, γ, in Eq. 4.2. Fig. 4.9 shows the fractional change in θ_{Debye} as a function of ϵ_{p} from which $\gamma = 0.45 \pm 0.19$. This indicates that the Nb bonds are very stiff as there is little pressure dependence of θ_{Debye}. As I listed in Table 4.2

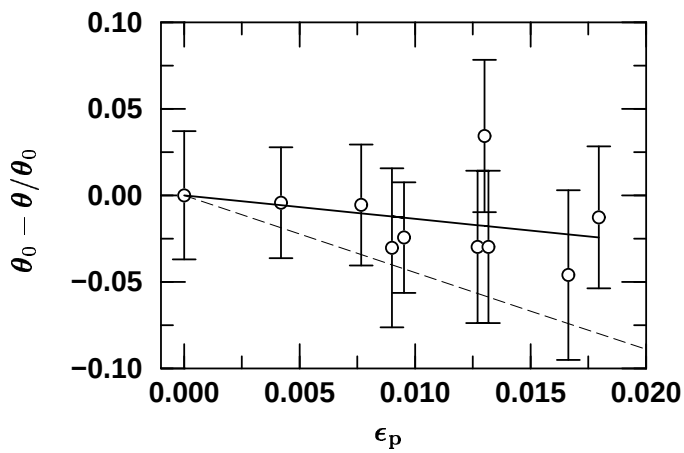

Figure 4.9: The Grüneisen relationship for Nb. The solid line represents a least squares fit to the data resulting in $\gamma = 0.49 \pm 0.19$ where the slope of this line is -3γ as given by Eq 4.2. The dashed line represents a $\gamma = 1.49$ reported in Ref. [49] for Nb at 100K.

previously measure value for γ is 1.49 from Ref. [49] which is quite a bit larger than my measured value at 0.45 ± 0.19. The dashed line in Fig. 4.9 represents a γ of 1.49.

Several Debye temperatures are listed in Ref. [50]. The values for θ_{Debye} are: 241 $\pm$ 13 K at 0 K, 260 at 298 K both from specific heat data, 340 K at 0 K from Lindemann's Equation and 328 K at 298 K from Elastic Constants. Our result for $\theta_{\text{Debye}} = 318 \pm 8$ K at 150 K and ambient pressure is slightly more consistent with the last two measurements.

Chapter 5

THE B1 TO B2 PHASE TRANSITION OF RBCL

5.1 Crystal Structure of RbCl

A phase diagram for RbCl is shown in Fig. 5.1[8]. The dashed line at room temperature corresponds to the part of the phase diagram which I have sampled. The low-pressure B1-phase has the NaCl-type structure. The high-pressure B2-phase has the CsCl-type structure. As shown in the phase diagram, the crystal structure at

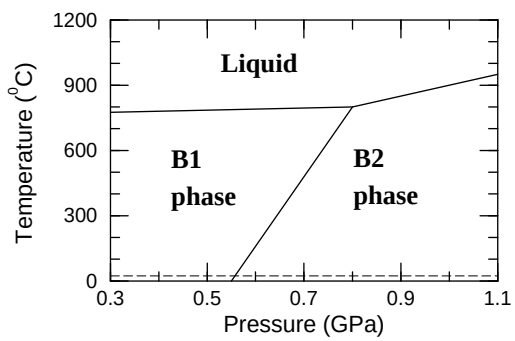

Figure 5.1: Phase diagram for RbCl. The B1-phase has the NaCl-type structure. The B2-phase has the CsCl-type structure. A cartoon of these structures can be found in Fig. 5.2. The dashed line represents the part of the phase diagram which I have sampled.

room temperature is expected to transform from the B1 to the B2 phase at approximately 0.55 GPa. I show a cartoon of theses structures in Fig. 5.2. The shells I used in the theoretical models are listed in Table. 5.1. The model for the B1-phase includes the first three shells extending about 5 Å from the absorbing atom. The model for the B2-phase includes the first four shells extending about 6 Å from the absorbing atom. No multiple scattering paths are needed to describe the data to these distances.

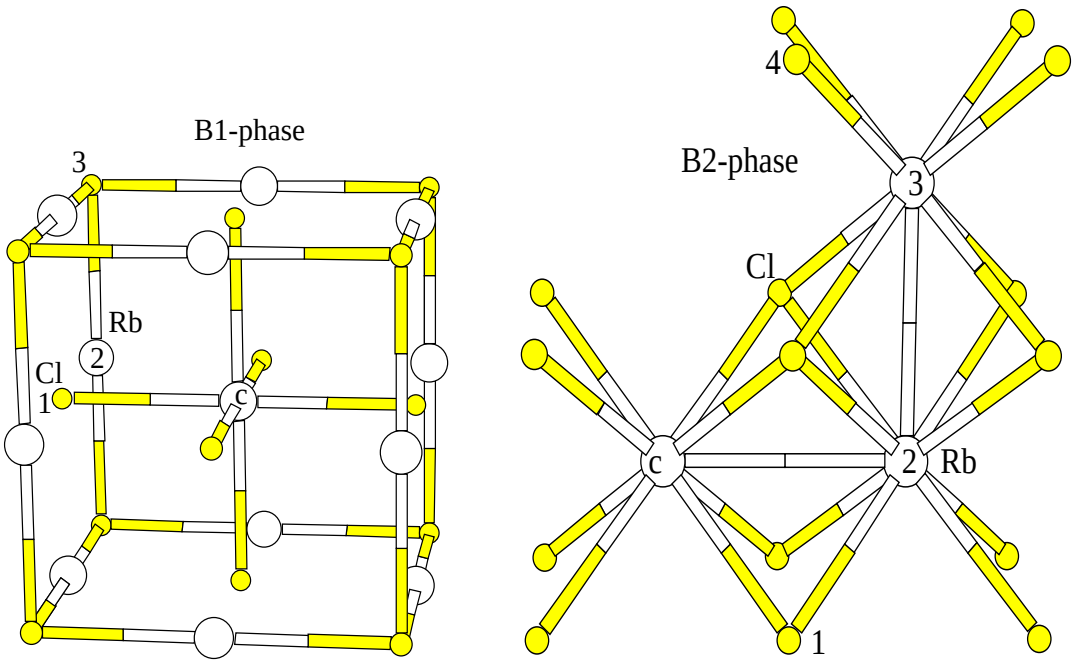

Figure 5.2: A cartoon of the B1 and B2 phases of RbCl are shown in the left and right panels, respectively. The larger open circles and the smaller shaded circles represent the Rb and Cl atoms, respectively. The bonds between the atoms are a guide the eye. The left cartoon shows one unit cell while the right shows three smaller unit cells. I have labeled the central Rb atom with the letter c, and an atom from each shell included in the model with a corresponding number based on its distance from the central atom. Table. 5.1 lists the shell's radial distance from the central Rb atom and degeneracy of the shell.

Table 5.1: List of paths for the B1 and B2 phases of RbCl. The subscripts on the atom types correspond to the labels in the cartoon for the structures shown in Fig. 5.2. The reference bond lengths and the degeneracy of each shell are listed.

Phase	Shell	Atom type	R_{ref} (Å)	N
B1	1	$Rb_c \rightarrow Cl_1$	3.295	6
	2	$Rb_c \rightarrow Rb_2$	4.660	12
	3	$Rb_c \rightarrow Cl_3$	5.707	8
B2	1	$Rb_c \rightarrow Cl_1$	3.401	8
	2	$Rb_c \rightarrow Rb_2$	3.927	6
	3	$Rb_c \rightarrow Rb_3$	5.553	12
	4	$Rb_c \rightarrow Cl_4$	6.511	24

5.1.1 Fourier Transform as a Finger Print

The magnitude of the Fourier transform of the $\chi(k)$ can be considered a finger print for a particular local structure. A detailed explanation can be found in Sec. 4.1.1 and a description of the Fourier transform procedure in Sec. 2.2.2. The $|\tilde{\chi}(R)|$ are split into three sets. The first set consists of the data measured at pressures below 0.5(1) GPa, corresponding to the B1-structure. The second set consists of data corresponding to the structure at the transition. The third set consists of data measured above 0.6(2) GPa, corresponding to the B2-structure. Examples of $|\tilde{\chi}(R)|$ for RbCl from the B1-phase, the intermediate region, and the B2-phase are shown in Fig. 5.3. These data were obtained using the Fourier transform parameters and data ranges listed in Table 5.2. As shown in Table 5.1 the second Rb→Rb shell has a radial distance of 4.67 Å in the B1-phase which decreases to 3.93 Å in the B2-phase. This large change is easily seen in the $|\tilde{\chi}(R)|$ in Fig. 5.3. The data from the transition region seems to have a contribution from both of these shells suggesting a mixture of both phases.

5.2 Alignment and Background Removal

A detailed discussion of the alignment and background removal procedure can be found in Sec. 2.2.1. Here I give the important parameters used to remove the background and show an example of the results. As outlined in Sec. 2.2.1, the value for the

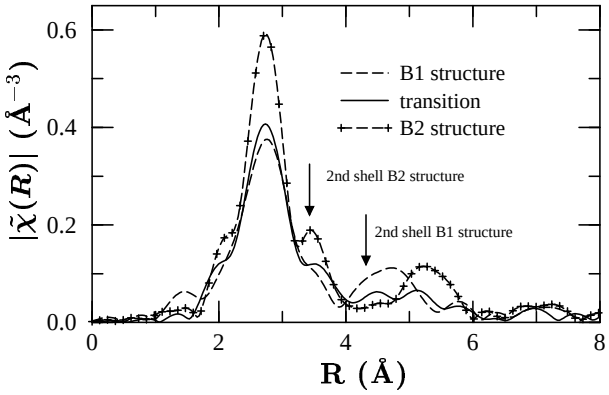

Figure 5.3: $|\tilde{\chi}(R)|$ for the B1-phase, transition region, and B2-phase of RbCl. I have labeled the second shell for the B1 and B2 phases. The transition region $|\tilde{\chi}(R)|$ seems to have some contribution from both of these shells.

Fermi energy, E_0, is set to 68% of the step height at 15185 ± 1 eV in the normalized and aligned data, and the R_{bkg} parameter is set to 1.8 Å. Given these parameters, AUTOBK finds the resulting spline of 15 knots as determined by Eq. 2.31, which it subtracts from the data to isolate the XAFS signal. An example of the μ(E)·x data and background for RbCl at ambient pressure are shown in Fig. 5.4.

Two consecutive measurements are taken at each pressure. Except at the onset of the phase transition, differences between separate measurements of μ(E)·x at a given external pressure are small and dominated by shot noise. Typically, they are averaged to increase the signal-to-noise ratio. The resulting $\chi(k)$ for two measurements of μ(E)·x taken at the same external pressure are shown in Fig. 5.5. As shown in the top panel the differences are purely caused by statistical noise and therefore, these data are averaged. The resulting $\chi(k)$ for two measurements of μ(E)·x taken at the onset of the phase transition are shown in the bottom panel. The relatively large difference between the data sets made it necessary to analyze each separately. Only at the onset of the phase transition was there any significant difference between the two measurements taken at the same applied pressure. This becomes important in the interpretation of the mechanism for the phase transition and will be discussed further in Sec. 5.6.

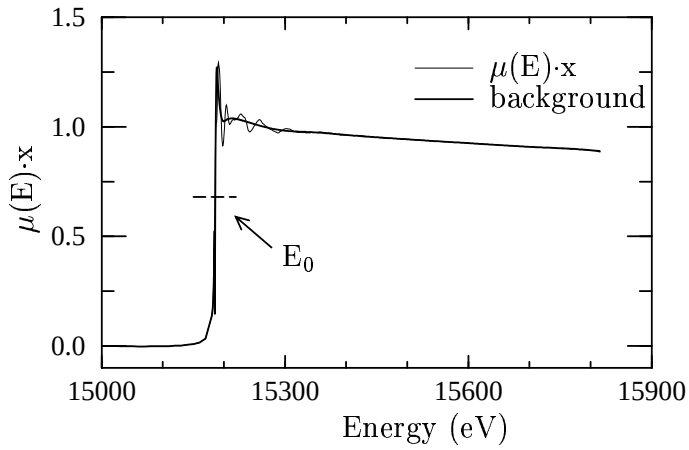

Figure 5.4: Data and background for RbCl at ambient pressure and room temperature. E_0, the Fermi energy, is set to 68% of the step height.

5.3 Overview of Fit Procedure

This is an overview of the fit procedure, which is described in detail in the next few sections. First I determine the XAFS parameters for the data corresponding to the B1- and B2-phases. The goal is to parameterize as many variables as possible so that few free parameters are needed to model the data at the transition as a mixture of both phases. These steps include:

- Determine the parameters which do not depend on pressure, S_0^2 and $\Delta E_0{}^i$.
- Reduce the fitted variables $\Delta E_0{}^i$ to a single ΔE_0.
- Determine the pressure dependent parameters, p, $\theta_{\mathrm{Debye}_i}$, and C_3^3.
- Relate $\theta_{\mathrm{Debye}_i}$ and C_3^3 to the pressure.

In the end, only two variables will be needed to determine the model for each phase, ΔE_0 and p. Even with this reduction in the number of fitted parameters, the transition region will need four fitted parameters, a ΔE_0 for each phase, p the pressure, and the fractional amount of the B1 phase x_{B1}. The fractional amount of the B2 phase, x_{B2}, is given by 1 - x_{B1}. In each of these fits the data range, fit range, Fourier transform parameters and the corresponding number of independent points are as listed in Table. 5.2 unless otherwise specified.

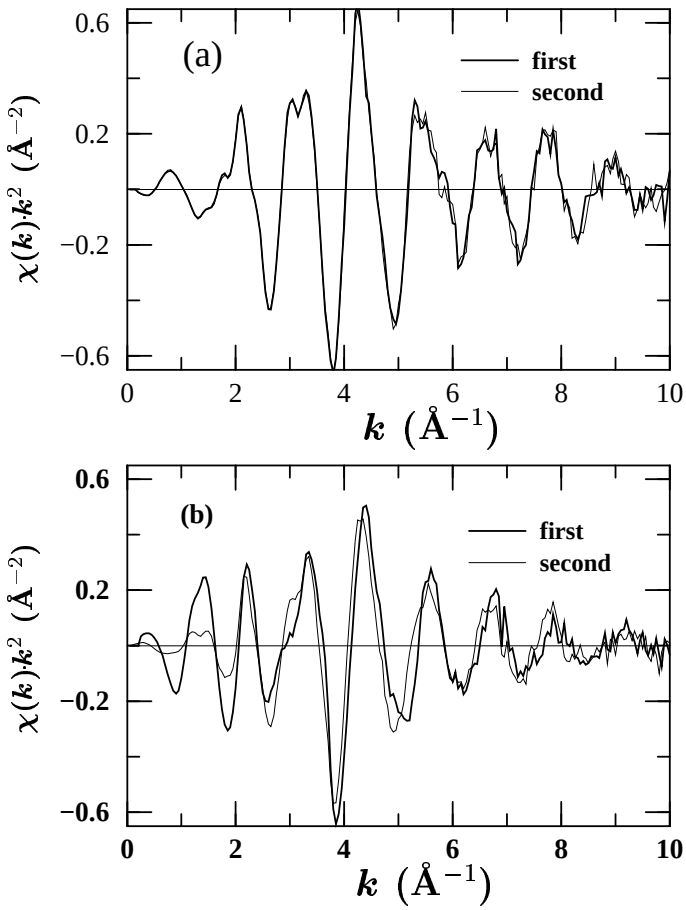

Figure 5.5: A comparison of consecutive $\chi(k)\cdot k^2$ data. Panel(a): at 0.8(1) GPa. Panel(b): at the onset of the phase transition.

Table 5.2: Fourier transform parameters along with fit and data ranges for RbCl. A detailed description of these parameters can be found in Sec. 2.2.2. The fit range is listed in R-space. The data range is listed in k-space. The Fourier transform parameters including the k-weighting, the window type and the sill widths dk are listed. The number of independent points is also listed as determined by Eq. 2.40.

Phase	R-range (Å)	k-range (Å^{-1})	Window	dk(Å^{-1})	k-weighting	N_{idp}
B1	[2.3:5.3]	[2.0:9.0]	Hanning	1.5	2	15
B2	[2.3:6.0]	[2.1:9.0]	Hanning	1.5	2	17

5.4 Analysis of the Pure B1- and B2-Phases of RbCl

In this section I will discuss the analysis of the data from the pure phases of RbCl.

5.4.1 XAFS Parameters and Meaningful Parameters

As we discussed in Sec. 5.1.1 the first three shells are included in theoretical model for the B1-phase. A detailed discussion of all the parameters can be found in Sec. 2.2.4. The parameters needed for these fits are S_0^2, $\Delta E_0{}^i$, σ_i^2, C_3^i and Δr_i. In this picture there are a total of 11 parameters for the B1-phase where the third cumulant C_3^i was determined to be important for the third shell alone.

The first four shells are included in the theoretical model for the B2-phase. The parameters I needed for these fits are the same as for the B1-phase except that the third cumulant was determined to be important for the first and fourth shells.

Many of the XAFS parameters for these shells are related in a fundamental way. The first relationship connects each bond length to a fractional compression which I discussed in Sec. 4.3. Here I extend this relationship by relating the fractional compression to the pressure. Therefore I replace the fitted parameter ϵ_p by p. In this way, the best-fit value for a single parameter p determines each bond length. I describe the details involved in this change in variables in the following subsection. The second relationship connects σ_i^2 of each shell to a Debye temperature, θ_{Debye}, with the Debye model as discussed in Sec. 4.3.

Pressure and Compression

I directly substitute the change in path length parameter Δr, for the pressure p. To do this, I use the data from Ref. [7] which gives the fraction of volume for RbCl as a function of pressure. From these data, I convert the fractional change in volume to the fractional change in lattice constant. Assuming cubic symmetry, the volume is proportional to the lattice constant cubed. Therefore $\frac{\delta v}{\delta a} = 3a^2$ and the final expression is written as

$$\frac{a}{a_0} = \frac{1}{3}\left(\frac{\Delta v}{v_0}\right) + 1 \tag{5.1}$$

where a_0 and v_0 represent the lattice constant and volume at ambient pressure and room temperature. Rather than relating the lattice constant, a to the volume, the

parameters that are more closely related to our analysis are r_{10} and r_1, the first nearest neighbor distance at ambient pressure and at the unknown pressure, respectively. Their ratio is also equal to Eq. 5.1 since the proportionality constants cancel. For example, the B1-phase has $r_1 = 0.5{\cdot}a$ and $r_{10} = 0.5{\cdot}a_0$ so $r_1/r_{10} = a/a_0$.

Of course, this relationship holds only if r_1 and r_{10} are from the same phase. The original table lists the fractional change in volume relative to volume of the B1-phase at ambient pressure and room temperature. The phase transition itself causes a 15% decrease in volume[7] therefore the data is discontinuous at the phase transition. Since the change in volume for the B1- and B2-phases after and before the transition is needed, the data is extrapolated into these regions. To make the change in volume as a function of pressure continuous, I multiplied the fractional change in volume for the B2-phase by 1.15 to erase the 15% decrease due to the phase transition. Therefore, the pressure for both phase can be calculated based on this data with the appropriate reference value. For the B1-phase, the reference value is the first neighbor distance at ambient pressure and room temperature. For the B2-phase, I equate the volume per chemical formula of 85% of the B1 to the B2 phases at ambient pressure to find an appropriate reference, r_0, for the B2 phase.

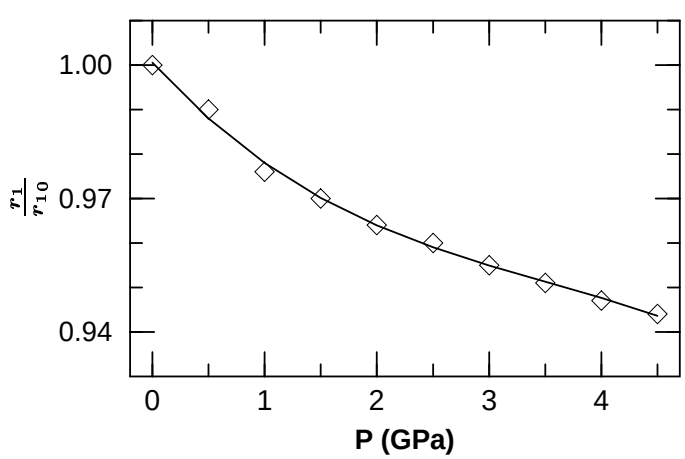

Figure 5.6: The pressure dependence of the fractional change in the first nearest neighbor distance for RbCl. The diamonds represent the experimental results converted from bulk volume measurements which can be found in Ref. [44]. The line represents a least-squares fit to these data.

The converted data, represented by the diamonds, are shown in Fig. 5.6. I also

performed a least squares fit of a cubic equation to these data which is shown in the figure as the solid line. Finally, I substitute this cubic equation which relates the lattice constant to the pressure directly into FEFFIT. In this way I have changed the fitted parameter from Δr to ϵ_{p} and then to p. The equations look something like this:

$$\begin{aligned}
\Delta \mathrm{r}_1 &= \epsilon_{\mathrm{p}} * \mathrm{R}_{\mathrm{ref1}} \\
\Delta \mathrm{r}_2 &= \epsilon_{\mathrm{p}} * \mathrm{R}_{\mathrm{ref2}} \\
\Delta \mathrm{r}_3 &= \epsilon_{\mathrm{p}} * \mathrm{R}_{\mathrm{ref3}} \\
\epsilon_{\mathrm{p}} &= ((A + B{\cdot}p + C{\cdot}p^2 + D{\cdot}p^3){\cdot}\frac{\mathrm{R}_{\mathrm{ref}}}{r_0}) - 1
\end{aligned}$$

where p the fitted parameter represents the pressure, A, B, C and D are the coefficients of the cubic equation shown in Fig. 5.6, $\mathrm{R}_{\mathrm{ref}}$ is the reference path length given to FEFF, and r_0 is the path length at ambient pressure and room temperature. I have written out the $\Delta \mathrm{r}_i$ equation for three paths to emphasize that the the single p determines all the path lengths.

5.4.2 Determination of S_0^2

As discussed in Sec. 4.4 both the k-weighting and the pressure dependence of the data can be used to break the correlations between S_0^2 and θ_{Debye}.

I simultaneously fit the theoretical models with one S_0^2 to each of the data sets using a k-weighting of w= 1, 2 and 3 for the B1-phase alone. For each data set the total number of pressure dependent parameters is eight: p, C_3^3, and $\Delta \mathrm{E}_0{}^i$ and $\theta_{\mathrm{Debye}_i}$ for each of the three shells. I have a total of 4 data sets at different pressures giving a total of 32 pressure dependent fitted parameters plus the one S_0^2. The resulting best-fit value for $\mathrm{S}_0^2 = 0.97 \pm 0.03$. Previous XAFS analysis of the temperature dependence of RbCl gave $\mathrm{S}_0^2 = 0.96$ [51] which agrees with our results.

5.4.3 Determination of ΔE_0

Next I determine $\Delta \mathrm{E}_0$. As I discussed in Sec. 4.5, it is highly correlated to a change in the path lengths. So that the fit is most sensitive to changes in energy the low k-region of the data is emphasized. Therefore a k-weighting of one is used with the Fourier transform parameters, data and fit range listed in Table 5.2. Here I fit the model to the data at each pressure independently. The value for S_0^2 is fixed at 0.97

$\pm$ 0.03 and each of our fits contains eight parameters which are: p, C_3^3, and $\Delta E_0{}^i$ and $\theta_{\mathrm{Debye_i}}$ for each shell. The resulting $E_0{}^i$ for each shell is shown in Fig. 5.7. As shown in this figure the energy shifts behave in a very predictable manor which I will use to fit the theory to the data at the transition. Namely the relative change is approximately constant: $\Delta E_0{}^i - \Delta E_0{}^{i+1} \sim Constant$. To test this constraint, I compare the reduced-χ^2 with and without it. The average R-factor and reduced-χ^2 for these fits, without any constraints on ΔE_0 are 1% and 170 respectively. If I change the variables so that only one energy shift per data set is determined in the fit, say $\Delta E_0{}^1$ and then the other two energy shifts are given by a constant offset from this value, i.e. $\Delta E_0{}^i = \Delta E_0{}^1 + Constant^i$ where the offset for the second shell is -0.43 eV and the third shell is -2.82 eV. The average R-factor and reduced-χ^2 for these fits are 1% and 130 respectively. Since the reduced-χ^2 decreases slightly this constraint does not decrease the goodness-of-fit. The expected difference between the χ^2_ν for equally acceptable models will be within two standard deviations. This can be written as $\chi^2_{i\nu}/\chi^2_{f\nu} - 1 \leq 2\sqrt{2/\nu}$, where $\sqrt{2/\nu}$ is one standard deviation. Comparing our fit with and without this constraint we have $\chi^2_{i\nu}/\chi^2_{f\nu} - 1 = 0.3$, which is about 3 times larger than $2\sqrt{2/\nu} = 1$, indicating that the constraint is a better model for the data. Therefore I will use it to predict the energy shifts for the data at the transition.

Exactly the same procedure is applied to the B2-phase so that only single energy shift is required. The resulting energy shifts are shown in the bottom panel of Fig. 5.7.

5.4.4 Determination of Pressure Dependent Parameters

The pressure dependent parameters are: the pressure, p, the Debye temperatures for each shell, $\theta_{\mathrm{Debye}_i}$, and the third cumulant, C_3^3. I fit the theoretical model to the data using $S_0^2 = 0.97 \pm 0.02$ and $\Delta E_0{}^i$ for each shell as determined in Sec. 5.4.2 and 5.4.3, respectively. The Fourier transform parameters, data and fit range are listed in Table. 5.2. These ranges give a total of 14 independent points per data set which are fitted with 5 parameters. They are p, $\theta_{\mathrm{Debye}_i}$ for each of the three shells, C_3^3. The best-fit values are shown in Fig. 5.8, represented by the open symbols. As shown in the figure $\theta_{\mathrm{Debye}_i}$ and C_3^3 have an approximately linear pressure dependence. The next step is to determine these linear relationships so that the pressure can be related to the appropriate $\theta_{\mathrm{Debye}_i}$ and C_3^3 values for the data at the transition. For comparison with the goodness-of-fit parameters for this next step, the average

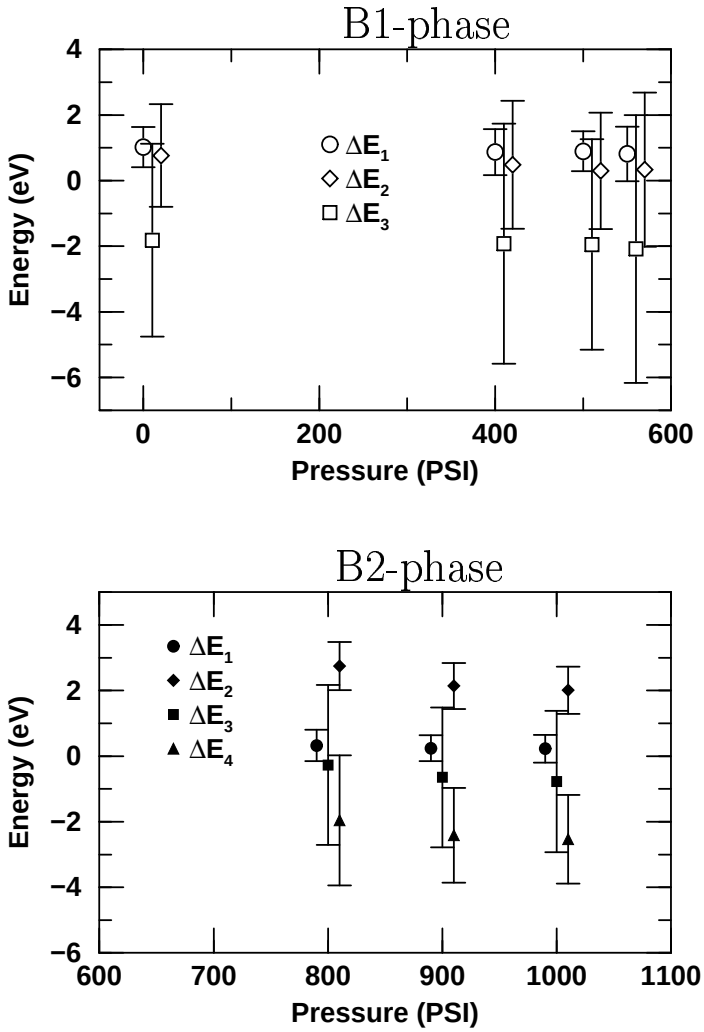

Figure 5.7: Energy shifts for the pure phases of RbCl. Top: energy shifts for the B1-phase. Bottom: energy shifts for the B2-phase. The B1-phase data was taken at 0, 400, 500, and 550 PSI, which is the external oil pressure applied to the anvils. The B2-phase data was taken at 800, 900, and 1000 PSI. I have shifted the pressure values slightly so that the error-bars from the different shells can be distinguished from each other.

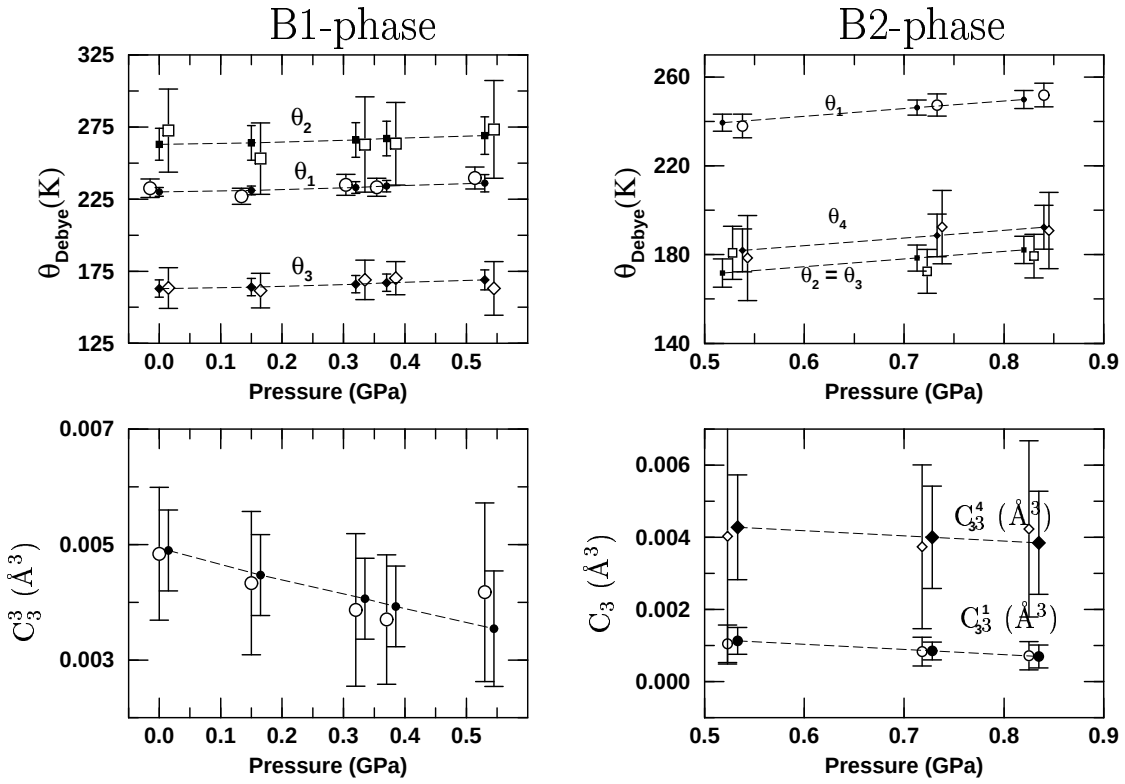

Figure 5.8: Pressure dependence of $\theta_{\mathrm{Debye}_i}$ and C_3 for RbCl. Left: Shows the results for the B1-phase. Right: Shows the results for the B2-phase. The open and closed symbols represent the best-fit value as free parameters and with a linear pressure dependence respectively. The closed symbols are connected by dashed lines, which represent the intercept and slope parameters. I have shifted the pressure slightly so that the error-bars from the different fits can be distinguished from each other.

reduced-χ^2 and $\mathcal{R}$-factor for these fits are 60 and 1%.

In a simultaneous fit I determined three intercept points and one slope for $\theta_{\mathrm{Debye}_i}$ of each shell, and an intercept and slope for C_3^3 along with the pressure of each data set. For comparison the best-fit values determined here are also shown in Fig. 5.8 represented by the closed symbols. The lines connecting these symbols represent the intercept and slope parameters which were determined by the fit. Both sets agree very well and the uncertainty in the fitted parameters is reduced by including the linear pressure dependence. The average reduced-χ^2 and $\mathcal{R}$-factor for the simultaneous fit are 48 and 1%. Since these constraints do not decrease the fit quality, I will be use them to fit the theory to the data at the transition. The best-fit value for the pressure, also determined by this simultaneous fit, is shown in Fig. 5.9.

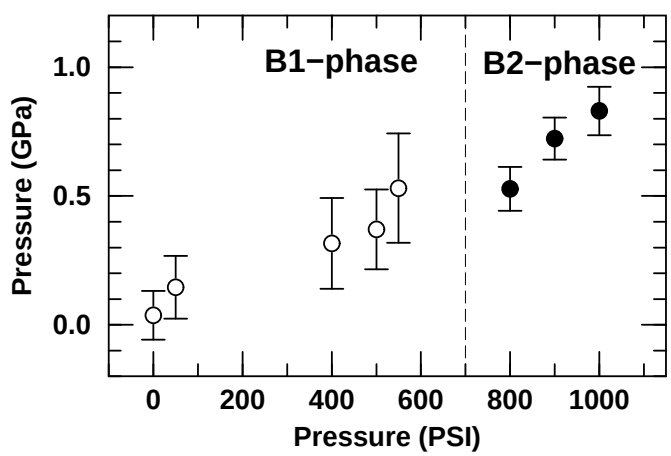

Figure 5.9: Sample pressure for the pure phases of RbCl as a function of the external PSI reading for the oil pressure. The open and closed symbols represent the data from the B1 and B2 phases, respectively.

The data corresponding to the B2-phase of RbCl is treated in exactly the same manor. The B2-phase results are shown in the figures described above next to the results for the B1-phase. Fig. 5.10 shows the experimental $|\tilde{\chi}(R)|$ along with the fitted theoretical $|\tilde{\chi}(R)|$ for the B1- and B2-phases respectively.

For completeness I have listed the θ_{Cl1}, θ_{Rb1} and θ_{Cl2} and their corresponding values for σ_i^2 as a function of pressure in Tables 5.3 and 5.4 for the B1- and B2-phases, respectively. Fig. 5.11 shows the Grüneisen relationship for θ_{Cl1} of the B1-

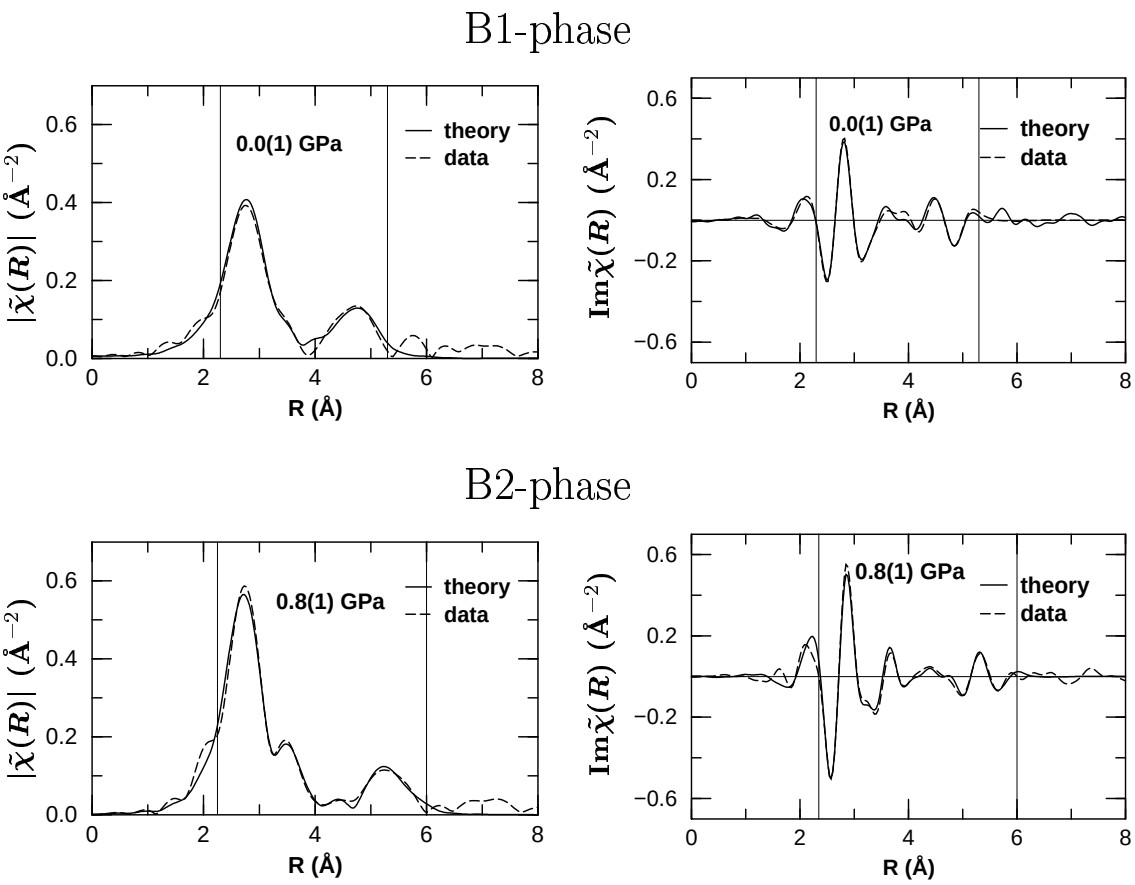

Figure 5.10: The $|\tilde{\chi}(R)|$ and $\mathrm{Im}\tilde{\chi}(R)$ for the data and theoretical model for RbCl are shown in the left and right panels, respectively. Top: Data and theory for the B1 phase at ambient pressure. Bottom: Data and theory for the B2 phase at 0.8(1) GPa. The fit range is indicated by the vertical lines.

Table 5.3: List of σ_i^2 and the corresponding θ_{Debye} for the B1-phase of RbCl

Pressure (GPa)	θ_{Cl1} (K)	σ_1^2 (Å^2)	θ_{Rb1} (K)	σ_2^2 (Å^2)	θ_{Cl2} (K)	σ_3^2 (Å^2)
0	230(3)	0.024(1)	163(6)	0.032(2)	263(12)	0.023(2)
0.2	232(2)	0.023(1)	164(5)	0.031(2)	265(12)	0.023(2)
0.3	233(3)	0.023(1)	166(6)	0.031(2)	266(12)	0.023(2)
0.4	234(3)	0.023(1)	166(6)	0.030(2)	267(11)	0.023(2)
0.5	235(5)	0.022(1)	167(16)	0.030(5)	267(20)	0.023(3)

Table 5.4: List of σ_i^2 and the corresponding θ_{Debye} for the B2-phase of RbCl

Pressure (GPa)	θ_{Cl1} (K)	σ_1^2 (Å^2)	θ_{Rb1} (K)	σ_4^2 (Å^2)
0.5	239(4)	0.023(1)	181(10)	0.046(5)
0.7	246(3)	0.022(1)	188(10)	0.042(4)
0.8	249(4)	0.021(1)	192(10)	0.041(4)

Pressure (GPa)	θ_{Cl2} (K)	σ_2^2 (Å^2)	σ_3^2 (Å^2)
0.5	171(6)	0.027(2)	0.030(2)
0.7	178(6)	0.025(1)	0.028(2)
0.8	182(6)	0.024(1)	0.027(2)

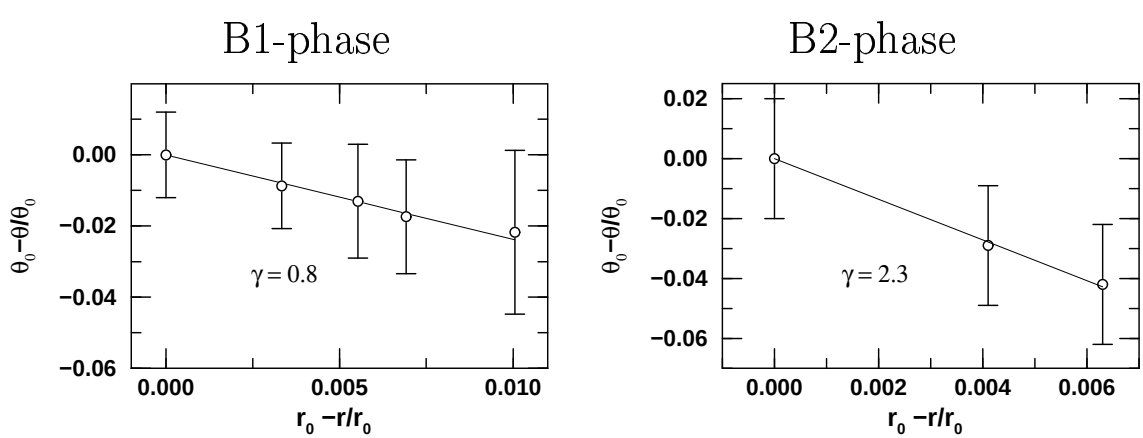

Figure 5.11: The Grüneisen relationship for θ_{Cl1} of the B1- and B2-phases of RbCl are shown in the left and right panels, respectively. The solid line represents a least squares fit to the data points. The slope of the line is -3γ as defined by Eq. 4.2 where $\gamma = 0.8 \pm 0.7$ for the B1-phase and $\gamma = 2.4 \pm 0.7$ for the B2-phase.

and B2-phases as a function of ϵ_p the fractional compression. The reference values are taken from my ambient pressure results therefore the first point is by definition at the origin.

5.5 Analysis of the Transition Region of RbCl

Most of the proceeding analysis was performed so that the transition region can be modeled as a mixture of both phases using a minimum number of free parameters. There are two reasons for doing this. The first is that only a limited number of variables that can be used to describe the data. The four free parameters are ΔE_0 for each phase, p and x_{B1} as I discussed in Sec. 5.4.1. The second reason is to know if the data is a mixture of the B1 and B2 phases without additional distortions caused by the transition mechanism. By parameterizing all the pressure dependent variables I have constrained σ_i^2 and C_3 to the values predicted by the pure phases. Thermal and static disorder that is not present in the pure phases is not accounted for in this model. Therefore any misfit which is greater than that expected from the pure phase fits gives a measure of this disorder.

5.5.1 Modeled as a Mixture of B1- and B2-Phases

The theoretical model for the data at the transition is based on the mixture of B1 and B2 structures. Table 5.5 lists the best-fit values for the pressure and the fraction of each phase along with the goodness-of-fit parameters. This table shows that the transition starts at a pressure of 0.7(1) GPa as compared to 0.55 GPa which is the reported value for the phase transition as shown in the phase diagram (Fig. 5.1). As discussed in Sec. 5.2 two measurements were taken at each pressure point. Only at the beginning of the transition were any significant differences between the two measurements taken at each applied pressure. For the data at the transition we have two sets of consecutive measurements. The first, at the onset of the transition, shows a large change in crystal structure from 76(4)% to 41(4)% B1-structure accompanied by a slight drop in pressure from 0.7(1) to 0.5(1) GPa. This slight drop may be due to the 15% decrease in volume associated with the change of phase. The next two measurements, taken at a slightly increased applied pressure, both have 17(4)% of the B1 phase and the pressure remains at 0.5(1) GPa. We interpret the slight drop in pressure between the first and next two measurements as evidence of excess pressure

that is needed to start the transition which has also been reported in Ref. [2].

Fig. 5.12 shows the experimental $|\tilde{\chi}(R)|$ for each transition point along with the theoretical $|\tilde{\chi}(R)|$ for a mixture of B1 and B2 structures. I have labeled a few of the most significant changes in the imaginary part with arrows numbered 1, 2, and 3. Going from the B1 to the B2 phase the features labeled 1 and 3 become less prominent while the feature labeled 2 is not present in the B1 phase and slowly emerges as the transition is completed. As shown by these changes in the data the transition from 100% B1 phase to 0% B1 phase are gradual as is expected for this transition where the B1-phase is being replaced by the B2-phase. The average reduced-χ^2 for these fits agrees with those for the pure phases at 25 and 28, respectively. The good agreements between the theory and data verifies the assumed linear pressure dependence of σ^2 and C_3. This indicates that the transition is dominated by a simple mixture of the B1- and B2-type structures and that the amount of disorder in the structure, reflected by these values is consistent with the applied pressure. These results also show the transition to be displacive and martensitic-like in agreement with the work of Onodera *et at.*[2].

Table 5.5: Best-fit values for the pressure and the fraction of B1-type structure, x_{B1}, along with the goodness-of-fit parameters χ^2_ν and $\mathcal{R}$-factor for the data at the transition modeled as a mixture of B1- and B2-type structures.

P (GPa)	x_{B1}	χ^2_ν	$\mathcal{R}$-factor
0.7(1)	0.76(4)	17	0.005
0.5(1)	0.41(4)	20	0.003
0.5(1)	0.17(4)	39	0.016

Test the Model for the B1- and B2-Phase Mixture

To test the mixture of phases model, I apply it to the data for which I expect only a single phase. Table. 5.6 lists the best-fit values for the pressure and the fraction of B1-phase along with the goodness-of-fit parameters using both the mixture of phases model and the pure phase model described in Sec. 5.4.4. Comparing the best-fit values of the pressure we see they are within 0.1 GPa, which is our estimated uncertainty for

the sample pressure. This is strong justification for the procedure used to determine the pressure for the data at the transition. For the first four data points listed in Table 5.6, the two-phase fit yield values for x_{B1} that are within 6% of the expected 100%, and for the last three points the two-phase fit yields values for x_{B1} that are within 1% of the expected 0%. I use the larger value of 6% as my best estimate for the uncertainty in the extracted values for x_{B1} at the transition. Fig. 5.13 shows a summary of the best-fit results of x_{B1} for all the data as a function of pressure. From the figure, the best-fit value for the pressure of 0.7(1) GPa at the first point with a significant mixture of phases is expected for this type of transition where excess pressure is required to nucleate the parent (B2) phase. This figure also shows that the transition is completed within the narrow pressure range of 0.2(2) GPa.

Table 5.6: Best-fit values for data corresponding to the structure before and after the transition for RbCl modeled as a mixture of B1 and B2 phases. Left side shows the results for a model based on the pure B1- or B2-phase. The value for x_{B1} denotes the phase where a 1 corresponds to the B1 phase and 0 corresponds to the B2 phase. Right side shows the results for a model based on a mixture of both phases. The best-fit values of pressure and the fraction of B1-type structure, x_{B1}, along with the goodness-of-fit parameters χ^2_ν and $\mathcal{R}$-factor are listed.

Single Phase Model				Mixture of Phases Model			
P (GPa)	x_{B1}	χ^2_ν	$\mathcal{R}$-factor	P (GPa)	x_{B1}	χ^2_ν	$\mathcal{R}$-factor
0.0(1)	1_f	75	0.013	0.0(1)	1.01(2)	128	0.007
0.2(1)	1_f	35	0.008	0.2(2)	0.96(9)	73	0.006
0.3(1)	1_f	27	0.016	0.4(2)	0.94(10)	41	0.011
0.4(1)	1_f	26	0.007	0.4(2)	0.98(10)	66	0.008
0.5(1)	1_f	21	0.006	0.6(2)	0.97(10)	29	0.006
0.5(1)	0_f	28	0.013	0.5(1)	0.01(3)	37	0.015
0.7(1)	0_f	17	0.011	0.7(1)	0.00(3)	22	0.012
0.8(1)	0_f	19	0.012	0.8(1)	0.00(4)	23	0.014

5.5.2 Modeled as a Distorted B1-phase

A detailed description of this intermediate structure can be found in Sec. 6.1. As a starting point for my fit based on a proposed intermediate structure, I have chosen reasonable values for certain structural parameters based on the previous results.

Figure 5.12: The $|\tilde{\chi}(R)|$ and $\mathrm{Im}\tilde{\chi}(R)$ data and theoretical model for RbCl at the transition are shown in the left and right panels, respectively. The fit range is indicated by the vertical lines. I have add the data for 100% B1-phase at the top and 0% B1-phase at the bottom for reference. I have labeled a few of the most significant changes in the imaginary part with arrows numbered 1, 2, and 3. Going from the B1 to the B2 phase the features labeled 1 and 3 become less prominent while the feature labeled 2 is not present in the B1 phase and slowly emerges as the transition is completed. As shown by these changes in the data the transition from 100% B1 phase to 0% B1 phase are gradual as is expected for this transition where the B1-phase is being replaced by the B2-phase.

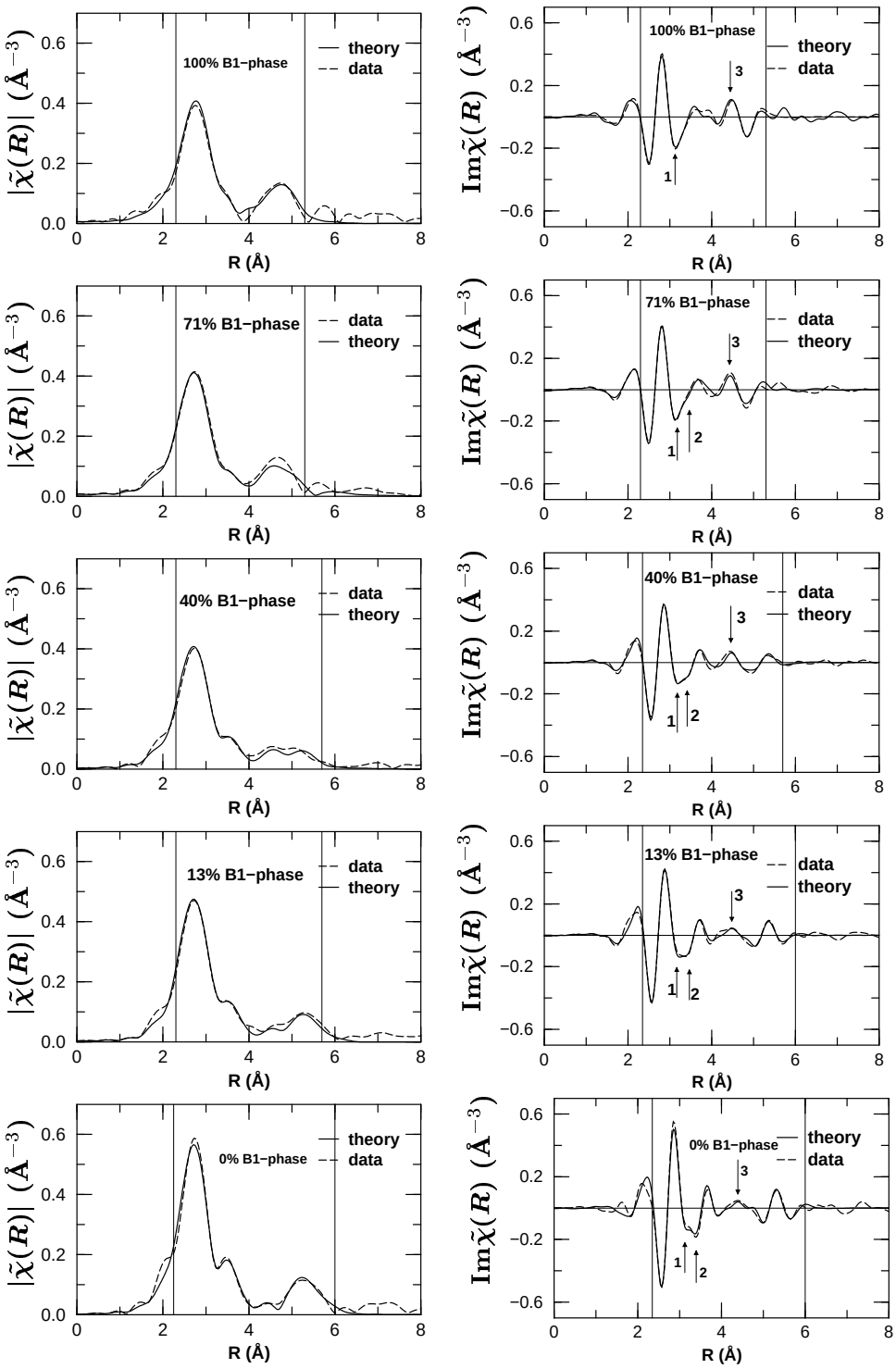
100% B1−phase
theory
data
71% B1−phase
40% B1−phase
13% B1−phase
0% B1−phase
$|\tilde{\chi}(R)|$ (Å^{-3})
$\mathrm{Im}\tilde{\chi}(R)$ (Å^{-3})
R (Å)
1
2
3

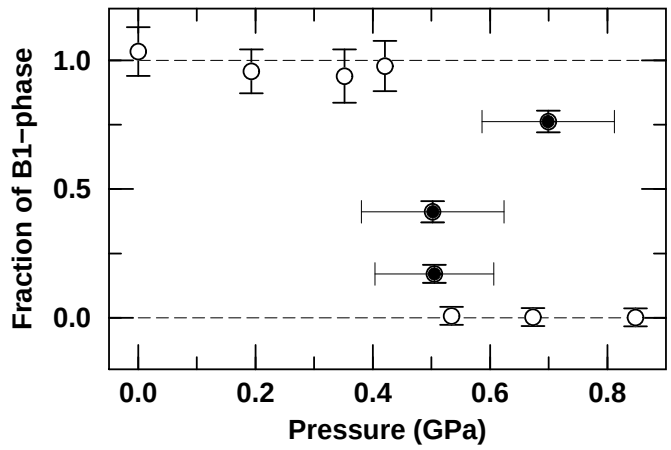

Figure 5.13: Fraction of B1-phase as a function of pressure. Data from the transition region are shown with closed symbols.

These include values for σ^2, C_3 and ΔE_0, that I have fixed to correspond to 0.7 GPa as we determined in the mixture of phases fit. The unit cell parameters a, b, c, and β are treated as fit parameters.

From Fig. 5.14 it is evident that the fit to the data at the transition is poor relative to the mixture of phases fit (Fig. 5.12). Table 5.7 lists $\mathcal{R}$ and χ^2_ν along with the number of independent points in the fit and the number of degrees of freedom in the fit. Both the $\mathcal{R}$ and χ^2_ν increase as compared to those for the fit based on a mixture of phases. The expected difference between the χ^2_ν for equally acceptable models will be within two standard deviations. This can be written as $\chi^2_{i\nu}/\chi^2_{f\nu} - 1 \leq 2\sqrt{2/\nu}$, where $\sqrt{2/\nu}$ is one standard deviation. Comparing our intermediate phase fit to the mixture of phases fit we have $\chi^2_{i\nu}/\chi^2_{f\nu} - 1 = 21$, which is about 27 times larger than $2\sqrt{2/\nu} = 0.78$, indicating that the intermediate phase model is incorrect.

For comparison, Table 5.8 lists the fit results for the both models. The most notable difference between the two structures is in the coordination number of each shell. In general, the paths from the B2-phase are not reproduced with enough degeneracy in the intermediate structure fits. This leads to a large under prediction of the data in the regions where the B2 phase contributes significantly in the mixture of phase analysis.

Finally, I allowed the unit cell parameters, the position of the atoms within the

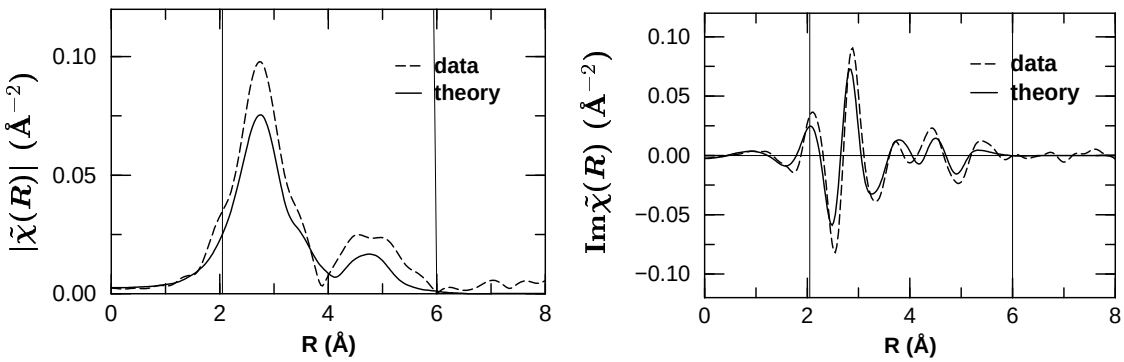

Figure 5.14: The $|\tilde{\chi}(R)|$ and Im$\tilde{\chi}(R)$ for the data and the theoretical fit for RbCl are shown in the left and right panels, respectively. The model based on the KOH-type structure is a constrained so that the θ_{Debye} and E_0 values are consistent with the results for the pure phase.

Table 5.7: Comparison of the goodness-of-fit parameters, χ^2_ν and $\mathcal{R}$-factor, along with the degrees of freedom in the fit for the model of a mixture of B1 and B2-phases (41(4)% B1 phase) and the intermediate structure at the transition.

Structure	Variables	$\mathrm{N_{idp}}$	χ^2_ν	$\mathcal{R}$-factor
Intermediate	4	17	452	0.172
B1 and B2	4	17	20	0.003

Table 5.8: Comparison of the intermediate and mixture of phases models for the transition region of RbCl. Left panel: lists the best-fit values using a model based on a mixture of B1 and B2 phases with $x_{B1} = 0.47(6)\%$. Right panel: lists the best-fit values using a model based on a KOH-type structure. Here σ^2 was set to correspond to the values predicted for the transition as determined from the mixture of phases model. The unit cell parameters: a, b, c and β were determined in the fit.

Mixture of B1 and B2 phases				Restricted KOH-type structure			
Atom type	N	R_{ref} (Å)	σ^2	Atom type	N	R_{ref} (Å)	σ^2
Rb→Cl_{B1}	6	3.26(1)	0.0225(3)	Rb→Cl	1	3.08(13)	0.0224
				Rb→Cl	2	3.29(3)	0.0224
Rb→Cl_{B2}	8	3.37(1)	0.0227(7)	Rb→Cl	1	3.30(3)	0.0226
				Rb→Cl	2	3.33(14)	0.0226
Rb→Rb_{B2}	6	3.89(1)	0.0269(12)	Rb→Rb	2	3.91(6)	0.0268
Rb→Rb_{B1}	12	4.61(1)	0.0298(5)	Rb→Rb	2	4.54(18)	0.0297
				Rb→Rb	2	4.60(11)	0.0297
				Rb→Rb	2	4.64(6)	0.0297
				Rb→Rb	2	4.75(14)	0.0297
Rb→Rb_{B2}	12	5.50(2)	0.0304(13)	Rb→Rb	2	5.25(13)	0.0303
Rb→Cl_{B1}	8	5.61(1)	0.0226(2)	Rb→Cl	1	4.95(13)	0.0225
				Rb→Cl	1	5.09(9)	0.0225
				Rb→Cl	2	5.66(12)	0.0225
				Rb→Cl	2	5.78(13)	0.0225
Rb→Cl_{B2}	24	6.45(2)	0.0463(19)				

unit cell, two Debye temperatures and two energy sifts to vary. Here I had a total of 12 parameters and 14 independent-points and the correlation between the position variables is quite high, around 85%. I was able to obtain a comparable fit for the data at the mid-transition point which we labeled at 45% B1-phase using the previous model. The data from the other two points were not reproduced using this model. Using the method described above for comparing two models, these fits are 9, 2.5, and 16.5 standard deviations worse than the mixture model. Clearly, only the midpoint can be considered a "reasonable" fit. For this model I obtained best-fit values for σ^2 that where about half of that predicted by our linear extrapolation method. This large change in the bond stiffness is highly unlikely and the fact that no "reasonable" fit was determined for the other two points suggests that this structure is not correct. Another indication that this model is not correct is that the intermediate model is reported to have an angle β= 101° which to obtain our "reasonable" fit became 90(1) degrees. This is consistent with a completely different type of distortion. I describe the original KOH-type distortion in detail in Sec. 6.1. For completeness I show the R-space data and the best-fit of the model where all 12 parameters were optimized in Fig. 5.15.

5.6 Conclusions

From the fits to the data at the transition we deduce the following properties of the phase transition. First the data were determined to be consistent with a mixture of phases and not with the intermediate KOH-type structure. Second, the phase transition requires an excess pressure at the onset of the transition of 0.2(1) GPa. Once the transition starts the system relaxes to a pressure of 0.5(1) GPa which remains approximately constant until the transition is complete. This is expected in a martensitic-like transition where the nucleation of the parent (B2) phase requires excess pressure. This also explains why the previously reported values for the transition pressure may be slightly low. Third, because the best-fit values for the σ^2's and C_3's of each shell in the single-phase regions were used to parameterize their pressure dependence and this pressure dependence was used in the model of the data at the transition, it follows from the success of these fits that the structural disorder is no larger at the phase transition than in the single-phase regions. From these results we conclude that the phase transition is consistent with a martensitic-like interpretation.

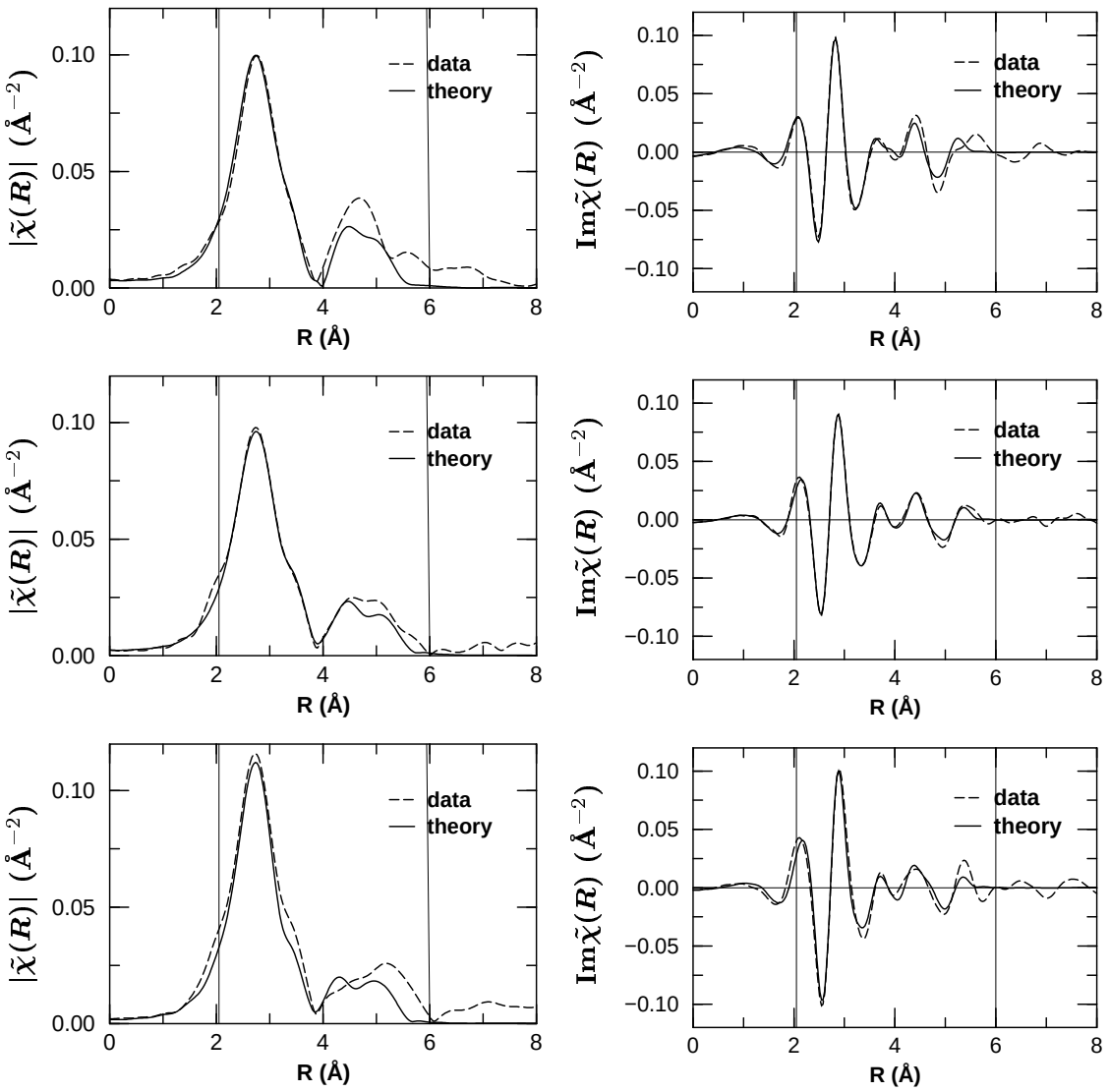

Figure 5.15: The $|\tilde{\chi}(R)|$ and Im$\tilde{\chi}(R)$ for the transition data and the theoretical fit for RbCl are shown in the left and right panels, respectively. The model is a distortion of the B1-phase based on the KOH-type structure where θ_{Debye} and $\mathrm{E}_{0\,i}$ are not constrained.

Chapter 6

LOCAL STRUCTURE OF AgCl UNDER PRESSURE

As discussed in Ch. 1, pressure induced changes in the crystal structure of AgCl are interesting since they differ from the well studied class of alkali halides with the NaCl-type structure called the rock-salts. Both the rock-salts and AgCl have B1-phase structure (NaCl-type) at ambient pressure but AgCl does not directly transform to the usual high pressure B2-phase structure (CsCl-type) as the rock-salts do. Instead the diffraction pattern becomes complicated with the appearance of many broad lines indicating a crystal structure with lower symmetry and possibly disorder[1].

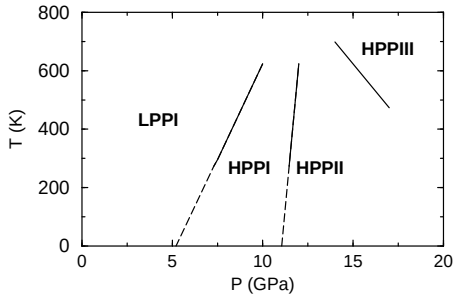

Figure 6.1: A phase diagram for AgCl[1], only the solid to solid phase transitions are shown. The low pressure phase I (LPPI) represents a NaCl-type structure or B1-phase of AgCl. The high pressure phase I (HPPI) represents a KOH-type structure. The high pressure phase II (HPPII) represents a TlI-type structure. The high pressure phase III (HPPIII) represents a CsCl-type structure or B2-phase of AgCl. The formation of the two intermediate phases between the B1 to B2 phase transition differs from that of the well studied rock salt structures. The phase diagram has been extended to low temperatures represented by the dashed lines.

The phase diagram of AgCl is shown in Fig. 6.1. This diagram was proposed as a result of recent energy dispersive x-ray diffraction work[1]. The B2-phase of AgCl is stable at very high pressures and temperatures after the formation of two distinct intermediate phases which are referred to as high pressure phase I (HPPI), KOH-type, and the high pressure phase II (HPPII), TlI-type. In the diagram the high

pressure phase III (HPPIII), CsCl-type structure, corresponds to the B2-phase. I have extrapolated the transition lines in the phase diagram, indicated by the dashes, to low temperatures as these measurements were made at 150 K. Although the structure type and unit cell dimensions have been determined at each transition and at room temperature[1] the crystal structure has not been completely determined since the position of the atoms within the unit cell are unknown. This is because it is difficult to determine the absolute intensity of the diffraction peaks due to the variation in the intensity of the x-ray source with wavelength. This creates an unique opportunity for XAFS spectroscopy which can determine the local structure given the space group and unit cell dimensions from the x-ray diffraction study[1].

6.1 Topological Relationship

A "topological" relationship between the different structural phases of AgCl was presented in Ref.[1]. The idea is that the most primitive of the space groups, the KOH-type for HPPI, can be used to reproduce each of the other structures. For example, the B1-type structure can be reproduced from the KOH-type space group with special restrictions on the lattice constants and atomic positions. The top left panel of Fig. 6.2 shows a diagram of the usual B1-type unit cell for AgCl at ambient pressure. The special KOH-type unit cell is outlined in this figure and shown by itself in the top right panel. The table following the diagrams lists the parameters necessary to reproduce the B1-phase structure in terms of both space groups. As listed in this table the unit cell dimensions as well as the position of the atoms within the unit cell are needed to define this "topological" relationship.

The "topological" relationship between the KOH-type structure and the TlI-type structure is not as well defined since the placement of the atoms within the unit cell are unknown. As a starting point for the determination of the atomic positions, I will assume, as in Ref. [1], that they are the same as for the KOH and TlI structures[45]. I will refer to this structure as the starting model. A diagram of these structures is shown in Fig. 6.3 and Fig. 6.4 for HPPI and HPPII, respectively. These starting models are based on the space group and unit cell dimensions as determined from diffraction[1]. Since they could not determine the placement of the atoms within the unit cell they are assumed to be the same as for KOH and TlI structures. The TlI-type structure as shown for the starting model can be reproduced using the KOH-type space group, forming a "topological" relationship. To demonstrate how these

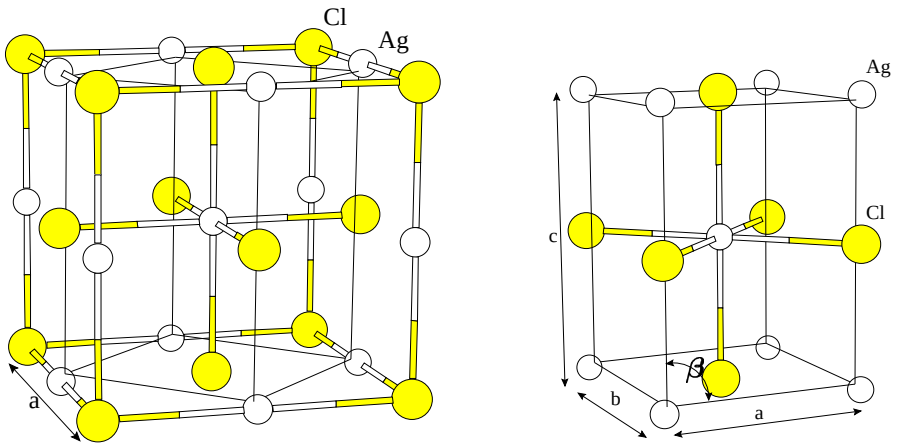

Structure Type	NaCl	KOH
Space Group	Fm3m	$P2_1$
Unit Cell Parameters (Å)	a = 5.320	a = 3.762 b = 3.762 c = 5.230 $\beta = 90°$
Atomic Positions	Cl:(0, 0, 0) (0.5, 0.5, 0) (0, 0.5, 0.5) (0.5, 0, 0.5) Ag:(0.5, 0.5, 0.5) (0, 0, 0.5) (0.5, 0, 0) (0, 0.5, 0)	Cl:(0.25, 0.25, 0.75) (0.75, 0.75, 0.25) Ag:(0.25, 0.25, 0.25) (0.75, 0.75, 0.75)

Figure 6.2: A diagram of the relationship between the NaCl-type structure and the KOH-type structure followed by a table that lists the parameters needed to specify these structures in terms of the NaCl-type and KOH-type space groups. Left: The usual B1-type unit cell for AgCl at ambient pressure. The special KOH-type unit cell is the rectangle outlined in this figure and shown by itself in the right panel. The first nearest neighbor Cl atoms are shown connected to the central Ag atom. I have shifted the KOH-type unit cell relative to the atomic positions listed in the table by a vector, $(0.25\hat{x}$,$0.25\hat{y}$, $0.25\hat{z})$, to place a Ag atom at the center of the unit cell.

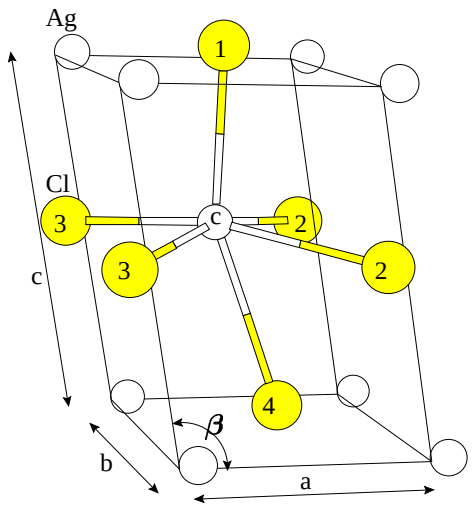

Structure Type	KOH
Space Group	$P2_1$
Unit Cell Parameters (Å)	a = 3.516 b = 3.988 c = 5.225 $\beta = 101°$
Atomic Positions	Ag:(0.175, 0.25, 0.288) (0.825, 0.75, 0.712) Cl:(0.318, 0.25, 0.770) (0.682, 0.75, 0.230)

Figure 6.3: A starting model for HPPI of AgCl. This structure corresponds to the space group and unit cell dimensions determined by x-ray diffraction[1]. Since the atomic positions are unknown they were assumed to be the same as actual KOH atomic positions. The unit cell is outlined. The first nearest neighbor Cl atoms are shown connected to the central Ag atom. I have shifted the KOH-type unit cell relative to the atomic positions listed in the table by a vector, ($0.325\hat{x}$,$0.25\hat{y}$, $0.212\hat{z}$), to place a Ag atom at the center of the unit cell.

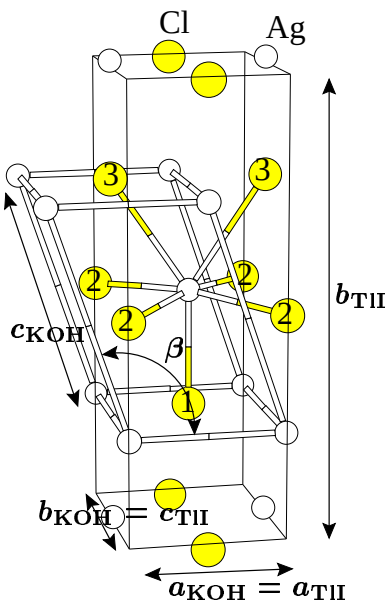

Structure Type	TlI	KOH
Space Group	Cmcm	P 2_1
Unit Cell Parameters (Å)	a = 3.350 b = 9.916 c = 4.093	a = 3.350 b = 4.093 c = 5.233 $\beta = 108.667°$
Atomic Positions	Ag:(0, 0.386, 0.25) (0, 0.614, 0.75) (0.5, 0.886, 0.25) (0.5, 0.114, 0.75) Cl: (0, 0.133, 0.25) (0, 0.867, 0.75) (0.5, 0.614, 0.25) (0.5, 0.385, 0.75)	Ag:(0.886, 0.25, 0.772) (0.114, 0.75, 0.228) Cl:(0.633, 0.25, 0.266) (0.367, 0.75, 0.734)

Figure 6.4: A starting model for HPPII of AgCl. This structure corresponds to the space group and unit cell dimensions determined by x-ray diffraction[1]. Since the atomic positions are unknown they were assumed to be the same as actual TlI atomic positions. The equivalent KOH-type unit cell is shown by the Ag atom bonds. The first nearest neighbor Cl atoms are shown connected to the central Ag atom. The table following the diagrams lists the parameters needed to reproduce this structure in terms of both space groups. I have shifted the TlI-type and KOH-type unit cell relative to the atomic positions listed in the table by a vector, ($0.5\hat{x}$, $0.114\hat{y}$, $0.25\hat{z}$) and ($0.114\hat{x}$, $0.75\hat{y}$, $0.228\hat{z}$) respectively, to place a Ag atom at the center of the TlI-type unit cell.

two structures are related both the TlI-type and the KOH-type unit cell is outlined in Fig. 6.4. The table that follows the diagram lists the atomic positions and unit cell dimensions needed to reproduce this structure in terms of both space groups. This is just one example of a "topological" relationship between the KOH-type and TlI-type structures. Both of these space groups allow for several variable position of the atoms within the unit cell. Once these positions have been determined from the XAFS data the "topological" relationship will change and could become impossible, as I discuss in Sec. 6.6. A diagram illustrating the topological relationship between each phase of AgCl is shown in Fig. 1.2 of the introduction.

6.2 A First Look at the Data

In soft materials such as AgCl the expected pressure dependence of the $|\tilde{\chi}(R)|$ data should be easily identified. Specifically, the peaks in the $|\tilde{\chi}(R)|$ data are expected to increase in height and to move to lower R-values. I discuss the physical reason for these trends in Sec. 4.1.1. To see these trends, I compare the data corresponding to the B1-phase of AgCl at ambient pressure, 2.4 and, 4.3(5) GPa which are shown in Fig. 6.5. The pressure was determined from the Nb calibrant presented in Ch. 4. The Fourier transform procedure is discussed in Sec. 2.2.2. The peaks due to the first three shells of atoms are easily identified as labeled in the figure and the following diagram for the B1-phase. The table next to the diagram lists the radial distance to each of these shells along with their degeneracy. Each of these peaks in the $|\tilde{\chi}(R)|$ increases in height and moves to lower R-values. This is an excellent example of the expected pressure effects on a stable crystal structure.

In addition to this pressure dependence, most pressure induced structural phase transitions are accompanied by an increased degeneracy of the first shell as the structure becomes more compact. For example, the degeneracy of the first shell of atoms in the B1 to B2-phase transition increases from 6 to 8 which contributes to an increase in the first peak height across the phase transition. As shown in the Fig. 6.4 and Fig. 6.3 I expect the degeneracy of the first shell to increase from 6 to 7 from HPPI to HPPII therefore an increase in the first peak height is expected if the amount of disorder remains constant. In fact, I expect the amount of disorder, represented by the splitting in the first shell, to decrease since HPPII has 4 atoms at the same distance whereas HPPI has a maximum of 2 atoms at the same distance. In each figure (Figs. 6.4 and 6.3) the atoms in the first shell are shown by the bonds connected to

B1-phase of AgCl

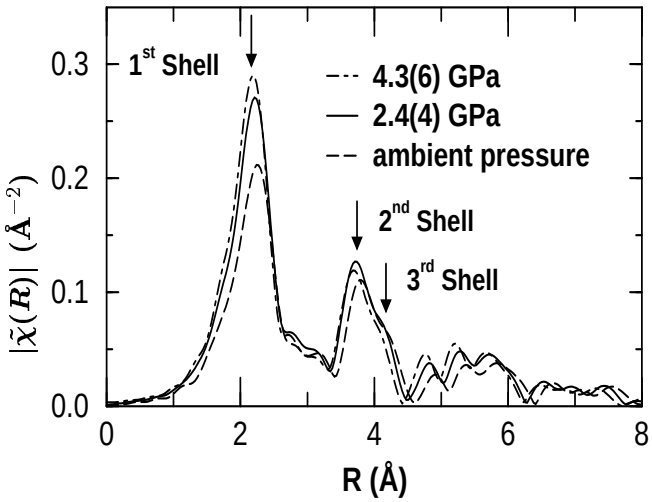

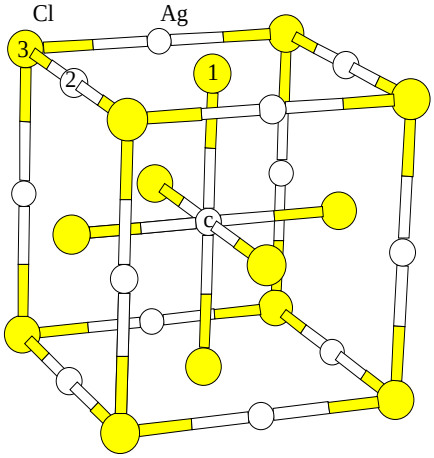

B1-phase of AgCl

atom type	R_{ref} (Å)	N_i
$Ag_c \rightarrow Cl_1$	2.715	6
$Ag_c \rightarrow Ag_2$	3.839	12
$Ag_c \rightarrow Cl_3$	4.702	8

Figure 6.5: Top: The $|\tilde{\chi}(R)|$ data for the B1-phase of AgCl. The contribution from the first three shells of atoms is labeled. Bottom left: A diagram of the B1-phase of AgCl. Bottom right: A list of the paths along with their degeneracy and half path lengths at ambient pressure. The central Ag_0 atom is labeled with a c in the diagram. Similarly the first, second and third neighbors are labeled with a 1, 2 and 3 in the diagram and correspond to the 1st, 2nd and 3rd shells labeled in the $|\tilde{\chi}(R)|$ data above.

the central Ag atom and each is labeled with a number corresponding to the distance from the central atom. From these indications I expect the peaks in the $|\tilde{\chi}(R)|$ data to increase in height and mover to lower R-values across the phase transitions. To see

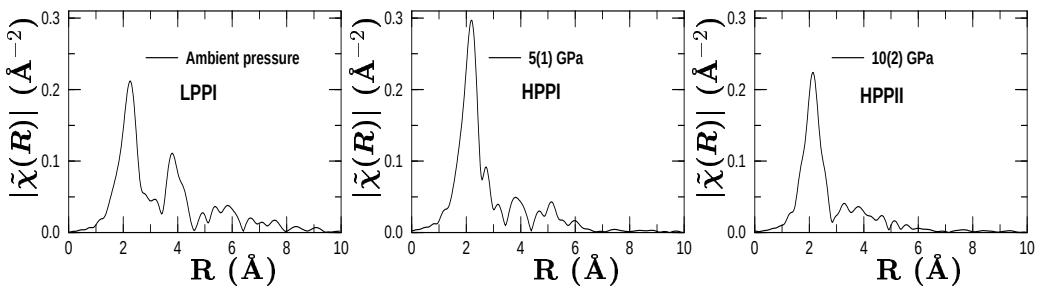

Figure 6.6: Comparison of $|\tilde{\chi}(R)|$ data for AgCl for three distinct phases: LPP at ambient pressure, HPPI at 5(1) GPa and HPPII at 10(2) GPa.

these trends, I compare the data from each of these phases of AgCl. An example of the $|\tilde{\chi}(R)|$ data, for the three distinct phases of AgCl is shown in Fig. 6.6. Comparing the first three shells of the LPPI with the other two phases we see that the 2nd and 3rd shells are not well ordered by the decreased height and increased broadening of the peaks in the same data range. Also notice that the first peak is larger in the HPPI but again smaller in the HPPII this suggests that there is more splitting in the first few Ag→Cl distances in HPPII than in HPPI. This trend of more splitting in the first shell as the pressure is increased is rarely seen. We would expect an increase in the peak height based on the increase in the number of atoms in the first shell which goes from 6 to 7 as discussed above.

6.3 B1-Phase of AgCl

In the previous section the $|\tilde{\chi}(R)|$ data for the B1-phase of AgCl at ambient pressure, 2.4 and 4.3 $\pm$ 0.5 GPa was discussed and shown in Fig. 6.5. Table 6.1 lists the data and fit ranges along with the Fourier transform parameters used to generate these data. The fit range includes all the atoms within the unit cell as shown in Fig. 6.5 along with the list of paths including their degeneracy and half path lengths at ambient pressure. The model-$|\tilde{\chi}(R)|$ is fit to each of these data sets with k-weightings $w = 1$, 2 and 3 simultaneously (see Sec. 4.4).

Table 6.1: Fourier transform parameters along with the fit and data ranges for each phase of AgCl. See Sec. 2.2.2 for detailed description of these parameters. The $\chi(k)$ data is multiplied by a Hanning window with full width of the sills given by the listed value for dk and a k^w where the value of w, called the k-weighting, is also listed.

Phase	R-range (Å)	k-range (Å^{-1})	Window type	dk(Å^{-1})	k-weighting
LPP	[1.65:4.5]	[2.5:12]	Hanning	2.0	1, 2 and 3
HPPI	[1.65:5.3]	[2.6:12.4]	Hanning	2.0	1
HPPII	[1.65:5.3]	[2.6:12.4]	Hanning	2.0	1

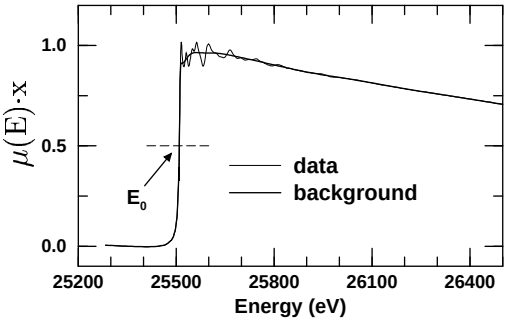

Figure 6.7: Example of the μ(E)·x data and the background function for AgCl. This data was taken at ambient pressure. The background function is a spline with 15 knots. E_0 = 25510 eV, chosen at about the middle of the step height.

6.3.1 Alignment and Background Removal

The background is removed according to the standard procedure described in Sec. 2.2.1. Here I will state the important parameters used in this procedure and show an example of the results. After normalization E_0 is set to the energy value corresponding to 50% of the step height at 25510 ± 1 eV in the normalized and aligned data. The background function μ_0(E)·x is constructed using R_{bkg} = 1.5 Å which corresponds to a spline with 15 knots, as indicated by Eq. 2.31. An example of the μ(E)·x data and the background is shown in Fig. 6.7.

6.3.2 XAFS Parameters and Meaningful Parameters

The basic XAFS parameters needed in the fit of the theoretical model to the data at each pressure are S_0^2, σ_i^2, $\Delta E_0{}^i$ and Δr_i giving a total of 10 parameters. The index i indicates that each of the three paths has its own value. Sec. 2.2.4 describes these parameters and their relation to the XAFS equation. Because of the cubic symmetry of the B1-phase structure each half-path length is expected to compress by the same factor as the pressure is increased therefore $\Delta r_i = -\epsilon_p \cdot r_{reff_i}$ where r_{reff_i} is the initial reference half-path length and ϵ_p is the fractional compression as defined by Eq. 4.1. Using this relation I reduce the three Δr_i parameters to the one fractional compression, ϵ_p. Another change of variables is made through the Debye model where a single θ_{Debye} determines σ_i^2 of different shells where the atom pairs are the same. A discussion of the Debye model can be found in Sec. 4.3. The first and third paths both contain Ag→Cl pairs therefore a single θ_{debye}^{Cl} is used, whereas the second path contains Ag→Ag pairs and is, therefore, given its own θ_{debye}^{Ag}. Each path needed its own $\Delta E_0{}^i$ due to charge transfer as I discuss in Sec. 2.2.3. This model is implemented on a trail basis and the goodness-of-fit is compared with and without these constraints. Only when the constraints did not decrease the goodness-of-fit were they used (see Sec. 2.2.4). Through the use of these constraints I reduced the number of fit parameters from 10 to 7. The final parameters varied in the fit are: S_0^2, $\Delta E_0{}^i$, ϵ_p, θ_{debye}^{Ag} and, θ_{debye}^{Cl}.

6.3.3 Determination of S_0^2

As described in Sec. 4.4 the method for determining S_0^2 is to simultaneously fit data at each pressure with k-weightings of $w = 1$, 2 and 3. The Fourier transform parameters and the fit and data ranges are listed in Table 6.1. This fit and data range includes 18 independent points per data set as given by Eq. 2.40. The number of parameters determined by the fit, as described above, is 6 for each pressure plus the one S_0^2 value. The best-fit value for $S_0^2 = 0.91 \pm 0.01$. This value for S_0^2 will be used for all the phases of AgCl as it only depends on the central atom as discussed in Sec. 2.1.2.

6.3.4 Pressure Dependences for the B1-Phase of AgCl

With $S_0^2 = 0.91 \pm 0.01$ the theoretical model is fit to the data for each pressure with 6 varied parameters. The best-fit values are listed in Table 6.2 along with the

measures of the goodness-of-fit. An example of the data at 2.4(5) GPa along with the theoretical model and fit range are shown in Fig. 6.8.

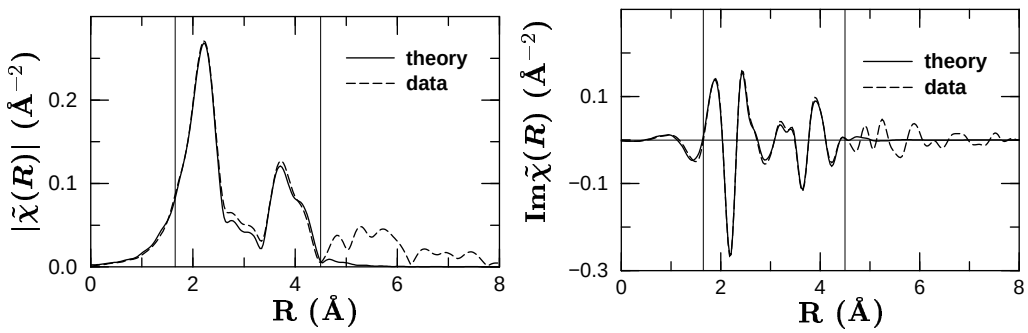

Figure 6.8: The left panel and right panels show the $|\tilde{\chi}(R)|$ and Im$\tilde{\chi}(R)$ for the data and the theoretical fit result for the B1-phase of AgCl at 2.3(5) GPa and 150K. The fit range is indicated by the vertical lines. The Fourier transform parameters and data range are listed in Table 6.1.

The value for the lattice constant at ambient pressure and 150K is found to be $a = 5.536(10)$ Å. This value is within the measured uncertainty for the lattice constant of $a = 5.526$ Å calculated from the room temperature value reported in Ref. [45] and using the thermal expansion coefficient from Ref. [52]. The values found for the energy shifts of each path, $\Delta E_0{}^i$, account for the misalignment of the data relative to the theoretical model, as well as to compensate for phase shifts due to charge transfer. Changes in $\Delta E_0{}^i$ due to the misalignment of the data relative to the theoretical model corresponds to the variation in $\Delta E_0{}^i$ for the same shell among the data taken at different pressures. As shown in the table this variation is within ± 0.5 eV which is less that our experimental resolution indicating that the alignment of the data relative to each other and the theoretical model is very good. The relative differences in $\Delta E_0{}^i$ for different shells are close to constant for each pressure point and is caused by the relative charge transfer between the atoms. Since Ag^+ has given up an electron and Cl^- has gained an electron the photoelectron which is negative will be repelled from Cl^-. This results in a negative phase shift of the photoelectron wave compared to a photoelectron which is traveling between neutral atoms as modeled in FEFF. This negative phase shift can be compensated for by an additional positive energy shift as indicated by Eq. 2.16 in Ref. [53]. Similarly an additional positive phase shift is add to the photoelectron that travels from $Ag^+ \rightarrow Ag^+$, resulting in a additional negative energy shift. Therefore a comparison of the $\Delta E_0{}^1$ and $\Delta E_0{}^2$ which correspond to

Table 6.2: The best-fit values for the B1-phase of AgCl. The pressure was determined from the Nb calibrant. The six parameters found in the fit are listed. They are an energy shift for each path, $\Delta E_0{}^i$, the fractional compression, ϵ_p, and two debye temperatures, θ^{Ag}_{debye} and θ^{Cl}_{debye}. The goodness-of-fit parameters χ^2_ν and R-factor are also listed. The reference value used to determine ϵ_p defined in Eq. 4.1 is given by the ambient pressure and 150 K unit cell dimension a = 5.536(10) Å.

P (GPa)	ϵ_p	θ^{Ag}_{debye} (K)	θ^{Cl}_{debye} (K)	χ^2_ν	R-factor
0.0(3)	0.0000(6)	162(2)	265(3)	33	0.4%
2.4(5)	0.0153(5)	166(2)	326(4)	8	0.3%
4.3(5)	0.0279(6)	156(2)	339(5)	33	0.2%

P (GPa)	$\Delta E_0{}^1$ (eV)	$\Delta E_0{}^2$ (eV)	$\Delta E_0{}^3$ (eV)
0.0(3)	3.4(2)	2.3(2)	0.6(4)
2.4(5)	2.7(2)	1.6(2)	-0.1(4)
4.3(5)	3.4(2)	2.0(3)	0.7(5)

Ag→Cl (+ΔE_0) and Ag→Ag (-ΔE_0) paths, respectively and we find that $\Delta E_0{}^1$ is on average 1.2(3) eV greater than $\Delta E_0{}^2$ as we expect from this simple picture. A comparison of $\Delta E_0{}^1$ and $\Delta E_0{}^3$ both of which correspond to Ag→Cl paths and we find that $\Delta E_0{}^1$ is on average 2.7(1) eV greater than $\Delta E_0{}^3$. This is due to the model which FEFF uses for the atomic potentials as described in Sec. 2.2.3. Briefly, FEFF screens the core-hole atom which is the central Ag atom. For ionic materials this is a bad approximation which effects the first nearest neighbor potential. To correct the core-hole screening negative charge is given back to the first nearest Cl atom which makes it more negative than the other Cl atoms. Therefore the energy shift associated with Ag→Cl_1 is more positive than the energy shift associated with Ag→Cl_3. More information about energy shifts can be found in Ref. [54].

In general the expected pressure dependence for θ_{Debye} will be positive. This is equivalent to an increase in the stiffness of the bond between the atoms as the pressure is increased and the bond length decreases. A detail discussion about the Debye model and its pressure dependence can be found in Sec. 4.3. Comparing the best-fit values for θ_{Debye} we find that this trend is true for the Ag→Cl paths, θ^{Cl}_{debye}, while there is not much change in the Ag→Ag path, θ^{Ag}_{debye}. The relationship between the change in the bond length and the change in the stiffness of the bond is determined by the Grüneisen

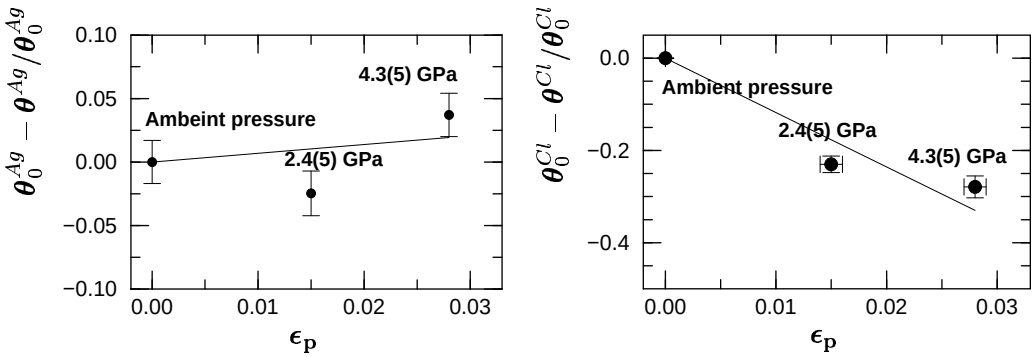

Figure 6.9: The Grüneisen relationship for the B1-phase of AgCl. The solid line represents a least squares fit to the data points. Left panel: The change in θ_{Debye} for the Ag→Ag paths. The slope of the line is -3γ as defined by Eq. 4.2 where $\gamma = -0.23 \pm 0.28$ is the Grüneisen parameter. Right panel: The change in θ_{Debye} for the Ag→Cl paths. The slope of the line is -3γ where $\gamma = 3.9 \pm 0.6$ is the Grüneisen parameter.

parameter, γ, which is defined by Eq. 4.2. Fig. 6.9 shows the fractional change in $\theta^{\mathrm{Cl}}_{\mathrm{debye}}$ and $\theta^{\mathrm{Ag}}_{\mathrm{debye}}$ as a function of ϵ_{p} the fractional compression. The reference values are taken from the ambient pressure results therefore the first point is by definition at the origin. The Grüneisen parameter for $\theta^{\mathrm{Ag}}_{\mathrm{debye}}$ is $\gamma = -0.23 \pm 0.28$ which has the wrong sign but is at least consistent with zero while the Grüneisen parameter for $\theta^{\mathrm{Cl}}_{\mathrm{debye}}$ is $\gamma = 3.9 \pm 0.6$. As shown in the figure the last data point is slightly larger than expected from the value determined by a line through the first two points for both $\theta^{\mathrm{Ag}}_{\mathrm{debye}}$ and $\theta^{\mathrm{Cl}}_{\mathrm{debye}}$. This increase could be due to an increase in static disorder due to the phase transition which occurs at the next pressure point. At least one more data point before the transition is needed to confirm this idea.

For completeness I have listed the $\theta^{\mathrm{Ag}}_{\mathrm{debye}}$ and $\theta^{\mathrm{Cl}}_{\mathrm{debye}}$ and their corresponding values for σ_i^2 as a function of pressure in Table 7.4.

6.4 HPPI of AgCl

As a starting point for the HPPI phase of AgCl, a theoretical model for the structure as shown in Fig. 6.3 is constructed. This structure uses the unit cell parameters and crystal symmetry as determined from x-ray diffraction measurements[1]. Since the atomic positions were not determined they are assumed to be the same as for actual KOH structure (see Sec. 6.1). The unit cell dimensions were determined at 9.0 GPa

Table 6.3: List of σ_i^2 and the corresponding θ_{Debye} for the B1-phase of AgCl

Pressure (GPa)	$\theta_{\mathrm{debye}}^{\mathrm{Cl}}$ (K)	σ_1^2 (Å^2)	σ_3^2 (Å^2)	$\theta_{\mathrm{debye}}^{\mathrm{Ag}}$ (K)	σ_1^2 (Å^2)
0	265(3)	0.0084(2)	0.0105(2)	162(2)	0.0122(3)
2.4	327(4)	0.0058(1)	0.0073(2)	166(2)	0.0116(3)
4.3	339(5)	0.0055(1)	0.0068(2)	156(2)	0.0130(4)

and room temperature. From the phase diagram (Fig. 6.1) these dimensions should be similar to the structure at 7.0 GPa and 150K. This corresponds to about one GPa above the phase transition expected to be around 6.0 GPa at 150K. From our data we find the phase transition at 5.3(7) GPa which is at least consistent with the phase diagram. For a comparison between our results and the diffraction results I shift the diffraction results by -3 GPa since their higher temperature corresponds to higher pressures than my results at lower temperature. This can be seen in the phase diagram by the negative slope of LPPI to HPPI transition line.

The data for HPPI was taken at 5.3(7), 5.1(7), 5.7(7) and 7.4(10) GPa as determined by the Nb calibrant (see Ch. 4). I chose to compare the data taken at 7.4(10) GPa to the theoretical model as described above. Because the model is extremely poor I fixed the parameters based on the best-fit values found for the B1-phase of AgCl. Those parameters are $\theta_{\mathrm{debye}}^{\mathrm{Ag}}$, $\theta_{\mathrm{debye}}^{\mathrm{Cl}}$ and $\Delta \mathrm{E}_0{}^i$ which were taken directly from the B1-phase at 4.3(6) GPa as listed in Table 6.2. A diagram of this structure is shown in Fig. 6.3. The first shell is shown in the diagram by the bonds that connect the Cl atoms to the central Ag atom. A table of the half path lengths and their degeneracy is shown in the right panel of Fig. 6.10. The left panel shows the $|\tilde{\chi}(R)|$ data and theoretical model along with the individual contributions from the first shell. As shown in this figure the model fails to reproduce the data. The measure of probability for two equally acceptable models is that the expected difference between the χ_ν^2 will be within two standard deviations as I discussed in Sec. 2.2.4. For this model the measures of goodness-of-fit are $\mathcal{R} = 53\%$ and $\chi_\nu^2 = 17747$ which corresponds to about 50 standard deviations away from the average fit found in Sec. 6.4.3.

The breakdown of the actual KOH atom positions within the unit cell may not be surprising if we compare the atomic radii of the K and O atoms to that of the Ag and Cl atoms. K^+ and O^{-2} have ionic radii of 1.33 and 1.40 Å respectively while Ag^+

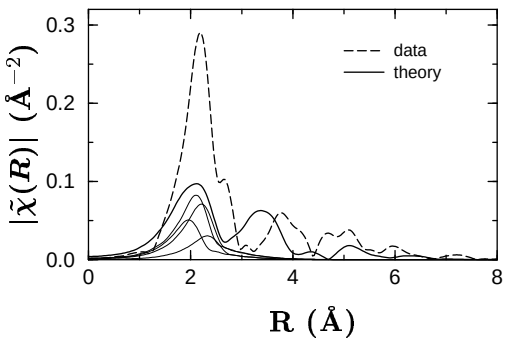

atom type	R_{ref} (Å)	N_i
$Ag_c \rightarrow Cl_1$	2.472	1
$Ag_c \rightarrow Cl_2$	2.622	2
$Ag_c \rightarrow Cl_3$	2.730	2
$Ag_c \rightarrow Cl_4$	2.846	1

Figure 6.10: Left panel: A comparison of the theoretical model $|\tilde{\chi}(R)|$ based on the starting model shown in Fig. 6.3 and the $|\tilde{\chi}(R)|$ data at 7.4(10) GPa and 150K for the HPPI phase of AgCl. The individual contributions from the first 4 nearest neighbors Cl are shown as the thin curves which are listed in the right panel along with their half path lengths and degeneracy.

and Cl^- have ionic radii of 1.26 and 1.81 Å respectively[55]. The largest difference is for the Cl^- radius which is about 25% bigger than that of O^{-2} and therefore we might expect some differences in the local structure of KOH from that of AgCl.

6.4.1 HPPI Model

The next step is to vary the position of the atoms within the unit cell to find a match to the data. The unit cell is very big, approximately 70 Å^3, therefore there are many possibilities. I can immediately conclude from the data that the first shell of Cl atoms needs to have a radial distance between 2.4 and 2.9 Å from the central Ag atom. I can also deduce that the splitting as predicted by the actual-KOH atomic positions is too large to describe the XAFS data as the first peak height for the theoretical model with this splitting is too small as compared to the data (Fig. 6.10). As a test, the first peak of the $|\tilde{\chi}(R)|$ data at 7.4(10) GPa can be fit with a single Ag→Cl path were the degeneracy, half path length and θ_{Debye} are determined. The result gives the first peak except for the shoulder (the data is shown in Fig. 6.10) as a single Ag→Cl shell at a distance of 2.68 ± 0.01 Å with a $\theta_{\text{Debye}} = 315 \pm 50$ K and a degeneracy of 6.3 ± 0.7. The measures of goodness-of-fit are $\chi^2_\nu = 2333$ and R-factor = 1%. The fit range in $\Delta R = [1.65{:}2.65]$ includes 7 independent points. This result shows that the splitting of the first Cl atoms as expected from the KOH-atomic positions listed in Fig. 6.10 does not describe the data.

The model structure needs to be close to the actual structure before a fit can be

considered, so a program was written to cycle through the possible atomic positions within the unit cell. This program calculates the radial distribution about a Ag atom (writes `atoms.inp` file and then runs ATOMS about a billion times). Then it checks the first shell of Cl atoms. If the first shell is at about 2.68 Å from the Ag atom then the theoretical $|\tilde{\chi}(R)|$ is calculated and compared with the data as in our example above for the starting model (Fig. 6.10). The final candidates are then grouped based on the splitting of the first Cl shell. From these groups I systematically eliminated all but one by considering the goodness-of-fit. I found that the shoulder of the first peak must be due to a Ag shell based on its shape. I also found that an added symmetry which is present in KOH and in the B1 and B2-phases of AgCl is needed. This symmetry is that the y position for the Ag and Cl atoms within the unit cell had to have the same value. This means that the [101] plane is a mirror plane.

Our final result for the radial distribution function about a Ag atom at 5(1) GPa is shown in the right panel of Fig. 6.11. Our fit range ΔR =[1.65:5.3] Å includes about 40 paths. Due to the large degree of splitting I found that all the paths with an amplitude greater than 5% of the first path as determined by FEFF[56] contributed significantly to the model. As shown by the labels in the figure, I formed 5 Ag→Ag groups and 4 Cl→Cl groups based on their distance from the central Ag atom. Several different constraints were placed on these groups. Originally, one Debye temperature and one energy shift is determined for all Ag→Ag paths and another for all Ag→Cl paths. Once a reasonable fit is found by varying the unit cell parameters, the two Debye temperatures and the two energy shifts, the fit is refined by allowing each group to have its own θ_{Debye} and $\Delta \mathrm{E}_0{}^i$. I found that this gave the model too much freedom, as I obtained an excellent fit with unreasonable $\Delta \mathrm{E}_0{}^i$ values therefore I constrain some of the groups. The best-fit with reasonable parameters is obtained by allowing the first Ag and Cl shells to have there own energy shifts. I also found that several Debye temperatures improved the goodness-of-fit. A table of the final varied parameters and their notation are shown in the right panel of Fig. 6.11.

6.4.2 Crystal Structure and Radial Distribution

A diagram of the HPPI structure is shown in Fig. 6.12 along with a table listing the unit cell parameters. I denote the atomic positions within the unit cell as j_{Ag} and j_{Cl} where j = x, y, z. As stated above the values for y_{Ag} and y_{Cl} needed have the same value which imposes a mirror symmetry about the [101] plane. Since XAFS is

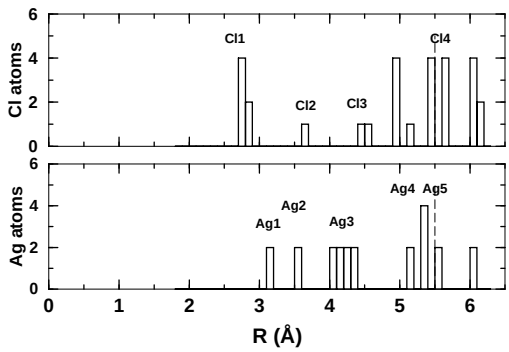

Group	θ_{Debye}	$\Delta E_0{}^{i}$
Cl_1	θ_{Cl1}	$\Delta E_0{}^{Cl1}$
Cl_2	θ_{Cl2}	
Cl_3	θ_{Cl2}	$\Delta E_0{}^{Cl2}$
Cl_4	θ_{Cl2}	
Ag_1	θ_{Ag1}	$\Delta E_0{}^{Ag1}$
Ag_2	θ_{Ag2}	
Ag_3	θ_{Ag3}	$\Delta E_0{}^{Ag2}$
Ag_4	θ_{Ag2}	
Ag_5	θ_{Ag4}	

Figure 6.11: The local structure as determined from the XAFS data. Left panel: The radial distribution of Cl atoms, top, and Ag atoms, bottom, about a Ag atom. Paths were grouped together depending on their distances as shown by the labels. Right panel: XAFS parameters for each group that were varied in the fit of the theoretical model to the data. The atomic subscripts indicate the shell index; all Cl and Ag atoms sit in crystallographic-equivalent positions.

sensitive to the radial distribution function I cannot determine the value of $y_{Ag} = y_{Cl}$ but only their relation, as explained below.

XAFS measures the radial distribution of atoms about a specific atomic species[13]. Here I measured the radial distribution about Ag atoms in AgCl. The crystal structure is given by the space group and the unit cell parameters which includes the cell dimensions, denoted as a, b, c and β, and the fractional position of the Ag and Cl atoms within the unit cell. There are actually two Ag and two Cl atoms inside each the unit cell. The first Ag atom is placed at (x_{Ag}, y_{Ag}, z_{Ag}) and the second Ag atom is placed at $(x_{\bar{A}g}, y_{Ag} + .5, z_{\bar{A}g})$ and similarly for the Cl atoms. XAFS measures the difference between the placement of the Ag atom and the surrounding atoms therefore the expression for the first nearest neighbor Cl atoms goes like

$$d^2_{Ag\rightarrow Cl} \sim ((x_{Ag} - x_{Cl})\cdot a)^2 + ((y_{Ag} - y_{Cl})\cdot b)^2 + ((z_{Ag} - z_{Cl})\cdot c)^2 \qquad (6.1)$$

This expression is just approximate since, for simplicity the β dependence has been neglected. As mentioned above as long as the values for y_{Ag} and y_{Cl} are the same the absolute value cannot be determined. This is because the coefficient for the second term on the right side of Eq. 6.1 is always zero or one half. As stated above this constraint is found to be true and so we chose to fix the value for $y_{Ag} = y_{Cl} = 0.25$ as found for the atomic positions of KOH. Let me emphasize that regardless

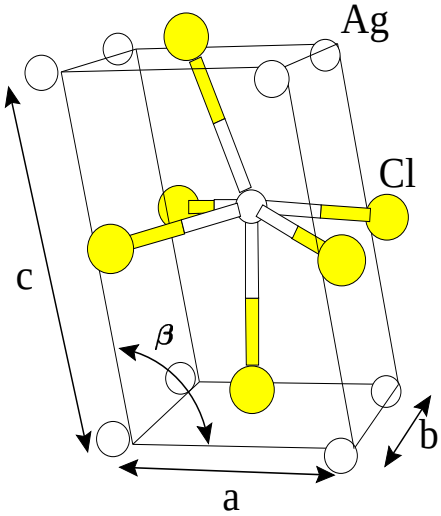

Structure Type	KOH
Space Group	$P2_1$
Unit Cell	a = 3.44(6)
Parameters	b = 3.99(6)
(Å)	c = 5.41(12)
	$\beta = 99(2)^\circ$
Atomic	Ag: (0.156(11), 0.25, 0.200(4))
Positions	(0.844, 0.75, 0.800)
Positions	Cl: (0.314(28), 0.25, 0.722(7))
Positions	(0.686, 0.75, 0.278)

Figure 6.12: The final model for HPPI of AgCl as determined by the XAFS data. Left panel: A diagram of the HPPI of AgCl. The bonds connect the first shell of atoms to the central Ag atom which includes six Cl atoms and two Ag atoms. Right panel: The crystal structure parameters including the best-fit values for the unit cell dimensions and the fractional position of the Ag and Cl atoms within the unit cell. I have shifted the KOH-type unit cell relative to the atomic positions listed in the table by a vector, $(0.344\hat{x}, 0.25\hat{y}, 0.30\hat{z})$, to place a Ag atom at the center of the unit cell.

of the absolute value, as long as $y_{Ag} = y_{Cl}$ the radial distribution and therefore the theoretical XAFS model are identical.

6.4.3 HPPI Results and Pressure Dependence

The data and the resulting theoretical model at each pressure are shown in Fig. 6.13. The most dramatic pressure induced change in the data can be seen in the shoulder of the first peak. The best-fit values found for our varied parameters as described above are shown in Fig. 6.14. There is a total of 18 varied parameters in the fit of the theoretical model to the data which contained about 25 independent points. The average measures of goodness-of-fit are $\mathcal{R} = 0.2\%$ and $\chi^2_\nu = 665$. The uncertainties in the fit parameters are quite large due to the correlations between the four atomic position parameters and the four unit cell dimension parameters. The top row shows the energy shifts for each group of paths. A comparison of the first shell energy shifts with those found for the B1-phase give some confidence in the fit. For the B1-phase I found an average $\Delta E_0 = 2.0(5)$ and 3.2(5) eV for the first Ag and Cl shell respectively which is similar to our results here which average at 1.7(5) and 3.1(5) eV for the first Ag and Cl shell respectively. The next row and a half shows the best-fit values for the Debye temperatures. Because of the splitting, about 40 paths were used in the theoretical model while only a few Debye temperatures could be varied in the fit. The Ag→Ag paths were found to have more of an impact on the quality of the fit since the scattering from a Ag atom is stronger than that of the Cl atoms. Therefore, as indicated in the right panel of Fig. 6.11, I grouped the Ag→Ag paths into four groups each with its own Debye temperature and I grouped the Ag→Cl paths into only 2 groups which gave the first shell its own Debye temperature. As a result the error in these parameters is quite large and we hardly see any pressure dependence, maybe a slight pressure dependence for the first Ag shell which corresponds to the shoulder of the first peak. The uncertainty in the first Cl shell are about ± 500 K which are not shown in the figure since they are about as large as the best-fit values. These values are highly correlated, by about 80%, to the c dimension of the unit cell which is partly responsible for the large uncertainties. The left side of row three shows the best-fit values for the atomic positions. The average values are Ag:(0.154(9), 0.25, 0.198(3)) and Cl:(0.692(19), 0.25, 0.281(14)). I did not find that these values or the angle β, shown in the bottom row, changed with pressure suggesting that this structure is stable in this pressure region. The last row show the best-fit values for the

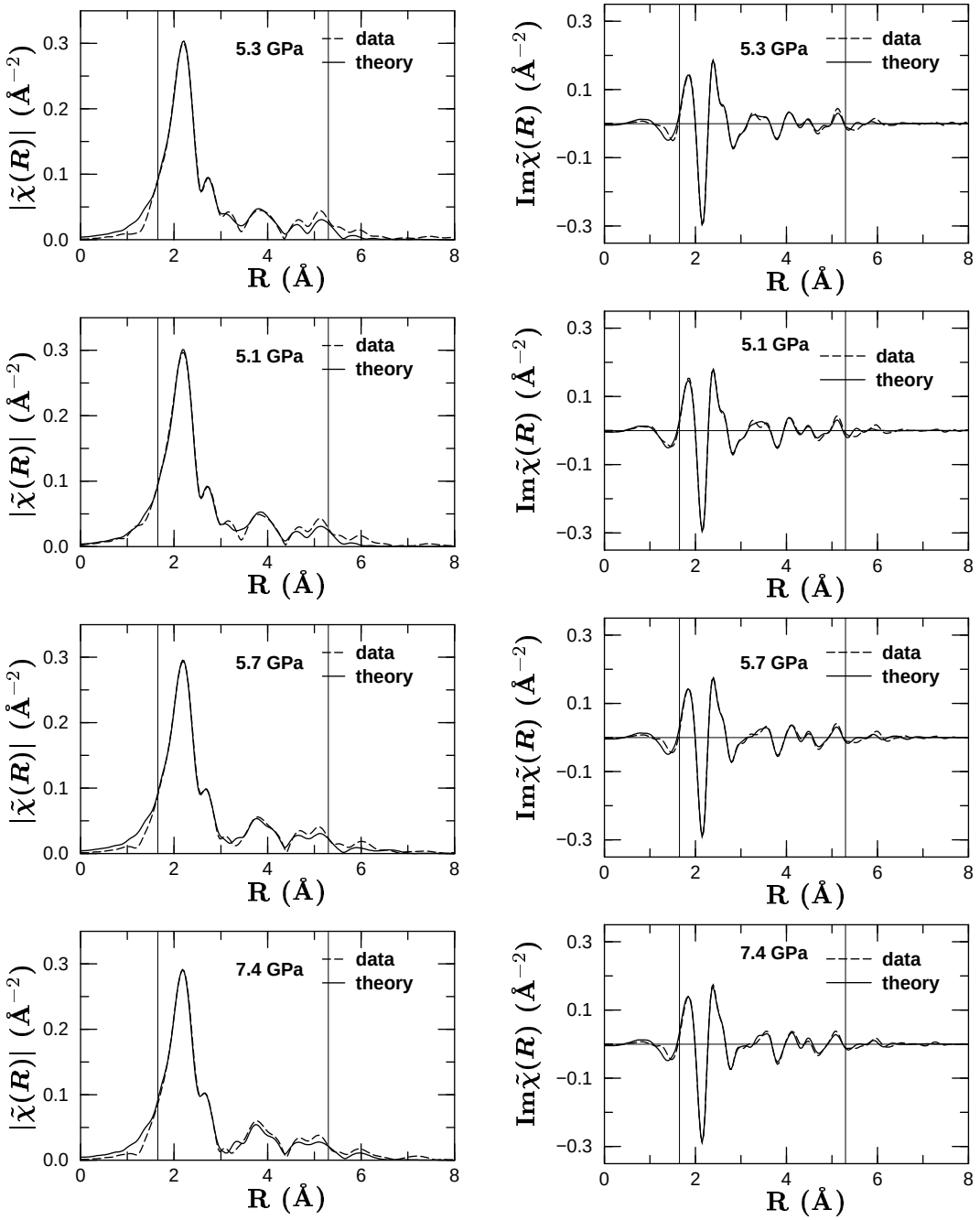

Figure 6.13: Data and theoretical model for HPPI of AgCl. Left side: $|\tilde{\chi}(R)|$ data and theoretical model. Right side: Im$\tilde{\chi}(R)$ data and theoretical model. The vertical lines represent the fit range. The Fourier transform parameters are listed in Table 6.1.

angle β and the unit cell dimensions. The closed symbols represent the diffraction[1] results which agree well with my results. I have shifted their results by -3 GPa for better comparison with our results which is due to the difference in temperature as I discussed in Sec. 6.4.

For completeness I have listed the θ_{Ag1} and θ_{Cl1} and their corresponding values for σ_i^2 as a function of pressure in Table 6.4.

Table 6.4: List of σ_i^2 and the corresponding θ_{Debye} for the KOH-type of AgCl

Pressure (GPa)	θ_{Cl1} (K)	σ_1^2 (Å^2)	θ_{Ag1} (K)	σ_5^2 (Å^2)
5.3	559(703)	0.003(23)	178(29)	0.009(3)
5.1	677(1100)	0.002(65)	180(32)	0.009(3)
5.7	738(1240)	0.002(85)	196(31)	0.007(2)
7.4	797(1800)	0.002(500)	207(45)	0.007(3)

6.5 HPPII of AgCl

The data for the HPPII of AgCl was taken at 9.4 and 10.4 $\pm$ 1 GPa as determined by the Nb calibrant presented in Ch. 4. The Fourier transform parameters, data and fit ranges are listed in Table 6.1. The starting model is constructed using the space group and unit cell dimensions from Ref. [1] since the atomic positions were not determined they were assumed to be the same as for the TlI structure. A diagram of this structure is shown in Fig. 6.4 where the first shell is indicated by the bonds that connect the Cl atoms to the central Ag atom. The parameters that were varied in the fit are $\theta_{\mathrm{debye}}^{\mathrm{Ag}}$, $\theta_{\mathrm{debye}}^{\mathrm{Cl}}$ and $\Delta \mathrm{E}_0$. This model is shown with the data at 9.4 GPa in the left panel of Fig. 6.15. The right panel lists the path lengths and degeneracy for the first shell. The best-fit values for our three varied parameters are $\theta_{\mathrm{debye}}^{\mathrm{Ag}} = 96(65)$, $\theta_{\mathrm{debye}}^{\mathrm{Cl}} = 386(113)$ and $\Delta \mathrm{E}_0$ = -0.9(1.6) and the goodness-of-fit parameters R = 28% and $\chi_\nu^2 = 8500$. The measure of probability for two equally acceptable models is that the expected difference between the χ_ν^2 will be within two standard deviations as I discussed in Sec. 2.2.4. This model corresponds to about 70 standard deviations from the average fit found in Sec. 6.5.2 indicating that this starting model fails.

Figure 6.14: Best-fit values for the HPPI of AgCl. Left side: the results for Ag→Ag paths. Right side: The results for Ag→Cl paths. The bottom row shows our results for the unit cell dimensions with the open symbols at 150K and the diffraction results with the closed symbols at 293K. I have shifted the diffraction results by -3 GPa for a better comparison with our results as discussed in Sec. 6.4. There is a total of 18 parameters and 25 independent points in the fit and data range.

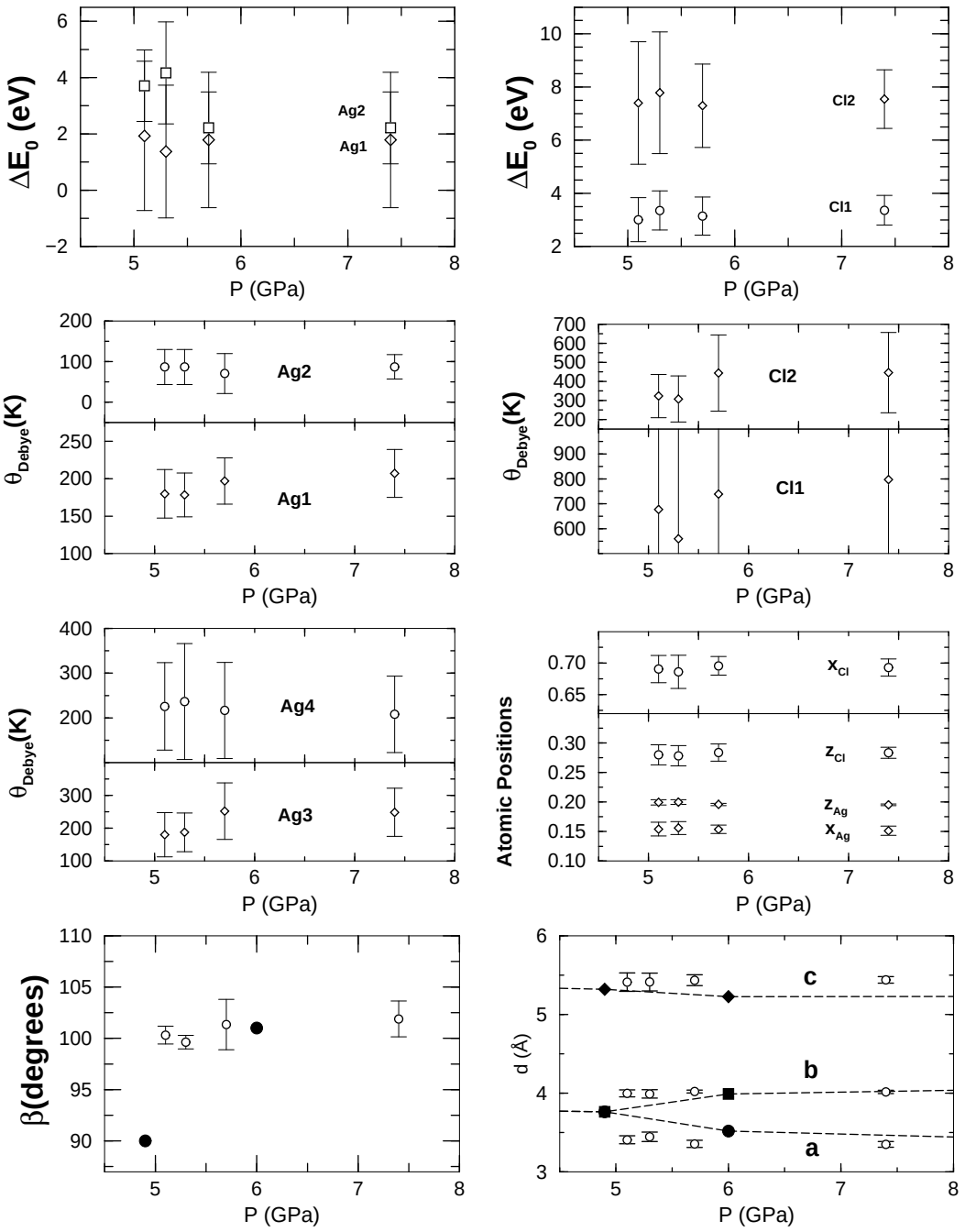
ΔE0 (eV)
Ag2
Ag1
P (GPa)
ΔE0 (eV)
Cl2
Cl1
P (GPa)
θDebye(K)
Ag2
Ag1
P (GPa)
θDebye(K)
Cl2
Cl1
P (GPa)
θDebye(K)
Ag4
Ag3
P (GPa)
Atomic Positions
xCl
zCl
zAg
xAg
P (GPa)
β(degrees)
P (GPa)
d (Å)
c
b
a
P (GPa)

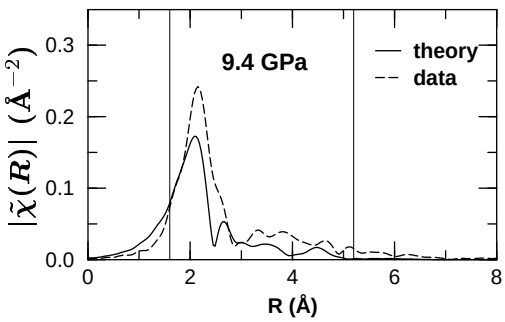

atom type	R_{ref} (Å)	N_i
$Ag_0 \rightarrow Cl_1$	2.506	1
$Ag_0 \rightarrow Cl_2$	2.647	4
$Ag_0 \rightarrow Cl_3$	2.966	2

Figure 6.15: Data and theoretical model based on the starting model for HPPII of AgCl. Left panel: A comparison of the theoretical model based on the structure shown in Fig. 6.4 and the data at 9.4(10) GPa and 150K for the HPPII phase of AgCl. Right panel: The first 3 nearest neighbors Cl are listed along with their half path lengths and degeneracy.

6.5.1 HPPII Model

The position of the 4 Ag and 4 Cl atoms within the unit cell are determined by the relationships shown in Table 6.5.1. The TlI-type structure has two undetermined values for the position of the atoms within the unit cell, y_{Ag} and y_{Cl}. The structure, therefore, is determined by 5 parameters: a, b, c, y_{Ag}, and y_{Cl}.

The final result for the radial distribution of atoms about a Ag atom for HPPII of AgCl is shown in the left panel of Fig. 6.16. The atoms were grouped according to their distance from the central Ag atoms as labeled in the figure. I found that three Ag→Ag groups and two Ag→Cl groups were needed. The right panel of Fig. 6.16 lists the group dependent variables used to fit the model to the data.

6.5.2 HPPII Results and Pressure Dependence

The data and the resulting theoretical model at each pressure are shown in Fig. 6.18. The best-fit values for the parameters described above are shown in Fig. 6.19. A total of 13 parameters where varied in the fit of the model to the data which contained about 22 independent points. The average measures of goodness-of-fit are $\chi^2_\nu = 268$ and $\mathcal{R} = 0.3\%$. The uncertainties in the fit parameters are quite large due to correlations between the two atomic position and the three unit cell dimensions. The top row shows the energy shifts for each group of paths. Comparing the relative difference of the energy shifts for the first Cl shell and the first Ag shell, I find that ΔE_0 for the Cl shell are about 3.3 ± 3 eV greater than the ΔE_0 for the Ag shell. This result is

Table 6.5: The atomic positions for the crystal structure of the HPPII of AgCl. The only undetermined values are y_{Ag} and y_{Cl}.

Atom type	position within unit cell		
Cl	(0,	y_{Cl},	0.25)
Cl	(0,	-y_{Cl},	0.75)
Cl	(0.5,	y_{Cl}+0.5,	0.25)
Cl	(0.5,	-(y_{Cl}+0.5),	0.75)
Ag	(0,	y_{Ag},	0.25)
Ag	(0,	-y_{Ag},	0.75)
Ag	(0.5,	y_{Ag}+0.5,	0.25)
Ag	(0.5,	-(y_{Ag}+0.5),	0.75)

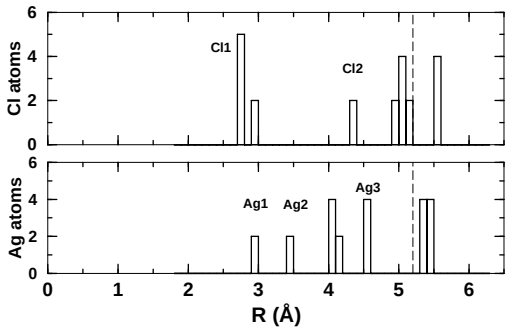

Group	θ_{Debye}	$\Delta E_0{}^{i}$
Cl_1	θ_{Cl1}	$\Delta E_0{}^{Cl1}$
Cl_2	θ_{Cl2}	$\Delta E_0{}^{Cl2}$
Ag_1	θ_{Ag1}	$\Delta E_0{}^{Ag1}$
Ag_2	θ_{Ag2}	$\Delta E_0{}^{Ag2}$
Ag_3	θ_{Ag1}	$\Delta E_0{}^{Ag2}$

Figure 6.16: The radial distribution of atoms for the final model of HPPII of AgCl based on the best-fit to the XAFS data. Left panel: The radial distribution of Cl atoms, top, and Ag atoms, bottom about a Ag atom. Paths were grouped together depending on their distances as shown by the labels. Right panel: XAFS parameters that were group dependent and varied in the fit of the theoretical model to the data. The atomic subscripts indicate the shell index; all Cl and Ag atoms sit in crystallographic-equivalent positions.

similar to our findings for the B1-phase where ΔE_0 for the first Cl shell was about 1.1 ± 1 eV greater than ΔE_0 for the first Ag shell. The next row shows the best-fit values for the Debye temperatures. The uncertainty in these parameters is quite large and we hardly see any pressure dependence. The left side of the final row shows the best-fit values for the atomic positions. The average values are $y_{Ag} = 0.399(1)$ and $y_{Cl} = 0.123(3)$. There is no pressure dependence in these values which suggests that this structure is stable in this pressure region. The right side of the final row shows the unit cell parameters. The closed symbols represent the diffraction[1] results. I have shifted their results by -3 GPa for better comparison with our results which is due to the difference in temperature (see Sec. 6.4). The best-fit values for the unit cell dimensions agree well with the diffraction[1] results.

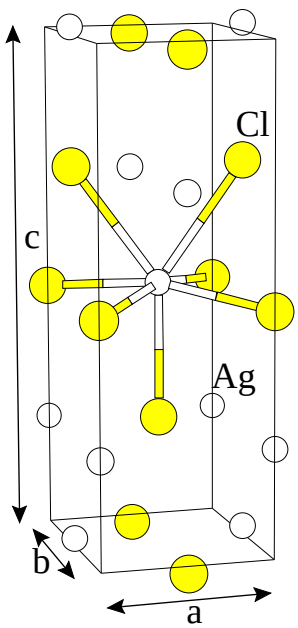

Structure Type	TlI
Space Group	Cmcm
Unit Cell Parameters (Å)	a = 3.38(3) b = 9.84(7) c = 4.11(3)
Atomic Positions	Ag:(0, 0.399(2), 0.25) (0, 0.601, 0.75) (0.5, 0.899, 0.25) (0.5, 0.101, 0.75) Cl:(0, 0.132(3), 0.25) (0, 0.868, 0.75) (0.5, 0.632, 0.25) (0.5, 0.368, 0.75)

Figure 6.17: A diagram of the final model for HPPII of AgCl based on the best-fit to the XAFS data. Left panel: A diagram of the HPPII of AgCl. The bonds connect the first shell of atoms, which includes seven Cl atoms, to the central Ag atom. Right panel: The crystal structure parameters including the best-fit values for the unit cell dimensions and the fractional position of the Ag and Cl atoms within the unit cell. I have shifted the TlI-type unit cell relative to the atomic positions listed in the table by a vector, $(0.50\hat{x}, 0.101\hat{y}, 0.25\hat{z})$, to place a Ag atom at the center of the unit cell.

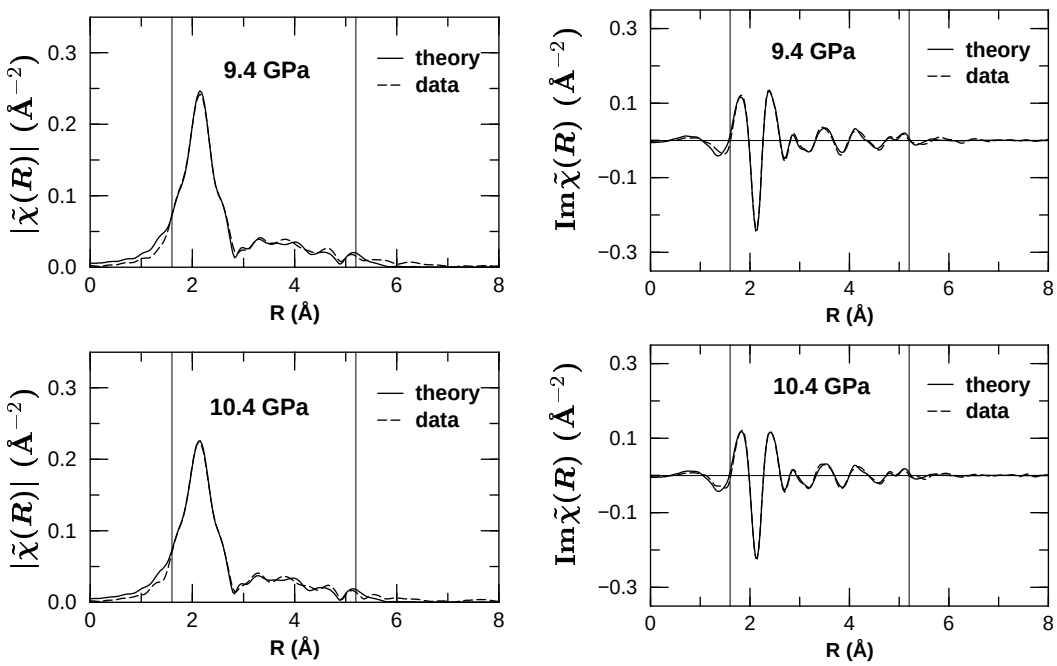

Figure 6.18: Data and the best-fit theoretical model for HPPII of AgCl. Left side: $|\tilde{\chi}(R)|$ data and theoretical model. Right side: Im$\tilde{\chi}(R)$ data and theoretical model. The vertical lines represent the fit range. The Fourier transform parameters are listed in Table 6.1.

For completeness I have listed the θ_{Ag1} and θ_{Cl1} and their corresponding values for σ_i^2 as a function of pressure in Table 6.6.

6.6 Discussion

The next step is to represent the HPPII, TlI-type, structure in terms of the HPPI, KOH-type, structure. Strictly, this does not have to be possible due to the restrictions on the placement of the atoms within the KOH-type unit cell. To demonstrate this restriction, consider Fig. 6.20 which shows the unit cell for the TlI structure as determined from the best-fit to the XAFS data at 9(1) GPa. By definition the KOH-like unit cell must contain 2 Ag and 2 Cl atoms. I have, therefore, outlined a possible unit cell shown by the Cl bonds in the figure. The accompanying table lists the parameters necessary to reproduce these unit cells. As shown in the table the actual space group needed to reproduce the KOH-like unit cell is not P 2_1 but the more primitive P 1

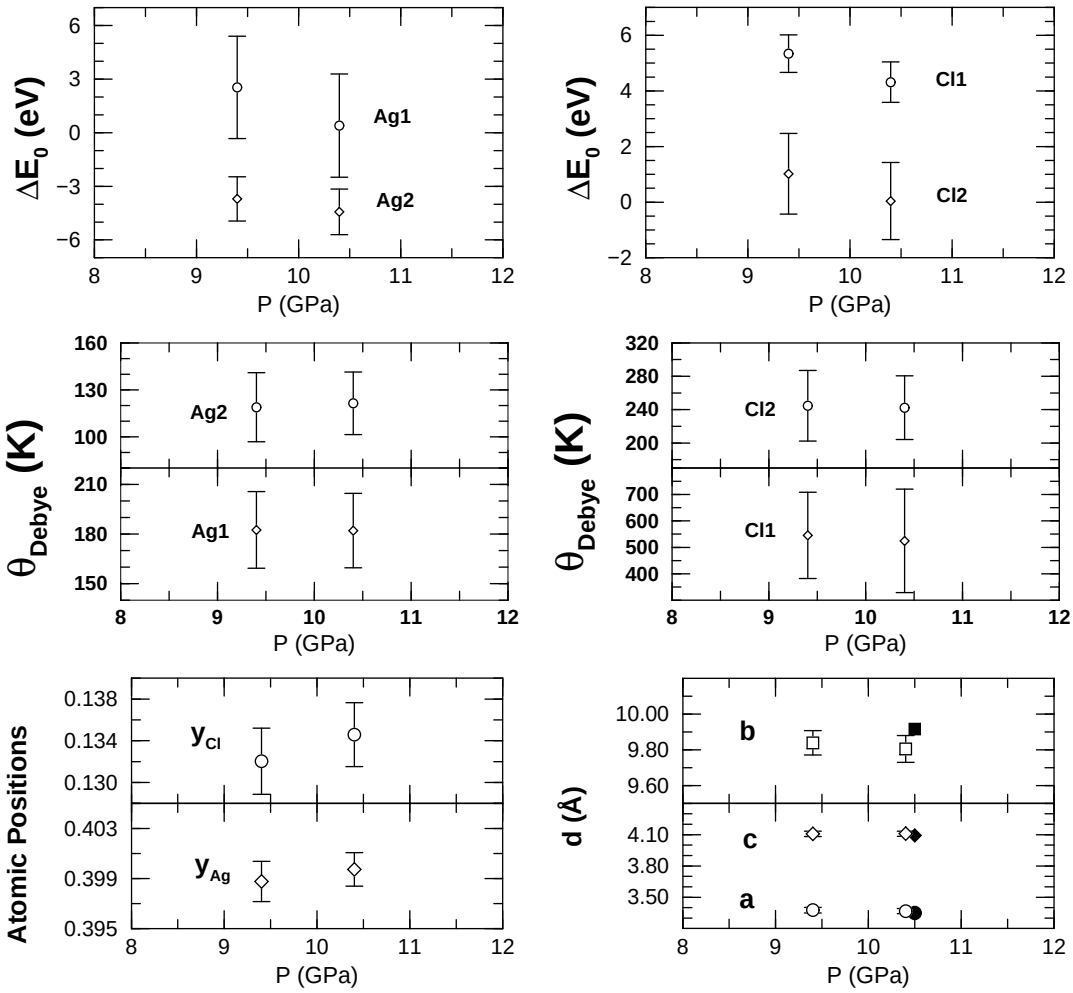

Figure 6.19: Best-fit values for HPPII of AgCl. Left side: the results for Ag→Ag paths. Right side: the results for Ag→Cl paths. The bottom row shows our results for the unit cell dimensions with the open symbols at 150K and the diffraction results with the closed symbols at 293K. I have shifted the diffraction results by -3 GPa for a better comparison with our results. There is a total of 13 parameters and 22 independent points in the fit and data range.

Table 6.6: List of σ_i^2 and the corresponding θ_{Debye} for the TlI-type of AgCl

Pressure (GPa)	θ_{Cl1} (K)	σ_1^2 (Å^2)	θ_{Ag1} (K)	σ_4^2 (Å^2)
9.4	545(163)	0.003(1)	183(23)	0.008(2)
10.4	525(196)	0.003(2)	182(22)	0.008(2)

structure where each of the 4 atoms within the unit cell must be specified. The KOH-type unit cell needs to be represented in terms of a single Ag atom at Ag1:(x_{Ag}, y_{Ag}, z_{Ag}) where the second Ag atoms is found at Ag2:($x_{\bar{Ag}}$, y_{Ag}+0.5, $z_{\bar{Ag}}$) and similarly for the two Cl atoms. I can move the unit cell to satisfy the condition for the Ag atoms by adding the vector (-0.1012$\hat{x}$, 0.25$\hat{y}$, -0.2024$\hat{z}$) to the unit cell. The result for the new atomic positions for both the Ag and Cl atoms are listed in Table 6.6. Using these fractional distances the first Ag1 placement is now equivalent to the Ag2 placement as needed for the KOH-type space group and luckily the Cl1 placement is equivalent to Cl2 therefore this structure belongs KOH-type space group. Again, I can only add one vector to the unit cell so one pair of atoms satisfy the KOH-type space group. It is fortunate that the other pair also align themselves otherwise this structure would not belong to the KOH-type space group.

Table 6.7: A list of equivalent atomic positions for HPPII of AgCl. The first column is the same as in Fig. 6.20 which goes with the unit cell as shown in that figure. If I shift the unit cell by (-0.101$\hat{x}$, 0.25$\hat{y}$, -0.205$\hat{z}$) so that the two Ag atoms within the unit cell are given by Ag1:(x_{Ag}, y_{Ag}, z_{Ag}) and Ag2:($x_{\bar{Ag}}$, y_{Ag}+0.5, $z_{\bar{Ag}}$) as needed for the KOH space group the result is listed in the left most column of this table. With this shift of the unit cell the two Cl atoms are given by a similar relation Cl1:(x_{Cl}, y_{Cl}, z_{Cl}) and Cl2:($x_{\bar{Cl}}$, y_{Cl}+0.5, $z_{\bar{Cl}}$) so that it is possible to represent this structure in terms of the KOH-type space group.

Structure Type	KOH-like	KOH
Space Group	P 1	P 2_1
Unit Cell	a = 3.38(3)	a = 3.38(3)
Parameters	b = 4.11(3)	b = 4.11(3)
(Å)	c = 5.20(3)	c = 5.20(3)
	β = 109(1)°	β = 109(1)°
Atomic Positions	Ag1:(0.899, 0.75, 0.798)	Ag:(0.101, 0.25, 0.202)
	Ag2:(0.101, 0.25, 0.202)	(0.899, 0.75, 0.798)
	Cl1:(0.632, 0.25, 0.264)	Cl:(0.732, 0.25, 0.267)
	Cl2:(0.368, 0.75, 0.736)	(0.368, 0.75, 0.736)

To illustrate the usefulness of the "topological" relationship I show the parameters for the KOH-type unit cell for all three phases of AgCl in Fig. 6.21 and the corresponding diagram for these structures in Fig. 6.22. As shown in Fig. 6.21 the Ag and Cl atomic positions are constant within each of these phases. Also the angle

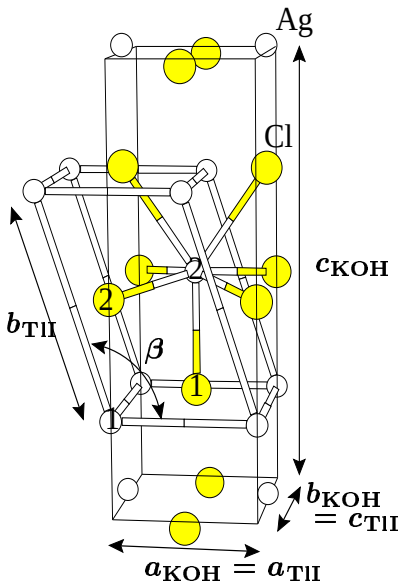

Structure Type	KOH-like	TlI
Space Group	P 1	Cm3m
Unit Cell Parameters (Å)	a = 3.38(3) b = 4.11(3) c = 5.20(3) β = 108.94(1)°	a = 3.38(3) b = 9.84(7) c = 4.11(3)
Atomic Positions	Ag1:(0, 0, 0) Ag2:(0.202, 0.5, 0.405) Cl1:(0.733, 0, 0.466) Cl2:(0.469, 0.5, 0.938)	Ag:(0, 0.399(2), 0.25) (0, 0.601, 0.75) (0.5, 0.899, 0.25) (0.5, 0.101, 0.75) Cl:(0, 0.132(3), 0.25) (0, 0.868, 0.75) (0.5, 0.632, 0.25) (0.5, 0.368, 0.75)

Figure 6.20: A diagram of the best-fit model the HPPII of AgCl in terms of the KOH and TlI space groups. The bonds connect the first shell of atoms to the central Ag atom which includes seven Cl atoms. The atomic positions for the KOH space group are not allowed (see the text). From the geometry of these space groups the KOH parameters are related to the TlI parameters as: $\tan(\beta) = a_{\mathrm{TlI}}/b_{\mathrm{TlI}}$ and $b_{\mathrm{TlI}} = 2c_{\mathrm{KOH}}\cdot\sin(\beta)$. I have shifted the TlI-type unit cell relative to the atomic positions listed in the table by a vector, $(0.50\hat{x},\ 0.101\hat{y},\ 0.25\hat{z})$, to place a Ag atom at the center of the unit cell.

β does not show any pressure dependence within the KOH-type and TlI-type phases. The lack of a pressure dependence in the atomic positions and the angle β is strong evidence that the KOH-type and TlI-type phases are stable crystal structures just as the B1 and B2 phases are. Our results for the unit cell dimensions along with the diffraction results are shown in the bottom row with the open and closed symbols respectively. The room temperature diffraction results have been shifted by -3 GPa (see Sec. 6.4) for better comparison with our results at 150K.

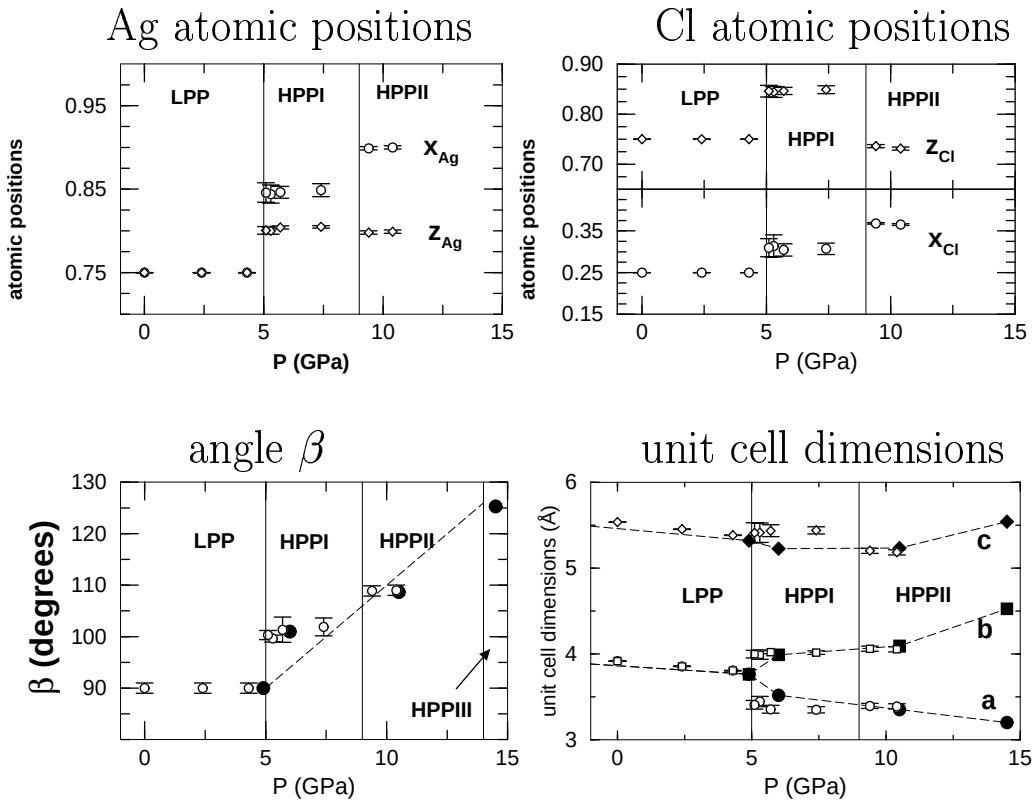

Figure 6.21: KOH-type parameters for all phases of AgCl. The solid vertical lines separate the data from different phases. The crystal structure of each phase is pressure independent which indicates that the structure is stable in this range. We did not find a gradual change of the angle β as we might expect indicated by the line in the lower left graph. Instead the angle changes quickly in the region between the different phases and is then stable until the next phase transition. The unit cell parameters from our best-fit and from the diffraction study are shown as the open and closed symbols respectively. We have shifted their room temperature results by -3 GPa (see Sec. 6.4) for comparison with our results at 150 K.

As a final check I calculate the volume per chemical formula as a function of pressure. The results are shown in Fig. 6.23 and illustrates that the overall volume is decreasing as the pressure is increased.

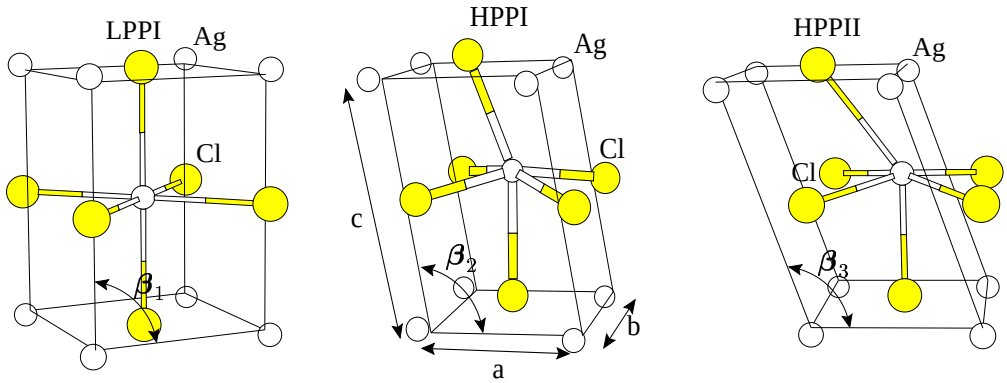

Figure 6.22: KOH-type unit cell for each phase of AgCl. Left: The KOH-type unit cell for LPPI. Middle: The KOH-type unit cell for HPPI. Right the KOH-type unit cell for HPPII. The parameters for these structures are shown in Fig. 6.21.

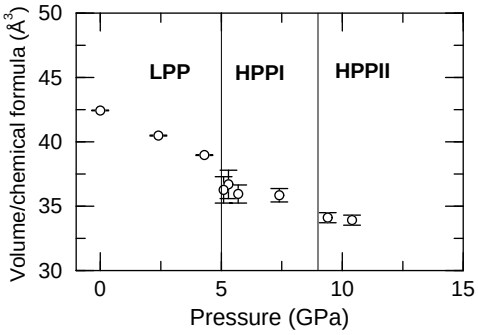

Figure 6.23: Volume per chemical formula as a function of pressure for AgCl.

Starting Model based on assumed atomic positions

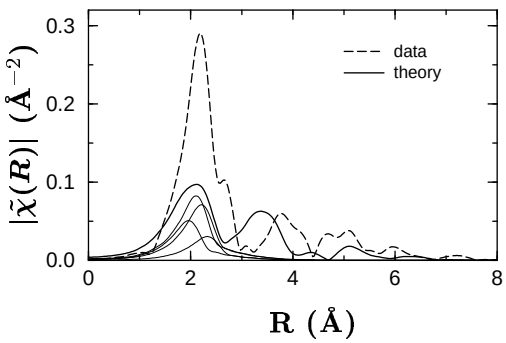

atom type	R_{ref} (Å)	N_i
$Ag_c \rightarrow Cl_1$	2.472	1
$Ag_c \rightarrow Cl_2$	2.622	2
$Ag_c \rightarrow Cl_3$	2.730	2
$Ag_c \rightarrow Cl_4$	2.846	1

Final Model based on best-fit to XAFS data

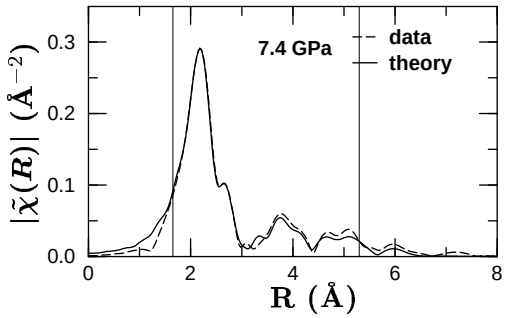

atom type	R_{ref} (Å)	N_i
$Ag_c \rightarrow Cl_1$	2.652	2
$Ag_c \rightarrow Cl_2$	2.659	2
$Ag_c \rightarrow Cl_3$	2.756	1
$Ag_c \rightarrow Cl_4$	2.770	1

Figure 6.24: A comparison of the structures based on the starting and final models for HPPI of AgCl. Top: A comparison of the data and model for the structure based on the unit cell dimensions determined from diffraction measurements[1]. The atomic positions were not determined therefore they were assumed to be the same as the KOH structure. Left side lists the first four shells, their degeneracy and radial distance. Bottom: A comparison of the data and model for the structure based on the unit cell dimensions determined from diffraction measurements[1]. The atomic positions were determined by the best-fit to the XAFS data. Left side lists the first four shells, their degeneracy and radial distance. Both of these models are consistent with the diffraction measurements for the long range structure but only the final model is consistent with the XAFS measurements for the local structure.

Starting Model based on assumed atomic positions

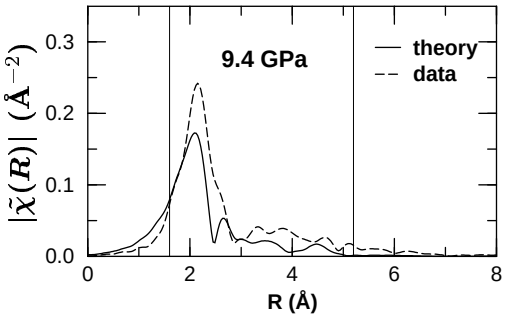

atom type	R_{ref} (Å)	N_i
$Ag_0 \rightarrow Cl_1$	2.506	1
$Ag_0 \rightarrow Cl_2$	2.647	4
$Ag_0 \rightarrow Cl_3$	2.966	2

Final Model based on best-fit to XAFS data

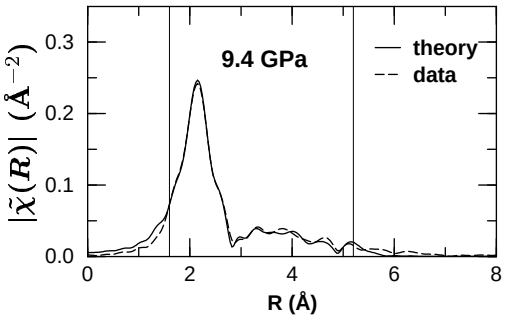

atom type	R_{ref} (Å)	N_i
$Ag_c \rightarrow Cl_1$	2.624	1
$Ag_c \rightarrow Cl_2$	2.676	4
$Ag_c \rightarrow Cl_3$	2.849	2

Figure 6.25: A comparison of the structures based on the starting and final models for HPPI of AgCl. Top: A comparison of the data and model for the structure based on the unit cell dimensions determined from diffraction measurements[1]. The atomic positions were not determined therefore they were assumed to be the same as the KOH structure. Left side lists the first four shells, their degeneracy and radial distance. Bottom: A comparison of the data and model for the structure based on the unit cell dimensions determined from diffraction measurements[1]. The atomic positions were determined by the best-fit to the XAFS data. Left side lists the first four shells, their degeneracy and radial distance. Both of these models are consistent with the diffraction measurements for the long range structure but only the final model is consistent with the XAFS measurements for the local structure.

6.7 Conclusions

I have determined the local structures of the high pressure phases of AgCl which are different than previously assumed in the diffraction study[1]. The assumed placement of the atoms within the unit cell for the KOH-type phase of AgCl are the same as for actual KOH and are Ag:(0.175, 0.25, 0.288) and Cl:(0.318, 0.25, 0.770). The positions that are consistent with the XAFS data are Ag:(0.156(11), 0.25, 0.200(4)) and Cl:(0.314(28), 0.25, 0.722(7)). The local structure as predicted by these atomic positions is quite dramatically different as shown in Fig. 6.24. The left side of this figures lists the shells which correspond to the first peak. As listed the radial distances as determined from the best-fit to the XAFS data are much more similar which gives the first large peak in the data. Similarly, the assumed atomic positions for the TlI-type phase of AgCl are the same as for actual TlI and are: Ag:(0,0.386,0.25) and Cl:(0,0.133,0.25). The positions that are consistent with the XAFS data are Ag:(0,0.399(2),0.25) and Cl:(0,0.132(3),0.25). Here the best-fit y_{Cl} value is consistent with the previously assumed value, and only a modest change has been made to the y_{Ag} value. This illustrates the sensitivity of XAFS to these positions by the relatively large differences shown in the theoretical models which are shown in Fig. 6.25 along with the shell distances which correspond to the first peak in the data.

I found that the TlI-phase of AgCl can be expressed in terms of a KOH-type structure which is consistent with the topological phase transition mechanism. The KOH-type unit cell for each AgCl phase is shown in Fig. 6.22 However for a given phase the crystal structure appears to be stable i.e. not changing gradually. This is not consistent with the pressure dependence of the topological phase transition as predicted in the diffraction study[1]. Fig. 6.22 shows the KOH-type unit cell for each of the phases: LPPI, HPPI and, HPPII. The pressure dependence of the KOH-type parameters are shown in Fig. 6.21. As discussed in Sec. 6.6 during both HPPI and HPPII the atomic positions and the angle β are constant indicating that these crystal structures are stable over a pressure range of several GPa. Most notably, β jumps quickly from 90° at 4.3 GPa in the B1-phase to 101° at 5 GPa in the KOH-phase and remains constant until 8 GPa in the KOH-type phase. This is not consistent with the pressure dependence of the phase transition mechanism as described in Ref. [1] which predicted a gradually increasing β as indicated by the dashed line in this figure. The XAFS results indicate that the topological relationship still holds but the pressure dependence of β is step-like.

The final question is: What is the crystal structure in between the transitions for each phase? Does the angle β gradually increase in the narrow pressure range of 0.7 GPa between the B1-phase at 4.3 GPa and the KOH-type phase at 5 GPa or is the crystal structure a mixture of the B1-phase and the KOH-type phase in this transition region? Unfortunately this XAFS data does not give the answer but some clue is found in the case of AgBr and is discussed in the next chapter.

Chapter 7

LOCAL STRUCTURE OF AgBr UNDER PRESSURE

The AgBr data was taken at 150K and at ambient pressure, 1.3(3), 3.0(5), 3.3(5), 4.9(5), 7.8(11), and 11.4(18) GPa. Experimental details can be found in Chapter 3. The pressure was determined from the XAFS data of Nb as discussed in Chapter 4. This chapter is an extension of the previous AgCl chapter. First, the B1-phase of AgBr is discussed. Then, the results for the atomic positions within the unit cell of HPPI for AgCl are applied to the high pressure phase of AgBr.

7.1 A First Look at the Data

The $|\tilde{\chi}(R)|$-data for AgBr is shown in Fig. 7.1. The left panel shows the data for the B1-phase. The peaks due to the first three shells of atoms are labeled as listed in Table 7.1 with their degeneracy and reference distance. A sketch of the B1 structure is shown for AgCl in Fig. 6.5. The right panel of Fig. 7.1 shows the data for the HPPI phase of AgBr. The arrow at about 3.5 Å shows some indication that the data at 4.9 GPa may not have the same structure as the other two data at 7.8 and 11.4 GPa.

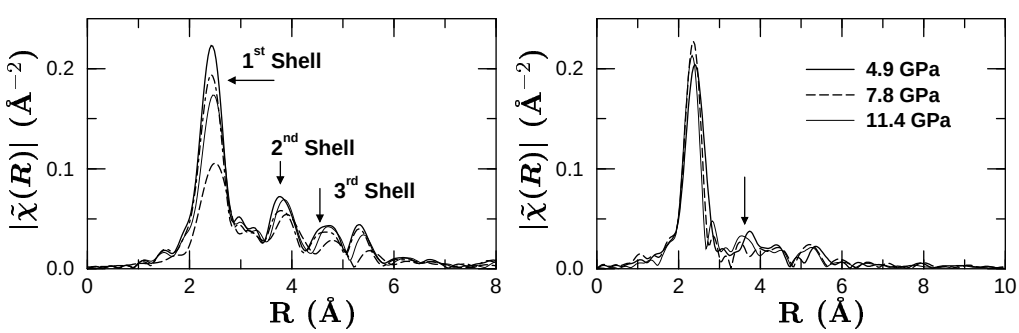

Figure 7.1: Pressure dependence of $|\tilde{\chi}(R)|$ for AgBr. Left panel: $|\tilde{\chi}(R)|$-data for the B1-phase of AgBr. The first shell peak increases in height as the pressure is increased. The corresponding data was taken at ambient pressure, 1.4, 3.0 and 3.3 GPa. Right panel: $|\tilde{\chi}(R)|$-data for HPPI of AgBr. The arrow at 4.5Å shows that the data at 4.9 GPa is somewhat different from the other two data.

Table 7.1: The first three shells for the B1-phase of AgBr about a Ag atom. The unit cell parameter $a = 5.7745$ at ambient pressure and room temperature[45] was used to determine the radial distances R_{ref}. The degeneracy of each shell is also listed, N_i. The contribution to the $|\tilde{\chi}(R)|$-data for each shell is labeled in Fig. 7.1

atom type	R_{ref} (Å)	N_i
$Ag_c \rightarrow Br_1$	2.887	6
$Ag_c \rightarrow Ag_2$	4.083	12
$Ag_c \rightarrow Br_3$	5.001	8

7.2 B1-Phase of AgBr

In the previous section the $|\tilde{\chi}(R)|$-data for the B1-phase of AgCl at ambient pressure, 1.4, 3.0 and 3.3 ± 0.5 GPa was discussed as shown in Fig. 7.1. Table 7.2 lists the data and fit ranges along with the Fourier transform parameters used to generate these data. The fit range includes all the atoms within the unit cell as listed in Table 7.1 along with their degeneracy and half path lengths at ambient pressure. The model-$|\tilde{\chi}(R)|$ was fitted to each of these data sets with k-weightings 1, and 2 simultaneously (see Sec. 4.4).

Table 7.2: Fourier transform parameters along with the fit and data ranges for each phase of AgBr. See Sec. 2.2.2 for detailed description of these parameters. The $\chi(k)$-data was multiplied by a Hanning window with full width of the sills given by the listed value for dk and a k^w where the value of w, called the k-weighting, is also listed.

Phase	R-range (Å)	k-range (Å^{-1})	Window type	dk(Å^{-1})	k-weighting
LPP	[1.7:5.2]	[3.55:12.10]	Hanning	2.0	1 and 2
HPPI	[1.7:4.8]	[2.8:13]	Hanning	2.0	1

7.2.1 Alignment and Background Removal

The background was removed according to the standard procedure described in Sec. 2.2.1. Here I will state the important parameters used in this procedure and show an example of the results. After normalization E_0 was set to the energy value corre-

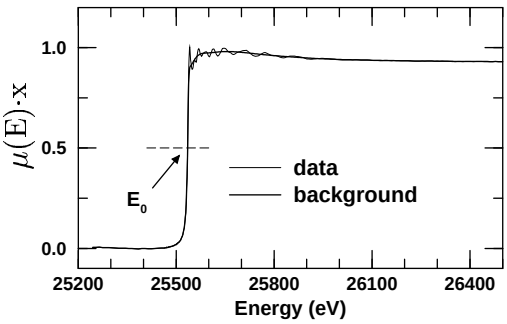

Figure 7.2: Example of the μ(E)·x-data and background function for AgBr. This data was taken at ambient pressure. The background function is a spline with 15 knots. E_0 = 25535 eV, chosen at about the middle of the step height.

sponding to 50% of the step height at 25535 ± 1 eV in the normalized and aligned data. The background function μ_0(E)·x was constructed using R_{bkg} = 1.5 Å which corresponds to a spline with 15 knots, as indicated by Eq. 2.31. An example of the μ(E)·x-data and background is shown in Fig. 7.2.

7.2.2 XAFS Parameters and Meaningful Parameters

The XAFS parameters needed in the fit of the theoretical model to the data at each pressure are S_0^2, σ_i^2, $\Delta E_0{}^i$ and Δr_i giving a total of 10 parameters. The index i indicates that each of the three paths has its own value. Sec. 2.2.4 describes these parameters and their relation to the XAFS equation. Because of the cubic symmetry of the B1-phase structure each half-path length is expected to compress by the same factor as the pressure is increased therefore $\Delta r_i = -\epsilon_p \cdot r_{reff_i}$ where r_{reff_i} is the initial reference half-path length and ϵ_p is the fractional compression as defined by Eq. 4.1. Using this relation the three Δr_i parameters are reduced to the one fractional compression, ϵ_p. Another change of variables was made through the Debye model where a single θ_{Debye} determines σ_i^2 of different shells where the atom pairs are the same. A discussion of the Debye model can be found in Sec. 4.3. The first and third paths both contain Ag→Br pairs therefore a single θ_{debye}^{Br} was used, whereas the second path containing Ag→Ag pairs was given its own θ_{debye}^{Ag}. Each path needed its own $\Delta E_0{}^i$ due to charge transfer as I discuss in Sec. 2.2.3. This model was implemented on a trail basis and

the goodness-of-fit was compared with and without these constraints. Only when the constraints did not decrease the goodness-of-fit were they used (see Sec. 2.2.4). Through the use of these constraints the number of varied parameters is reduced from 10 to 7. The final parameters varied in the fit are: S_0^2, $\Delta E_0{}^i$, ϵ_p, $\theta_{\rm debye}^{\rm Ag}$ and, $\theta_{\rm debye}^{\rm Br}$.

7.2.3 Determination of S_0^2

As described in Sec. 4.4 the method for determining S_0^2 is to simultaneously fit data at each pressure with k-weightings of $w = 1$, 2 and 3. The Fourier transform parameters and the fit and data ranges are listed in Table 7.2. This fit range includes 18 independent points per data set as given by Eq. 2.40. The number of parameters determined by the fit, as described above, was 6 for each pressure plus the one S_0^2 value. The best-fit value for $S_0^2 = 1.01 \pm 0.02$. This value for S_0^2 will be used for all the phases of AgBr as it only depends on the central atom as I discussed in Sec. 2.1.2.

7.2.4 Pressure Dependences for the B1-Phase of AgBr

With $S_0^2 = 1.01 \pm 0.02$ the theoretical model was fitted to the data for each pressure with 6 varied parameters. The best-fit values are listed in Table 7.3 along with the measures of the goodness-of-fit. An example of the data and the theoretical model at 1.4(5) GPa are shown in Fig. 7.3.

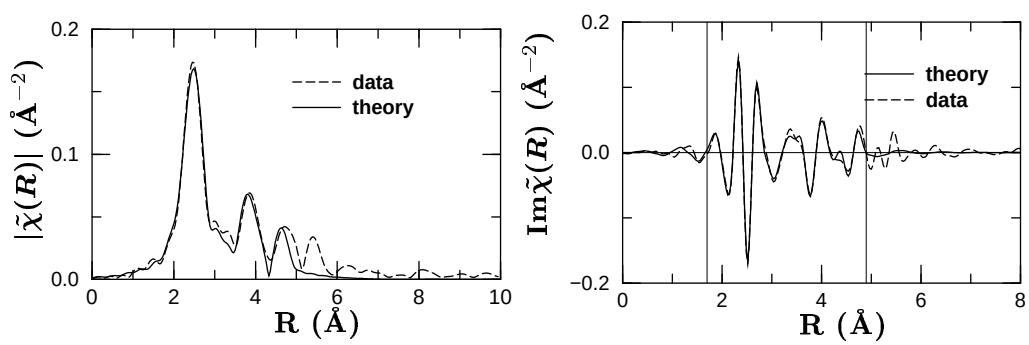

Figure 7.3: Comparison of the data and the best-fit theoretical model for the B1-phase of AgBr. The left panel and right panels show the $|\tilde{\chi}(R)|$ and Im$\tilde{\chi}(R)$ for the data and the theoretical fit result for the B1-phase of AgBr at 1.4(5) GPa and 150K. The fit range is indicated by the vertical lines. The Fourier transform parameters and data range are listed in Table 7.2.

The value for the lattice constant at ambient pressure and 150K was found to be $a = 5.737(16)$ Å. This value is within the measured uncertainty with the lattice

Table 7.3: The best-fit values for the B1-phase of AgBr. The pressure was determined from the Nb calibrant. The six parameters found in the fit are listed. They are an energy shift for each path, $\Delta E_0{}^i$, the fractional compression, ϵ_p, and two debye temperatures, θ^{Ag}_{debye} and θ^{Br}_{debye}. The goodness-of-fit parameters χ^2_ν and R-factor are also listed. The reference value used to determine ϵ_p is given by the ambient pressure and 150 K unit cell dimension $a = 5.737(8)$ Å. The data at 4.9 GPa will be discussed latter in this chapter.

P (GPa)	ϵ_p	θ^{Ag}_{debye} (K)	θ^{Br}_{debye} (K)	χ^2_ν	R-factor
0.0(3)	0.000(8)	137(3)	171(2)	133	1.2%
1.4(5)	0.016(5)	147(4)	207(2)	91	0.6%
3.0(5)	0.031(5)	139(4)	213(3)	92	0.7%
3.3(5)	0.028(5)	150(4)	232(3)	110	0.5%
4.9(5)	0.035(5)	84(12)	288(42)	78	0.5%

P (GPa)	$\Delta E_0{}^1$ (eV)	$\Delta E_0{}^2$ (eV)	$\Delta E_0{}^3$ (eV)
0.0(3)	1.1(7)	0.0(4)	3.5(11)
1.4(5)	2.9(6)	1.7(4)	5.4(9)
3.0(5)	2.9(6)	1.9(4)	6.8(9)
3.3(5)	3.0(6)	1.7(4)	6.2(10)
4.9(5)	-.3(20)	-1.6_s	2.4_s

constant $a = 5.751$ Å calculated from the room temperature value reported in Ref. [45] and using the thermal expansion coefficient from Ref. [52]. The values found for the energy shifts of each path, $\Delta E_0{}^i$, account for the misalignment of the data relative to the theory, as well as to compensate for phase shifts due to charge transfer. Changes in $\Delta E_0{}^i$ due to the misalignment of the data relative to the theory corresponds to the variation in $\Delta E_0{}^i$ for the same shell among the data taken at different pressures. As shown in the table this variation is within ± 1 eV which is consistent with our experimental resolution, indicating that the alignment of the data sets relative to each other and the theory is very good. The relative differences in $\Delta E_0{}^i$ for different shells are vary close to constant for each pressure point and is caused by the relative charge transfer between the atoms. Since Ag^+ has given up an electron and Br^- has gained an electron the photoelectron which is negative will be repelled from Br^-. This results in a negative phase shift of the photoelectron wave compared to a photoelectron which is traveling between neutral atoms as modeled in FEFF. This negative phase shift can be compensated for by an additional positive energy shift as indicated by Eq. 2.16 in Ref. [53]. Similarly an additional positive phase shift is add to the photoelectron that travels from $Ag^+ \rightarrow Ag^+$. This results in a additional negative energy shift. Therefore a comparison of the $\Delta E_0{}^1$ and $\Delta E_0{}^2$ which correspond to Ag→Br ($+\Delta E_0$) and Ag→Ag ($-\Delta E_0$) paths, respectively and we find that $\Delta E_0{}^1$ is on average 1.5(5) eV greater than $\Delta E_0{}^2$ as we expect from this simple picture. A comparison of $\Delta E_0{}^1$ and $\Delta E_0{}^3$ both of which correspond to Ag→Br paths and we find that $\Delta E_0{}^1$ is on average 3(1) eV greater than $\Delta E_0{}^3$. This is due to the model which FEFF uses for the atomic potentials as described in Sec. 2.2.3. Briefly, FEFF screens the core-hole atom which is the central Ag atom. For ionic materials this is a bad approximation which effects the first nearest neighbor potential. To correct the core-hole screening we need to give negative charge back to the first nearest Br atom which makes it more negative than the other Br atoms. Therefore the energy shift associated with $Ag \rightarrow Br_1$ is more positive than the energy shift associated with $Ag \rightarrow Br_3$. More information about energy shifts can be found in Ref. [54].

In general the expected pressure dependence for θ_{Debye} will be positive. This is equivalent to an increase in the stiffness of the bond between the atoms as the pressure is increased and the bond length decreases. A detail discussion on the Debye model and its pressure dependence can be found in Sec. 4.3. Comparing the best-fit values for θ_{Debye} we find that this trend is true for the Ag→Br paths, $\theta^{\mathrm{Br}}_{\mathrm{debye}}$, while there is

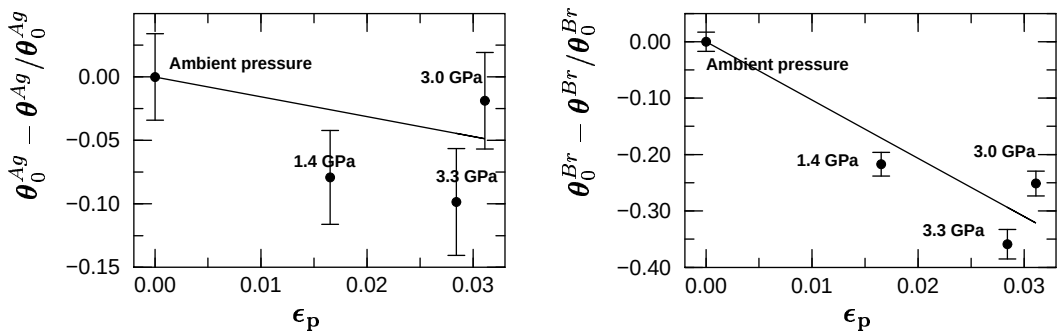

Figure 7.4: Example of the Grüneisen relationship for the B1-phase of AgBr. The solid line represents a least squares fit to the data points. ϵ_p is defined as the fractional compression, r - r_0/r. Left panel: The change in θ_{Debye} for the Ag→Ag paths. The slope of the line is -3γ where $\gamma = 0.52 \pm 0.41$ is the Grüneisen parameter. Right panel: The change in θ_{Debye} for the Ag→Ag paths. The slope of the line is -3γ where $\gamma = 3.4 \pm 0.5$ is the Grüneisen parameter.

not much change in the Ag→Ag path, $\theta^{\text{Ag}}_{\text{debye}}$. The relationship between the change in the bond length and the change in the stiffness of the bond is determined by the Grüneisen parameter, γ, defined in Eq. 4.2. Fig. 7.4 shows the fractional change in $\theta^{\text{Br}}_{\text{debye}}$ and $\theta^{\text{Ag}}_{\text{debye}}$ as a function of ϵ_p the fractional compression defined by Eq. 4.1. The reference values are taken from my ambient pressure results therefore the first point is by definition at the origin. The Grüneisen parameter for $\theta^{\text{Ag}}_{\text{debye}}$ is $\gamma = 0.52 \pm 0.41$ while the Grüneisen parameter for $\theta^{\text{Br}}_{\text{debye}}$ is $\gamma = 3.4 \pm 0.5$.

For completeness I have listed the $\theta^{\text{Ag}}_{\text{debye}}$ and $\theta^{\text{Br}}_{\text{debye}}$ and their corresponding values for σ_i^2 as a function of pressure in Table 7.4.

Table 7.4: List of σ_i^2 and the corresponding θ_{Debye} for the B1-phase of AgBr

P (GPa)	$\theta^{\text{Br}}_{\text{debye}}$ (K)	σ_1^2 (Å^2)	σ_3^2 (Å^2)	$\theta^{\text{Ag}}_{\text{debye}}$ (K)	σ_1^2 (Å^2)
0	170(2)	0.0103(2)	0.0137(3)	137(3)	0.0170(8)
1.4	207(2)	0.0072(2)	0.0096(2)	147(4)	0.0147(6)
3.0	213(3)	0.0069(2)	0.0091(2)	139(4)	0.0164(9)
3.3	232(3)	0.0059(2)	0.0078(2)	150(4)	0.0142(8)
4.9	492(521)	0.004(1)	0.017(15)	245(61)	0.043(12)

7.3 HPPI of AgBr

The data for the HPPI was taken at 7.8(11) and 11.4(18) GPa as determined by the Nb calibrant in a similar manor as for AgCl which is discussed in detail in Ch. 4.

Starting with the results from the HPPI of AgCl, I apply them to AgBr. As shown in the previous section the unit cell for the B1-phase of AgBr is about 4% larger than that of AgCl, therefore the unit cell parameters for AgCl were increased accordingly. Since several data points for the HPPI phase of AgCl indicated that the angle β was constant, its value, therefore, was set to 101°, decreasing the number of varied parameters. The values for the position of the atoms within the unit cell were originally fixed at the average values found for AgCl and the unit cell dimensions, a single θ_{Debye} and ΔE_0 for all Ag→Ag paths and another for all Ag→Br paths were determined by a fit to the data. Once a reasonable fit was found the four variable positions (x_{Ag}, z_{Ag}, x_{Br} and z_{Br}) for the placement of the atoms within the cell were also determined. These parameters are discussed in detail for AgCl in Sec. 6.4.2.

7.3.1 HPPI Model

The final result for the radial distribution function about a Ag atom at 7.8(11) GPa is shown in the right panel of Fig. 7.5. The fit range ΔR =[1.69:6.0] Å includes about 40 paths. Due to the large degree of splitting I found that all the paths with an amplitude greater than 5% of the first shell as determined by FEFF[56] contributed significantly to the model. As shown by the labels in the figure, I formed one Ag→Ag group and 2 Br→Br groups based on their distance from the central Ag atom. Several different constraints were placed on these groups. Once a reasonable fit was found by varying the unit cell parameters, the two Debye temperatures and the two energy shifts, the fit was refined by allowing each group to have its own θ_{Debye} and $\Delta E_0{}^i$. A table of the final varied parameters and their notation are shown in the right panel of Fig. 7.5.

A sketch of the HPPI structure is shown in Fig. 7.6 along with a table listing the unit cell parameters.

7.3.2 HPPI Results and Pressure Dependence

The data and the resulting theoretical model at each pressure are shown in Fig. 7.7. The best-fit values found for our varied parameters as described above are listed in

Table 7.5: The best-fit values for the HPPI of AgBr. The pressure was determined from the Nb calibrant. The 13 parameters found in the fit are listed. They are an energy shift for each path, $\Delta E_0{}^i$; the unit cell parameters a, b, and c; the atomic positions x_{Ag}, z_{Ag}, x_{Br}, and z_{Br}; and three Debye temperatures, θ_{debye}^{Ag1}, θ_{debye}^{Br1}, and θ_{debye}^{Br2}. The goodness-of-fit parameters χ_ν^2 and R-factor are also listed. The data at 4.9 GPa will be discussed later in this section.

P (GPa)	a (Å)	b (Å)	c (Å)	χ_ν^2	R-factor
4.9(5)	3.84(4)	3.87(4)	5.56(5)	78	0.5%
7.8(11)	3.73(3)	3.95(4)	5.42(6)	109	0.6%
11.4(18)	3.65(2)	4.01(3)	5.33(3)	40	0.3%

P (GPa)	x_{Ag}	z_{Ag}	x_{Br}	z_{Br}
4.9(5)	0.173(6)	0.200(1)	0.309(16)	0.741(6)
7.8(11)	0.146(5)	0.189(2)	0.326(60)	0.722(10)
11.4(18)	0.133(5)	0.184(3)	0.349(20)	0.730(4)

P (GPa)	θ_{debye}^{Br1} (K)	θ_{debye}^{Br2}(K)	θ_{debye}^{Ag1}(K)
4.9(5)	199(127)	492(521)	245(61)
7.8(11)	249(148)	38(4000)	184(21)
11.4(18)	284(73)	139(25)	163(14)

P (GPa)	$\Delta E_0{}^1$ (eV)	$\Delta E_0{}^2$ (eV)	$\Delta E_0{}^3$ (eV)
4.9(5)	2.9(13)	0.1_s	1.3_s
7.8(11)	3.3(10)	1.1(14)	0.7(17)
11.4(18)	2.6(9)	0.2(8)	3.0(17)

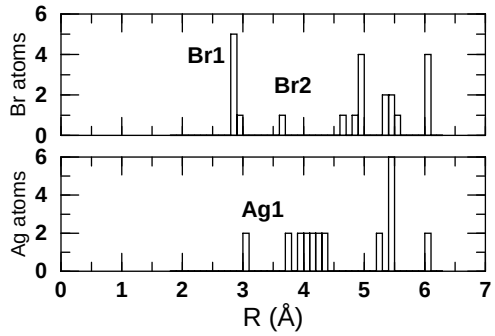

Group	θ_{Debye}	$\Delta E_0{}^{i}$
Br_1	θ_{Br1}	$\Delta E_0{}^{\mathrm{Br1}}$
Br_2	θ_{Br2}	$\Delta E_0{}^{\mathrm{Br2}}$
Ag_1	θ_{Ag1}	$\Delta E_0{}^{\mathrm{Ag1}}$

Figure 7.5: The radial distribution of atoms for HPPI of AgBr based on the best-fit to the XAFS data. Left panel: The radial distribution of Br, top, and Ag, bottom, atoms about a central Ag atom. Paths were grouped together depending on their distances as shown by the labels. Right panel: XAFS parameters for each group that were varied in the fit of the theoretical model to the data. The atomic subscripts indicate the shell index; all Br and Ag atoms sit in crystallographic-equivalent positions.

Table 7.5. There is a total of 13 varied parameters in the fit of the theoretical model to the data which contained about 29 independent points. The average measures of goodness-of-fit are $\mathcal{R} = 0.4\%$ and χ^2_ν =75. The uncertainties in the determined parameters are quite large due to the correlations between the four atomic position parameters and the three unit cell dimension parameters.

For completeness I have listed the $\theta^{\mathrm{Ag}}_{\mathrm{debye}}$ and $\theta^{\mathrm{Br1}}_{\mathrm{debye}}$ and their corresponding values for σ_i^2 as a function of pressure in Table 7.6.

Table 7.6: List of σ_i^2 and the corresponding θ_{Debye} for the KOH-type of AgBr

Pressure (GPa)	$\theta^{\mathrm{Br1}}_{\mathrm{debye}}$ (K)	σ_1^2 (Å^2)	σ_2^2 (Å^2)	σ_3^2 (Å^2)
4.9	199(127)	0.0075(110)	0.0076(112)	0.0078(114)
7.8	249(148)	0.0050(64)	0.0051(64)	0.0051(65)
11.4	284(73)	0.0039(20)	0.0040(20)	0.0041(19)

Pressure (GPa)	$\theta^{\mathrm{Ag1}}_{\mathrm{debye}}$ (K)	σ_5^2 (Å^2)
4.9	246(61)	0.0047(22)
7.8	184(21)	0.0079(18)
11.4	163(14)	0.0042(20)

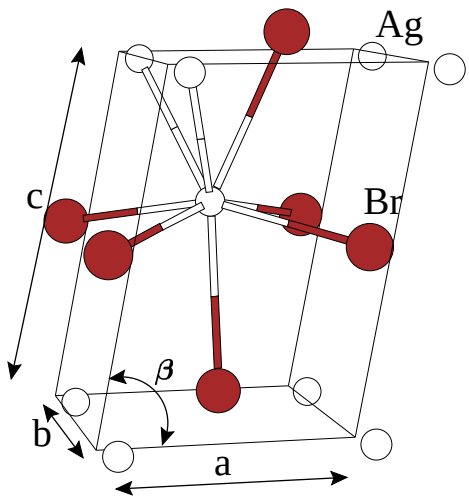

Structure Type	KOH
Space Group	$P2_1$
Unit Cell Parameters (Å)	a = 3.73(3) b = 3.95(4) c = 5.42(6) $\beta = 101°$
Atomic Positions	Ag: (0.146(5), 0.25, 0.189(2)) (0.854, 0.75, 0.811) Br:(0.326(59), 0.25, 0.722(10)) (0.674, 0.75, 0.278)

Figure 7.6: The structure of HPPI for AgBr based on the best-fit to the XAFS data. Top: A diagram of the HPPI of AgBr. The bonds connect the first shell of atoms to the central Ag atom which includes six Br atoms and two Ag atoms. Bottom: The crystal structure parameters including the best-fit values for the unit cell dimensions and the fractional position of the Ag and Br atoms within the unit cell. I have shifted the KOH-type unit cell relative to the atomic positions listed in the table by a vector, ($0.278\hat{x}$,$0.25\hat{y}$, $0.311\hat{z}$), to place a Ag atom at the center of the unit cell.

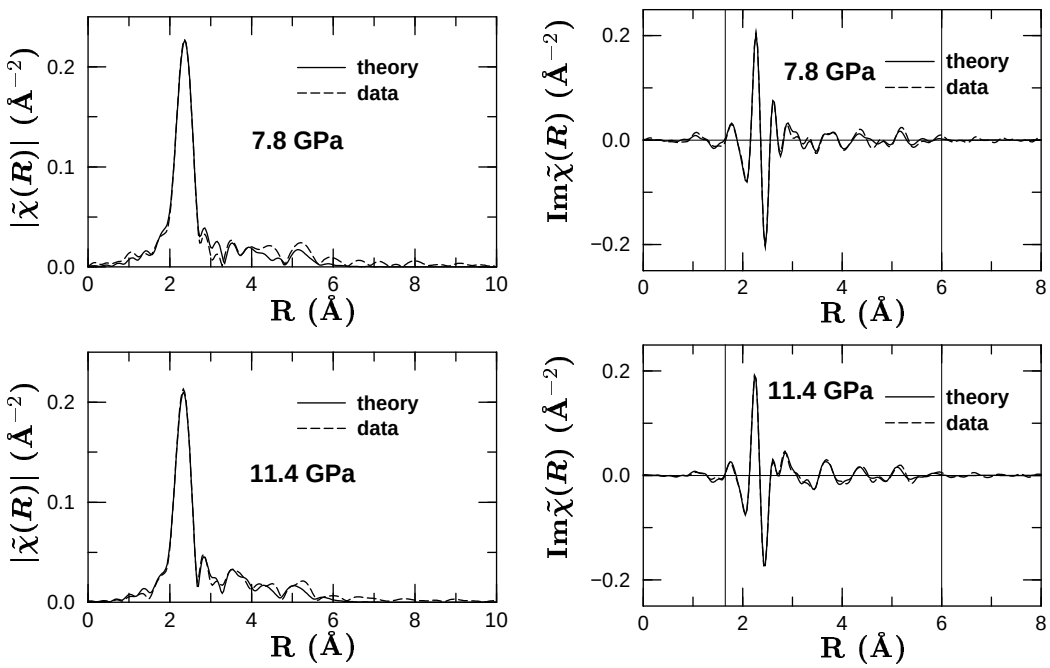

Figure 7.7: A comparison of the data and the theoretical model based on the best-fit to the XAFS data for HPPI of AgBr. Left side: $|\tilde{\chi}(R)|$-data and theory. Right side: Im$\tilde{\chi}(R)$-data and theory. The vertical lines represent the fit range. The Fourier transform parameters are listed in Table 7.2.

The model for HPPI does not described the data at 4.9 GPa. The angle β was allowed to vary, and despite many attempts the data particularly the peak at about 3.5 Å as shown in the Fig. 7.1 could not be reproduced. As a final attempt I tried a mixture of both HPPI structure and the B1 structure. As a starting point I used the parameters for the HPPI structure at 7.8 GPa and for the B1 structure at 3.3 GPa. This model was surprisingly successful at reproducing the data. The resulting $|\tilde{\chi}(R)|$-data and model are shown in Fig. 7.8. The best-fit parameters for HPPI structure and the B1 structure are listed in Table 7.5 and Table 7.1 along with the previous results. The mixing percent was found to be 44% HPPI phase.

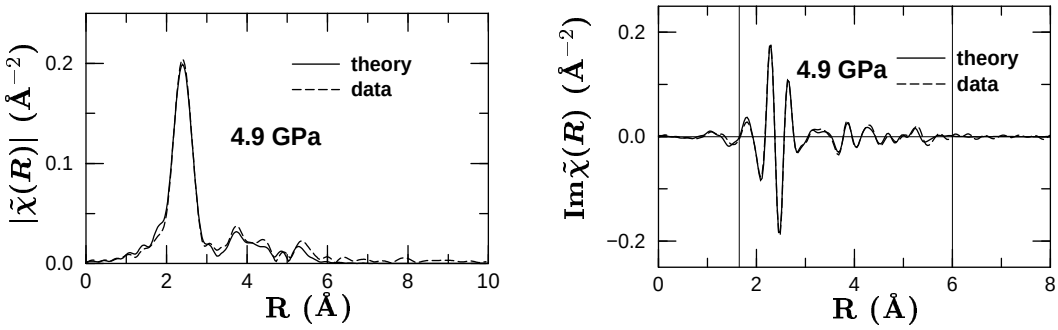

Figure 7.8: A comparison of the data and the theoretical model based on the best-fit to the XAFS data for mixture of HPPI and B1 phases of AgBr. Left side: $|\tilde{\chi}(R)|$-data and theory. Right side: Im$\tilde{\chi}(R)$-data and theory. The vertical lines represent the fit range. The Fourier transform parameters are listed in Table 7.2.

Fig. 7.9 shows the KOH-type parameters for both the B1 and HPPI structures of AgBr. As in AgCl the same splitting of the unit cell parameters a and b were found for HPPI. Fig. 7.10 shows the volume per chemical formula as a function of pressure and illustrates that the overall volume is decreasing as the pressure is increased.

7.4 Conclusions

I have determined the local structure for the KOH-type phase of AgBr, which is very similar to the structure for AgCl. I was also fortunate enough to have one data point between the B1-phase and the KOH-type phase that could not be described as either the B1-phase or the KOH-type phase alone. This data, also, could not be described with a KOH-type structure with an angle β between 90° and 101° as expected for a gradual pressure dependence of the topological transition mechanism.

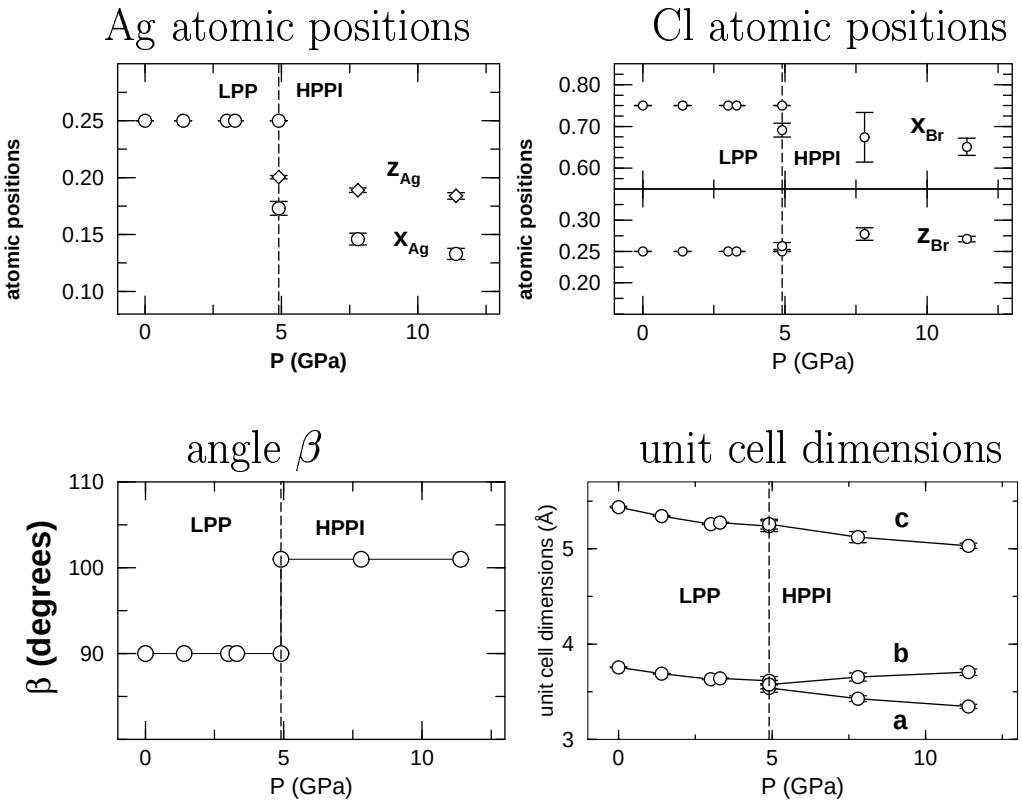

Figure 7.9: KOH-type parameters for all phases of AgBr. The solid vertical lines separate the data from different phases. The crystal structure of each phase is pressure independent which indicates that the structure is stable in this range.

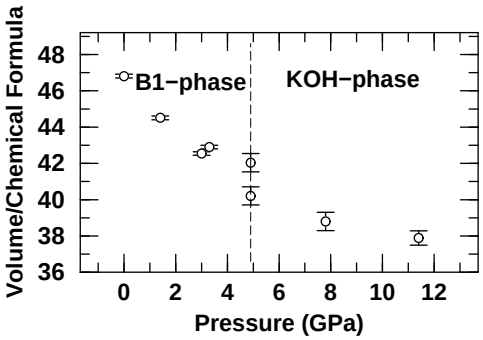

Figure 7.10: Volume per chemical formula as a function of pressure of AgBr.

The only reasonable fit to the data was found by allowing for a mixture of B1 and KOH-type phases. This is consistent with the martensitic-like mechanism as found for RbCl. Based on this evidence it seems likely that the transition between each phase of AgCl and AgBr is martensitic-like while the overall "topological" relationship between each phase exists. Another unfortunate but possible explanation for this mixture is pressure gradients. Unlike the RbCl transition which occurs at much lower pressure and where I have three data points consistent with a mixture of phases, for AgBr the transition pressure is about 10 times larger, in a regime known to produce pressure gradients, and I have only a single data point consistent with a mixture. Therefore it is difficult to be certain as to the transition mechanism between each phase of AgCl and AgBr.

Chapter 8

CONCLUSIONS

Based on my analysis of the transition region of RbCl, AgCl, and AgBr systems I found that the transition mechanism is quite different in the two systems. The transition mechanism for RbCl is consistent with a martensitic-like transition, whereas the transition mechanism for AgCl is more "topological". The next two paragraphs summarize my results for these systems.

For the RbCl system: From the fits of the theoretical model to the data at the transition I deduce the following properties of the phase transition. First the crystal structure for these data were found to be consistent with a mixture of phases and not with the intermediate KOH-type structure. Second, the phase transition requires an excess pressure at the onset of the transition of 0.2(1) GPa. Once the transition starts the system relaxes to a pressure of 0.5(1) GPa which remains approximately constant until the transition is complete. This is expected in martensitic-like transitions where the nucleation of the parent (B2) phase requires excess pressure. This also explains why the previously reported values for the transition pressure may be slightly low. Third, because the best-fit values for σ_i^2 and C_3^i of each shell in the single-phase regions were used to parameterize their pressure dependence and this pressure dependence was used in the model of the data at the transition, it follows from the success of these fits that the structural disorder is no larger at the phase transition than in the single-phase regions. From these results we conclude that the phase transition is consistent with a martensitic-like interpretation.

For the AgCl system: I have determined the local structure of two high pressure phases of AgCl which are different than previously assumed[1]. The first high pressure phase is a KOH-type structure and the second is a TlI-type structure. The "topological" relationship is based on the KOH-type structure which can be used to reproduce the structure of each phases of AgCl. Even though I found that the local structure of the TlI-type was different than previously assumed, I found that the TlI-type phase of AgCl can still be expressed in terms of a KOH-type structure which is consistent with the topological phase transition mechanism. This does not by definition to be

possible and is only true for special TlI-type structures.

The "topological" relationship between all the structural phases exist, but the transition mechanism is different than suggested in the diffraction study[1]. In the diffraction study it was proposed that the KOH-type and TlI-type phases would gradually distort connecting the B1 to the B2 phase. If this were the case the angle β of the equivalent KOH-type unit cell is expected to slowly increase from 90° →125° of the B1 and B2 phases respectively. Instead I found that the angle β increases in a step like manor from 90° →101° →110° →125° for the B1, KOH, TlI and B2 phases respectively. Furthermore, at the transition from the B1 to KOH-type phase, any change in the angle β must be occurring within a small pressure range of 0.7 GPa between 4.3 and 5.0 GPa which were found to be consistent with the B1-phase and KOH-type phase respectively.

For the AgBr system: I have determined the local structure for the KOH-type phase, which is very similar to the structure for AgCl. I also have one measurement of the crystal structure between the B1-phase and the KOH-type phase that could not be described as either the B1-phase or the KOH-type phase alone. This data, also, could not be described with a KOH-type structure with an angle β between 90° and 101° as expected for the gradual pressure dependence of the topological transition mechanism. The only reasonable fit to the data was found by allowing for a mixture of B1 and KOH-type phases. This is consistent with the martensitic-like mechanism as found for RbCl. Based on this evidence it seems likely that the transition between each phase of AgCl and AgBr is martensitic-like while the overall "topological" relationship between each phase exists. Another unfortunate but possible explanation for this mixture is pressure gradients. Unlike the RbCl transition which occurs at much lower pressure and where I have three data points consistent with a mixture of phases, for AgBr the transition pressure is about 10 times larger, in a regime known to produce pressure gradients, and I have only a single data point consistent with a mixture. Therefore it is difficult to be certain as to the transition mechanism between each phase of AgCl and AgBr.

BIBLIOGRAPHY

[1] K. Kusaba, Y. Syono, T. Kikegawa and O. Shimomura. A Topological Transition of B1-KOH-TlI-B2 Type AgCl Under High Pressure. *J. Phys. Chem. Solids.*, 56(5):751–757, May 1995.

[2] A. Onodera, S. Kawano, Y. Nakai, and N. Achiwa. Structural correspondence across the pressure-induced B1→B2 transition in RbCl. *Physica B*, 180&181:279–280, 1992.

[3] H. Fujiwara, N. Nakagiri, and M. Nomura. Orientation relation in the pressure-induced transition B1→B2 of RbCl Observed by an x-ray four-circle diffractometer. *J. Phys. Soc. Jpn.*, 52(5):1665–1668, May 1983.

[4] Bin Okai. Preferred orientation of B1-Type Rb and K Halides in the change B1→B2-type. *jpsjap*, 50(10):3189–3190, October 1981.

[5] A. V. Soldatov, T. S. Ivanchenko, I. E. Stekhin, A. Bianconi, and R. Ingalls. X-ray absorption fine structure investigation of the high pressure phase of KBr and RbCl. *Phys. Stat. Sol.*, 184:237–245, 1994.

[6] Carl W. F. T. Pistorius. Polymorphic transitions of the alkali chlorides at high pressures to 200°C. *jpcs*, 25:1477–1481, 1964.

[7] S. Vaidya and G. Kennedy. Compressibility of 27 halides to 45 Kbar. *J. Phys. Chem. Solids.*, 32:951–964, 1971.

[8] A. J. Darnell and W. A. McCollum. Thermodynamics of the Fm3m→Pm3m transition in the potassium and rubidum halides. *jpcs*, 31:805–815, 1970.

[9] J. Stohr. SEXAFS: Everything You Always Wanted to Know About SEXAFS but Were Afraid to Ask. In D.C. Koningsberger and R. Prins, editors, *X-Ray Absorption: Principles, Applications, Techniques of EXAFS, SEXAFS, and XANES*,

volume 92 of *Chemical Analysis*, chapter 10, pages 443–571. John Wiley and Sons, New York, 1988.

[10] A. B. Arons and M. B. Peppard. Einstein's proposal of the photon concept-a translation of the *Annael der Physik* paper of 1905. *American Journal of Physics*, 33(5):367–374, May 1965.

[11] W. C. Rontgen. On A New Kend of Rays. *American Journal of Physics*, 13:284–291, 1945.

[12] J.J. Rehr, R.C. Alber, C.R. Natoli, and E.A. Stern. New High–Energy Approximation for X–Ray–Absorption Near–Edge Structure. *Phys. Rev. B*, 34(6):4350–4353, 1986.

[13] E. A. Stern and S. M. Heald. Basic Principles and Applications of EXAFS. In E. E. Koch, editor, *Handbook of Synchrotron Radiation*, pages 995–1014, New York, 1983. North-Holland.

[14] E.A. Stern. Structural Determination by X-ray Absorption. *Comp. Phys. Comm.*, 19(4):289–310, 1978.

[15] P.A. Lee and J.B. Pendry. Theory of the Extended X-Ray Absorption Fine Structure. *Phys. Rev. B*, 11(8):2795–2811, 1975.

[16] C.A. Ashley and S. Doniach. Theory of extended x-ray absorption edge fine structure (EXAFS) in crystalline solids. *Phys. Rev. B*, 11(4):1279–1288, 1975.

[17] O. Keski-Rahkonen and M.O. Krause. Total and partial atomic-level widths. *Atomic Data and Nuclear Data Tables*, 14:139–146, 1974.

[18] J.J. Rehr, E.A. Stern, R.L. Martin and E.R. Davidson. Extended x-ray-absorption fine-structure – Wave-function relaxation and chemical effects. *Phys. Rev. B*, 17(2):560–565, January 1978.

[19] J. J. Rehr, R. C. Albers, and S. I. Zabinsky. High-order multiple-scattering calculations of x-ray-absorption fine structure. *Phys. Rev. Lett.*, 69(23):3397–3400, 1992.

[20] S. I. Zabinsky, J. J. Rehr, A. Ankudinov, R. C. Albers, and M. J. Eller. Multiple-Scattering Calculations of X-ray-Absorption Spectra. *Phys. Rev. B*, 52(4):2995–3009, 1995.

[21] J. J. Rehr and R. C. Albers. Scattering-Matrix Formulation of Curved-Wave Multiple-Scattering Theory: Application to X-ray-Absorption Fine Structure. *Phys. Rev. B*, 41(12):8139–8149, 1990.

[22] M. G. Kendall. *The Advanced Theory of Statistics*, volume 1. Charles Griffin & Co. Ltd., London, 1958.

[23] M. Newville, P. L¯iviņš, Y. Yacoby, J. J. Rehr, and E. A. Stern. Near-edge x-ray-absorption fine structure of Pb: A comparison of theory and experiment. *Phys. Rev. B*, 47(21):14126–14131, 1993.

[24] H. Wende, P. Srivastava, R. Chauvistré, F. May, K. Baberschke, D. Arvanitis, and J. J. Rehr. Evidence for Photoelectron Backscattering by Interstitial Charge Densities. *J. Phys.: Cond. Matt.*, 9:L427–L433, 1997.

[25] J. J. Rehr, C. H. Booth, F. Bridges, and S. I. Zabinsky. X-ray-absorption fine structure in embedded atoms. *Phys. Rev. B*, 49(17):12347–12350, 1994.

[26] W. H. McMaster, N. Kerr-Del Grande, J. H. Mallett, and J. H. Hubbell. *Compilation of X-ray Cross Sections. Lawrence Radiation Laboratory Report UCRL-50174*. National Bureau of Standards, Springfield, VA, 1969.

[27] M. Newville. FEFFIT: Using FEFF to model XAFS in R-space. unpublished, 1994. This documentation is part of the UWXAFS3.0 package.

[28] J. J. Rehr, J. Mustre de Leon, S. I. Zabinsky, and R. C. Albers. Theoretical X-ray Absorption Fine Structure Standards. *J. Am. Chem. Soc.*, 113(14):5135–5140, 1991.

[29] B.I. Lundqvist. Some Numerical Results on Quasiparticle Properties in the Electron Gas. *phys. stat. sol.*, 32:273–280, 1969.

[30] E.A. Stern. Number of Relevant Independent Points in X–Ray–Absorption Fine–Structure Specta. *Phys. Rev. B*, 48(13):9825, 1993.

[31] P. R. Bevington and D. K. Robinson. *Data Reduction and Error Analysis for the Physical Sciences.* McGraw-Hill, New York, 2nd edition, 1992.

[32] Neil W. Ashcroft and N. David Mermin. *Solid State Physics.* Holt, Rinehart and Winston, New York, 1976.

[33] S.M. Heald. EXAFS with Synchrotron Radiation. In D.C. Koningsberger and R. Prins, editors, *X-Ray Absorption: Principles, Applications, Techniques of EXAFS, SEXAFS, and XANES*, volume 92 of *Chemical Analysis*, chapter 4, pages 119–161. John Wiley and Sons, New York, 1988.

[34] E.A. Stern. Detectors for Laboratory EXAFS Facilities. In *AIP Conference Procedings*, number 64, New York, 1980. American Institute of Physics.

[35] E.A. Stern, W.T. Elam, B.A. Bunker and K. Lu. Ion Chambers for Fluorescence and Laboratory EXAFS Detection. *Nuc. Inst. Meth.*, 195:345–346, 1982.

[36] M. Newville. Compilation of X-Ray Cross Sections. Found on the World Wide Web at http://krazy.phys.washington.edu/Tools/Mcbook/, October 1995. Based on Ref [26].

[37] R. Ingalls, J.E. Whitmore, A.J. Seary, J.M. Tranquada. Extended x-ray absorption fine structure of NaBr and Ge at high pressure. *J. Appl. Phys.*, 51(6):3158–3163, June 1980.

[38] D.J. Dunstan. Theory of the gasket in diamond anvil high-pressure cells. *Rev. Sci. Instr.*, 60(12):3789–3795, 1989.

[39] W. B. Daniels and M. G. Ryschkewitsch. Simple double diaphragm press for diamond anvil cells at low temperature. *Rev. Sci. Instr.*, 54(1):115–116, 1983.

[40] F. Wang. *XAFS Study of Solid-Solid transitions Under High Pressure.* PhD thesis, University of Washington, 1998.

[41] M.E. Rose and M.M. Shapiro. Statistical Error in Absorption Experiments. *Phys. Rev.*, 74(12):1853–1864, 1948.

[42] K. Q. Lu and E. A. Stern. Size Effect of Powdered Sample on EXAFS Amplitude. *Nuc. Inst. Meth. Phys. Res.*, 212:475–478, 1983.

[43] E.A. Stern and K. Kim. Thickness Effect on the Extended-X-ray-Absorption-Fine-Structure Amplitude. *Phys. Rev. B*, 23(8):3781–3787, 1981.

[44] American Institute of Physics. *American Institute of Physics Handbook*. McGraw-Hill, 3rd edition, 1972.

[45] R.G.W. Wyckoff. *Crystal Structures*, volume 1–6. Interscience, New York, 1964.

[46] P.P. Lottici. Extended x-ray-absorption fine-structure Debye-Waller factors and vibrational density of states in amorphous arsenic. *Phys. Rev. B*, 35(3), 1236–1241 1987.

[47] G.S. Knapp, H.K. Pan, and J.M. Tranquada. Extended x-ray-absorpiton fine-structure Einstein frequency and moments of the phonon spectrum: An experimental and theoretical study. *Phys. Rev. B*, 32(4):2006–2009, 1985.

[48] M. Newville. Personal communication.

[49] G. K. White. The Heat Campacity of Transition Metals at High Temperatures. *Physica A*, 149:255–260, 1988.

[50] K. A. Gschneider, Jr. *Solid State Physics*, volume 16, chapter Physical Properties and Interrelationships of Metallic and Semimetallic Elements. Academic Press, 1964.

[51] A. Frenkel, E. Stern, M. Qian, and M. Newville. Mulitple-scattering x-ray-absorption fine-structure analysis and thermal expansion of alkali halides. *Phys. Rev. B*, 48(17):12449–12458, November 1993.

[52] Purdue University. Thermaophysical Properties Research Center. *Thermophysical properties of matter*. New York, IFI/Plenum, 1970.

[53] D. Haskel. *Local Structural Studies of Oriented High Temperature Superconducting Cuprates by Polarized XAFS Spectroscopy.* PhD thesis, University of Washington, 1998.

[54] D. Haskel, B. Ravel, M. Newville, and E.A. Stern. Single and multiple scattering XAFS in $BaZrO_3$: A comparison between theory and experiment. *Physica B*, 208&209:151–153, 1995.

[55] John A. Dean, editor. *Lange's Handbook of Chemistry.* McGraw-Hill, 11th edition, 1956. radii, 3-118.

[56] J.J. Rehr. *Ab initio Multiple Scattering X-ray Absorption Fine Structure and X-ray Absorption Near Edge Structure Code.* University of Washington, 1995. software documentation.

Appendix A

FITTING MODELS IN feffit

Models for XAFS data are based on a group of paths. The path is defined as starting from the excited atom and then to one or more neighboring atoms and then back to the excited atom. As discussed in Section 2.2.4 each path can have a total of seven parameters. The `feffit.inp` file is constructed so that each path has a paragraph containing three columns. The first column specifies a key word that represents a parameter for the path. The second column specifies a unique number for the path. The third column may be a mathematical expression or a number which will be used for the key word. The basic form of this paragraph is shown in Fig. A.1 and a list of the key words which correspond to the parameters described in Section 2.2.4 are shown in Table A.1.

Table A.1: Key words used in FEFFIT.

key word	symbol	description
path		The name of the `feffnnnn.dat` file for this path
id		A short description of the path.
s02	S_0^2	Passive electron reduction factor.
e0	ΔE_0	Shift in the reference photoelectron wave number.
delr	ΔR	Shift in the path length.
sigma2	σ^2	Relative mean square displacement about path length.
third	C_3	Third Cumulant about path length.
fourth	C_4	Fourth Cumulant about path length.
ei	E_i	Change in the effective mean free path of the photoelectron.

```
path    1       feff/feff0001.dat
id      1       amp=100.000, deg=2.000, nleg=2, r_eff=2.65, Ag-Cl-Ag
sigma2  1       debye(temp,tCl1_debye)
delr    1       r1 - reff
e0      1       eCl1
third   1       third1
fourth  1       fourth1

path    2       feff/feff0002.dat
id      2       amp=95.000, deg=2.000, nleg=2, r_eff=2.63, Ag-Cl-Ag
sigma2  2       debye(temp,tCl2_debye)
delr    2       r2 - reff
e0      2       eCl2
third   2       third2
fourth  2       fourth2
```

Figure A.1: Part of the `feffit.inp` file specifying the path paragraph for two shells. Each line contains a key word, path number and expression. Table A.1 gives a short description of each key word.

A.1 Nb Calibrant

Two of the most common constraints used in this thesis are illustrated within the Nb model. They are the amount of uniform compression and the Debye model. These change of parameters are listed in Table A.2, and are part of the `feffit.inp` file shown in Fig. A.2. More discussion on these constraints can be found in Sec. 4.3.

Table A.2: Change of parameters for Nb calibrant.

original parameter and shells	expression	final parameter
ΔR_i : $i = 1, 2$	ΔR_i = alpha· reff	alpha
σ_i^2 : $i = 1, 2$	σ_i^2 = Debye(Temp,θ_{Debye})	θ_{Debye}

A.2 RbCl

The model for RbCl evolved through several stages as discussed in Sec. 5.3. The first stage was to fit the data using a simple model similar to the one shown in the previous section for Nb. The second stage was to determine linear pressure dependencies of σ^2 and C_3. The final stage was to incorporate these linear pressure dependencies into the model for a mixture of both of the pure phases. The next two subsections outlines the model for the second and final stages.

A.2.1 B1-Phase and B2-Phase

The linear pressure dependencies are determined using this model. The model fits several data sets at different pressures to determine a slope and intercept value for a line which gives the parameters value at each corresponding pressure. For the B1-phase, three shells were included each with its own value for σ_i^2. I found that the pressure dependence of σ_i^2 depends approximately linearly on pressure and that the slope of the relationship is approximately the same for each shell. The 4 parameters: sig_slope, sig_int1, sig_int2 and sig_int3, therefore, determines σ_i^2 for each of the three shells for each of the 4 data sets each corresponding to a different pressure, i.e. I have reduced 12 parameters to 4. Sig_slope refers to the slope of the line connecting the value for σ^2 to the pressure, p, and sig_int1 refers to the intercept of this line for the

```
%==+==+==+
```

first shell. These change of parameters are listed in Table A.3 and are part of the `feffit.inp` file shown in Fig. A.3.

Table A.3: Change of parameters for the B1-phase of RbCl. The number of original parameters is multiplied by the number of data sets taken at different pressures. The constants A, B and C are determined from the known compressibility of RbCl (see Sec. 5.4.1).

original parameter and shells	expression	final parameter
ΔR_i : $i = 1, 2, 3$	ΔR_i = alpha· reff	p for each data
	alpha = A + B·p + C·p^2	
σ_i^2 : $i = 1, 2, 3$	σ_i^2 = Debye(Temp,θ_{Debye})	sig_slope, sig_int1,
	θ_{Debye} = sig_int$_i$ + sig_slope·p	sig_int2, sig_int3
C_3^i : $i = 3$	C_3^i = C3_int1 + C3_slope·p	C3_slope, C3_int1

A.2.2 Mixture of B1- and B2-Phases

The last stage is to use the slope and intercept values determined in the previous subsection to model the data as a mixture of both phases using a minimum of undetermined parameters. Table A.4 illustrates that the single parameter, the pressure, determines ΔR$_i$, σ_i^2 and C_3^i. The `feffit.inp` file is shown in several sections. The first section, Fig. A.4, shows the B1-phase parameters that were determined in the previous section and the expression for σ_i^2 and C$_3$ in terms of the pressure. The next section, Fig. A.5, shows the same expressions for the B2-phase and also lists the parameters determined by the fit indicated by the guess key word. The last two sections of the `feffit.inp` file, Figs. A.6 and A.7, lists the paths for the B1- and B2-phase, respectively.

A.3 AgCl and AgBr

The AgCl and AgBr models are the same, so only the AgCl `feffit.inp` are discussed in this section. The B1-phase of AgCl was modeled in a similar manor to the Nb calibrant discussed in Sec. A.1. The KOH-type and TlI-type phases were modeled in terms of the crystallographic parameters for each of these phases and are discussed in the next two subsections.

Table A.4: Change of parameters for mixture of phases for RbCl. The pressure determines the amount of compression, σ_i^2 and C_3. The energy shift for each path is related to an overall shift plus a constant$_i$ which was determined from the average value results of the previous model.

original parameter and shells		expression	final parameter
ΔR_i :	$i = 1, 2, 3$	ΔR_i = alpha· reff	p for each data
		alpha = A + B·p + C·p^2	
σ_i^2 :	$i = 1, 2, 3$	σ_i^2 = Debye(Temp,θ_{Debye})	
		θ_{Debye} = sig_int$_i$ + sig_slope·p	
C_3^i :	$i = 3$	C_3^i = C3_int1 + C3_slope·p	
ΔE$_i$	$i = 1, 2, 3$	ΔE$_i$ = ΔE$_0$ + constant$_i$	ΔE$_0$

A.3.1 KOH-Type Phase

Fig. A.8 shows part of the `feffit.inp` file, including the parameters needed to specify only two of the 40 paths used in the fit, for the KOH-type phase of AgCl. This piece illustrates how the unit-cell dimensions and position of the atoms within the unit cell are parameterized in terms of the basic XAFS parameter for the path length. The guess values represent those that are varied in the fit to the data. In this example the unit cell dimensions and the four atomic positions are determined by the fit to the data. A summary of the change of parameters is shown in Table A.5.

A.3.2 TlI-Type Phase

I have broken the `feffit.inp` file for the TlI-type phase of AgCl into the following sections: I) Fig. A.9: the values determined by the fit to the data are denoted by the guess key word. The other known values for the atomic positions within the unit cell are denoted by the set key word. II) Fig. A.10: lists the expressions used to calculate the change in the atomic positions relative the a central Ag atom and the path lengths from these parameters and the unit cell dimensions. III) Fig. A.11: lists only nine of the 23 paths used in the fit. Table A.6 lists the change in parameters.

Figure A.3: Part of the `feffit.inp` file for B1-phase of RbCl specifying linear pressure dependencies of σ^2 and C_3 as well as determining the pressure from the compression alpha. The path number 0 is special and means the parameterization for the key words listed apply to all paths that follow. The subscript _4 indicates that these parameters apply specifically to the data taken at the fourth pressure.

```
%==+==+==+==+==+==+==+==+==+==+==+==+==+==+==+==+==+==+==+==+==+==+==+==+==
#constant values for each pressure
set     sig_mcm 0.0029
set     s02     0.971198
set     e2     -0.43     #relative energy shifts
set     e3     -2.82
#determine the slope and intercept for debye temp and third cumulant
guess     debye_int1_b1     230.071320
guess     debye_int3_b1     263.142273
guess     deybe_int2_b1     162.905746
guess     debye_slope_b1     10.669373
guess     c3_int1_b1         0.004806
guess     c3_slope_b1       -0.002332
#variables for each pressure this is an example for the forth data set
set     e1_4          1.123877
guess   gpa_04        0.539625
set     tdebye1_4     debye_int1_b1 + debye_slope_b1*gpa_04
set     tdebye2_4     deybe_int2_b1 + debye_slope_b1*gpa_04
set     tdebye3_4     debye_int3_b1 + debye_slope_b1*gpa_04
set     third3_4      c3_int1_b1 +c3_slope_b1*gpa_04

! Alpha1 coefficients that relate compression and GPa
# for the B1-phase
set     a1_A1     -.06946
set     a1_A2      .00865
set     alpha1_4   (a1_A1* gpa_04 + a1_A2 * gpa_04^2)/3.295
set      alpha_4   ((3.295*(1+alpha1_4))/(3.275)) - 1
%  insert sets and guesses here
%==+==+==+==+==+==+==+==+==+==+==+==+==+==+==+==+==+==+==+==+==+==+==+==+==
s02      0     s02
delr     0     alpha_4 * reff

path     1     p2/feff0001.dat
id       1     amp=100.000, deg=6.000, nleg=2, r_eff=3.2950
sigma2   1     debye(293,tdebye1_4) + sig_mcm
e0       1     e1_4

path     2     p2/feff0002.dat
id       2     amp=77.914, deg=12.000, nleg=2, r_eff=4.6598
sigma2   2     debye(293,tdebye2_4) + sig_mcm
e0       2     e2 + e1_4


path     4     p2/feff0005.dat
id       4     amp=23.510, deg=8.000, nleg=2, r_eff=5.7071
sigma2   4     debye(293,tdebye3_4) + sig_mcm
third    4     third3_4
e0       4     e3 + e1_4
```

```
#Values for the B1 phase
set     e2_b1     -0.43      #relative change for energy shifts
set     e3_b1     -2.82
set     debye_int1_b1     230.199677  #intercept values debye temp
set     debye_int3_b1     263.130249
set     debye_int2_b1     162.933090
set     debye_slope_b1     10.019114  #slope for debye temp
set     c3_int3_b1          0.004812  #intercept for third cumulant
set     c3_slope_b1        -0.002350  #slope for third cumulant

#linear expressions used to determine debye temp
set     tdebye1_b1     debye_int1_b1 + debye_slope_b1*gpa_b1
set     tdebye2_b1     debye_int2_b1 + debye_slope_b1*gpa_b1
set     tdebye3_b1     debye_int3_b1 + debye_slope_b1*gpa_b1
set     third3_b1      c3_int3_b1 + c3_slope_b1*gpa_b1

# Alpha1 coefficients that relate compression and GPa
# for the B1-phase
set     a1_b1     -.06946
set     a2_b1      .00865
set     r_b1      (a1_b1* gpa_b1 + a2_b1*gpa_b1^2)/3.295
set     alpha_b1  ((3.295*(1+r_b1))/(3.26)) - 1
%==+==+==+==+==+==+==+==+==+==+==+==+==+==+==+==+==+==+==+==+==+==+==+==+==+==
```

Figure A.4: Part of the `feffit.inp` file for mixture of phases of RbCl listing the parameters and expressions part for the B1-phase of the input file.

```
%==+==+==+==+==+==+==+==+==+==+==+==+==+==+==+==+==+==+==+==+==+==+==
set     sig_mcm   0.0029           #Set values independent of phase
set     s02       0.971843

#Values for the B2-phase
set     e2_b2      1.01            #relative change for energy shifts
set     e3_b2     -1.23
set     e4_b2     -2.92
set     debye_int1_b2     227.040344  #intercept values for debye temp
set     debye_int2_b2     156.190125
set     debye_int4_b2     168.260941
set     debye_slope_b2     27.606367     #slope for debye temp
set     c3_int1_b2          0.002127     #intercept for third cumulant
set     c3_int4_b2          0.005194
set     c3_slope_b2        -0.001609     #slope for third cumulant

#linear expressions used to determine debye temperature
set     tdebye1_b2     debye_int1_b2 + debye_slope_b2*gpa_b2
set     tdebye2_b2     debye_int2_b2 + debye_slope_b2*gpa_b2
set     tdebye3_b2     tdebye2_b2
set     tdebye4_b2     debye_int4_b2 + debye_slope_b2*gpa_b2
set     third1_b2      c3_int1_b2 + c3_slope_b2*gpa_b2
set     third4_b2      c3_int4_b2 + c3_slope_b2*gpa_b2

# Alpha1 coefficients that relate compression and GPa
# GOOD for 0>P<4.5 GPa for B2-phase
set     A0_b2     1.000535
set     A1_b2     -.02789429
set     A2_b2     0.005917881
set     A3_b2     -.0005624852
set     r_r0_b2   A0_b2 + A1_b2*gpa_b2 + A2_b2*gpa_b2^2 + A3_b2*gpa_b2^3
set     alpha_b2  (r_r0_b2*(3.409/3.36)) - 1

#parameters to be determined by the fit!
set     e1_b2    0.559404      #energy shift for b2 phase
guess   e1_b1    1.144618      #energy shift for b1 phase
guess   gpa_b1  -0.055727      #pressure
guess   x        1.033978      #amount of B1 phase
set     gpa_b2   gpa_b1
set     x_b2     1 - abs(x)    #amount of B2-phase
set     x_b1     abs(x)        #amount must be positive
%==+==+==+==+==+==+==+==+==+==+==+==+==+==+==+==+==+==+==+==+==+==+==
```

Figure A.5: Part of the `feffit.inp` file for mixture of phases of RbCl listing the parameters and expressions part for the B2-phase of the input file.

```
path     5     b1_3.26/feff0001.dat
id       5     amp=100.000, deg=6.000, nleg=2, r_eff=3.2950
s02      5     s02 *x_b1
delr     5     alpha_b1 * reff
sigma2   5     debye(293,tdebye1_b1) + sig_mcm
e0       5     e1_b1

path     6     b1_3.26/feff0002.dat
id       6     amp=77.914, deg=12.000, nleg=2, r_eff=4.6598
s02      6     s02 *x_b1
delr     6     alpha_b1 * reff
sigma2   6     debye(293,tdebye2_b1) + sig_mcm
e0       6     e2_b1 + e1_b1


path     7     b1_3.26/feff0005.dat
id       7     amp=23.510, deg=8.000, nleg=2, r_eff=5.7071
s02      7     s02 *x_b1
delr     7     alpha_b1 * reff
sigma2   7     debye(293,tdebye3_b1) + sig_mcm
third    7     third3_b1
e0       7     e3_b1 + e1_b1

path     8     b1_3.26/feff0009.dat
id       8     amp=23.510, deg=8.000, nleg=2, r_eff=5.8081
s02      8     s02 *x_b1
delr     8     alpha_b1 * reff
sigma2   8     debye(293,tdebye1_b1) + sig_mcm
e0       8     e1_b1
```

Figure A.6: Part of the `feffit.inp` file for mixture of phases of RbCl listing the paths for the B1-phase of the input file.

```
%==+==+==+
```

Table A.5: Change of parameters for the KOH-type phase of AgCl. The crystallographic parameters include the unit cell dimensions: a, b, c and β and the position of the atoms within the unit cell x_{Ag}, y_{Ag}, z_{Ag}, x_{Cl}, y_{Cl} and z_{Cl} determine the length of each path. Several paths were found to have approximately the same θ_{Debye} so that only 6 were needed to determined all σ_i^2 and only 4 energy shifts were needed.

original parameter and shells		expression	final parameter
ΔR_i :	$i = 1$ to 40	$\Delta R_i = r_i$ - reff	a, b, c, β
		$r_i = sqrt(((x_{Ag} - x_{Cl}) \cdot a)^2$	x_{Ag}, x_{Cl}
		$+((y_{Ag} - y_{Cl}) \cdot b)^2$	y_{Ag}, y_{Cl}
		$+((z_{Ag} - z_{Cl}) \cdot c)^2)$	z_{Ag}, z_{Cl}
σ_i^2 :	$i = 1$ to 40	$\sigma_i^2 = \text{Debye}(\text{Temp},\theta_{Debye})$	θ_{Debye_i}
			total of 6
ΔE_i	$i = 1$ to 3	same energy shift	ΔE_1
		for first 4 Cl shells	
ΔE_i	$i = 4$ to 40	another energy shift	ΔE_2
		for all other Cl shells	
ΔE_i	$i = 4$ to 6	same energy shift	ΔE_3
		for first 2 Ag shells	
ΔE_i	$i = 7$ to 40	another energy shift	ΔE_4
		for all other Ag shells	

Table A.6: Change of parameters for the TlI-type phase of AgCl. The crystallographic parameters include the unit cell dimensions: a, b, c and the unknown position of the atoms within the unit cell y_{Ag} and y_{Cl} determine the length of each path. Several paths were found to have approximately the same θ_{Debye} so that only 4 were needed to determined all σ_i^2 and only 4 energy shifts were needed.

original parameter and shells		expression	final parameter
ΔR_i :	$i = 1$ to 40	$\Delta R_i = r_i$ - reff	a, b, c
		$r_i = sqrt(((x_{Ag} - x_{Cl}) \cdot a)^2$	
		$+((y_{Ag} - y_{Cl}) \cdot b)^2$	y_{Ag}, y_{Cl}
		$+((z_{Ag} - z_{Cl}) \cdot c)^2)$	
σ_i^2 :	$i = 1$ to 23	$\sigma_i^2 = \text{Debye}(\text{Temp},\theta_{Debye})$	θ_{Debye_i}
			total of 4
ΔE_i	$i = 1$ to 3	same energy shift	ΔE_1
		for first 4 Cl shells	
ΔE_i	$i = 4$ to 23	another energy shift	ΔE_2
		for all other Cl shells	
ΔE_i	$i = 4$ to 8	same energy shift	ΔE_3
		for first 2 Ag shells	
ΔE_i	$i = 8$ to 23	another energy shift	ΔE_4
		for all other Ag shells	

```
%==+==+==+==+==+==+==+==+==+==+==+==+==+==+==+==+==+==+==+==+==+==+==+==+==+==
#unit cell dimensions
guess   a    =  3.444568
guess   b    =  3.988621
guess   c    =  5.412174
guess   beta =  0.164238
set     asb  =  a*sin(beta)
set     acb  =  a*cos(beta)
#atomic positions for two Ag and two Cl atoms within unit cell
guess   Agx1 =  0.155904
set     Agy1 =  0.2500
guess   Agz1 =  0.199932
set     Agx2 =  abs(1-Agx1)
set     Agy2 =  Agy1 + .5
set     Agz2 =  abs(1-Agz1)
guess   Clx3 =  0.686180
set     Cly3 =  0.7500
guess   Clz3 =  0.278414
set     Clx4 =  abs(1-Clx3)
set     Cly4 =  Cly3 - .5
set     Clz4 =  abs(1-Clz3)
#deterime distance between central Ag atom and all other atoms
set     dx3  =  abs(Agx1-Clx3)
set     dy3  =  abs(Agy1-Cly3)
set     dz3  =  abs(Agz1-Clz3)
#determine distances for paths
set r1 =  sqrt((1 -1*dx3)*acb)^2 + (dy3*b)^2
                                 + (dz3*c+((1 -1*dx3)*asb))^2)
set r2 = sqrt((dx3*acb)^2+(dy3*b)^2+(dz3*c-dx3*asb)^2)
%==+==+==+==+==+==+==+==+==+==+==+==+==+==+==+==+==+==+==+==+==+==+==+==+==+==
path    1       feff_22a/feff0001.dat
id      1       amp=100.000, deg=2.000, nleg=2, r_eff=2.6505, Ag-Cl-Ag
sigma2  1       debye(temp,tCl1_debye)
delr    1       r1 - reff
e0      1       eCl1

path    2       feff_22a/feff0002.dat
id      2       amp=95.553, deg=2.000, nleg=2, r_eff=2.6891, Ag-Cl-Ag
sigma2  2       debye(temp,tCl1_debye)
delr    2       r2 - reff
e0      2       eCl1
```

Figure A.8: Part of the `feffit.inp` file for KOH-type phase of AgCl.

```
%==+==+==+==+==+==+==+==+==+==+==+==+==+==+==+==+==+==+==+==+==+==+==
set     S02      0.91
set     temp     150
guess   tag1_debye     183.193771       #debye temperatures
guess   tag2_debye     122.069031
guess   tcl1_debye     522.914673
guess   tcl_debye     239.382584
guess   a        3.3811     #unit cell dimensions
guess   b        9.8448
guess   c        4.0976
set     beta     0
set     asb      a*sin(beta)
set     acb      a*cos(beta)
guess   eAg1     1.563378       #energy shifts
guess   eAg     -3.584770
guess   eCl1     5.178380
guess   eCl      0.999558
set     Agx1     0.0000
set     Agy1     min(1,abs(Agy1a))
guess   Agy1a    0.3990     #undetermined value y for Ag.
set     Agz1     0.2500
set     Agx2     0.0000
set     Agy2     abs(Agy1 -.5) + .5
set     Agz2     0.7500
set     Agx3     0.5000
set     Agy3     Agy1 + .5
set     Agz3     0.2500
set     Agx4     0.5000
set     Agy4     abs(Agy1 - .5)
set     Agz4     0.7500
set     Clx5     0.0000
set     Cly5     min(1,abs(Cly5a))
guess   Cly5a    0.1320          #undetermined value y for Cl.
set     Clz5     0.2500
set     Clx6     0.0000
set     Cly6     abs(Cly5 -.5) + .5
set     Clz6     0.7500
set     Clx7     0.5000
set     Cly7     Cly5 + .5
set     Clz7     0.2500
set     Clx8     0.5000
set     Cly8     abs(Cly5 - .5)
set     Clz8     0.7500
%==+==+==+==+==+==+==+==+==+==+==+==+==+==+==+==+==+==+==+==+==+==+==
```

Figure A.9: Part of the `feffit.inp` file for HPPII of AgCl listing the parameters and expressions part of the input file.

```
#determine the difference in the atomic positions
set     dx1     abs(Agx1-Agx1)
set     dy1     abs(Agy1-Agy1)
set     dz1     abs(Agz1-Agz1)
set     dx2     abs(Agx1-Agx2)
set     dy2     abs(Agy1-Agy2)
set     dz2     abs(Agz1-Agz2)
set     dx3     abs(Agx1-Agx3)
set     dy3     abs(Agy1-Agy3)
set     dz3     abs(Agz1-Agz3)
set     dx4     abs(Agx1-Agx4)
set     dy4     abs(Agy1-Agy4)
set     dz4     abs(Agz1-Agz4)
set     dx5     abs(Agx1-Clx5)
set     dy5     abs(Agy1-Cly5)
set     dz5     abs(Agz1-Clz5)
set     dx6     abs(Agx1-Clx6)
set     dy6     abs(Agy1-Cly6)
set     dz6     abs(Agz1-Clz6)
set     dx7     abs(Agx1-Clx7)
set     dy7     abs(Agy1-Cly7)
set     dz7     abs(Agz1-Clz7)
set     dx8     abs(Agx1-Clx8)
set     dy8     abs(Agy1-Cly8)
set     dz8     abs(Agz1-Clz8)
#determine the path lengths from the atomic positions
set r1 = sqrt((dx5*acb)^2+(dy5*b)^2+(dz5*c+dx5*asb)^2)
set r2 = sqrt((dx8*acb)^2+(dy8*b)^2+(dz8*c+dx8*asb)^2)
set r3 = sqrt((dx7*acb)^2+(dy7*b)^2+(dz7*c+dx7*asb)^2)
set r4 = sqrt((dx2*acb)^2+(dy2*b)^2+(dz2*c+dx2*asb)^2)
set r5 = sqrt(((1+dx1)*acb)^2+(dy1*b)^2+(dz1*c+((1+dx1)*asb))^2)
set r6 = sqrt((dx4*acb)^2+(dy4*b)^2+(dz4*c+dx4*asb)^2)
set r7 = sqrt((dx1*acb)^2+(dy1*b)^2+((1+dz1)*c+dx1*asb)^2)
set r10 = sqrt(((1+dx5)*acb)^2+(dy5*b)^2+(dz5*c+((1+dx5)*asb))^2)
set r12 = sqrt(((1+dx2)*acb)^2+(dy2*b)^2+(dz2*c+((1+dx2)*asb))^2)
set r13 = sqrt((dx5*acb)^2+(dy5*b)^2+((1+dz5)*c+dx5*asb)^2)
set r14 = sqrt((dx7*acb)^2+(dy7*b)^2+((1+dz7)*c+dx7*asb)^2)
set r15 = sqrt((dx6*acb)^2+(dy6*b)^2+(dz6*c+dx6*asb)^2)
set r17 = sqrt((dx3*acb)^2+(dy3*b)^2+(dz3*c+dx3*asb)^2)
set r21 = sqrt(((1+dx1)*acb)^2+(dy1*b)^2+((1+dz1)*c+((1+dx1)*asb))^2)
set r23a = sqrt(((1+dx1)*acb)^2+(dy1*b)^2+((1+dz1)*c+((1+dx1)*asb))^2)
set r23b = sqrt((dx8*acb)^2+(dy8*b)^2+(dz8*c+dx8*asb)^2)
set r23c = sqrt((dx8*acb)^2+(dy8*b)^2+(dz8*c+dx8*asb)^2)
set r23 = .5 * (r23a + r23b + r23c)
set r25a = sqrt((dx3*acb)^2+(dy3*b)^2+(dz3*c+dx3*asb)^2)
set r25b = sqrt((dx7*acb)^2+(dy7*b)^2+(dz7*c+dx7*asb)^2)
set r25c = sqrt((dx5*acb)^2+(dy5*b)^2+(dz5*c+dx5*asb)^2)
set r25 = .5 * (r25a + r25b + r25c)
%==+==+==+==+==+==+==+==+==+==+==+==+==+==+==+==+==+==+==+==+==+==+==+==+==+==
```

Figure A.10: Part of the `feffit.inp` file for HPPII of AgCl listing the parameters and expressions for determining the path lengths in terms of the unit cell dimensions.

```
%==+==+==+
```

VITA

Shelly Diane Kelly was born at noon in Twin Falls, Idaho on May 1, 1970 to Vicki Jones and Stephen Jones. In 1988, she graduated from Boise High School, Idaho. She graduated *cum laude* with a B.A. in physics from the University of Idaho in 1992. The following fall she came to Seattle, Washington to begin graduate studies in physics at the University of Washington. It was then that she met her husband to be Michael Kelly while taking photographs for the department picture gallery. Some of Shelly's favorite things are: playing the clarinet, skiing on a sunny day, lifting weights with her husband, betting her dad in a foot race, and figuring out a good puzzle.